# DIELECTRIC BEHAVIOR CHARACTERIZATION OF FUNCTIONAL FIBROUS - CERAMIC / POLYMER NANOCOMPOSITES

by

CANAN DAĞDEVİREN

Submitted to the Graduate School of Engineering and Natural Sciences
in partial fulfillment of
the requirements for the degree of
Master of Science

Sabancı University
Spring 2009

# DIELECTRIC BEHAVIOR CHARACTERIZATION OF FUNCTIONAL FIBROUS - CERAMIC / POLYMER NANOCOMPOSITES

APPROVED BY:

Assist. Prof. Dr. Melih Papila…………….......................................................
(Dissertation Supervisor)

Assist. Prof. Dr. Cleva Ow Yang……………………………........................

Assoc. Prof. Dr. Mehmet Ali Gülgün …………………......................................

Prof. Dr. Yusuf Ziya Menceloğlu………………….......................................

Prof. Dr. Hüseyin Zafer Durusoy………………………….........................

DATE OF APPROVAL: June 05, 2009

# DIELECTRIC BEHAVIOR CHARACTERIZATION OF FUNCTIONAL FIBROUS - CERAMIC / POLYMER NANOCOMPOSITES

**Canan Dağdeviren**

**Materials Science and Engineering, M. Sc. Thesis, 2009**

**Thesis Advisor: Assist. Prof. Melih Papila**

**Key words:** PVDF, ZnO, PZT, electrospinning, nanofiber, nanocomposite, dielectric characterization.

## ABSTRACT

This study is mainly focused on forming fibrous-ceramic/polymer nanocomposites and characterizing their dielectric behavior.

The fibrous-ZnO/PVDF nanocomposite is prepared in two steps. First, a network of nano-scale zinc oxide (ZnO) fibers is produced by sintering electrospun PVA/Zinc Acetate fibers. Second, the ZnO fibrous non-woven mat is sandwiched between two polyvinylidine fluoride (PVDF) thermoplastic polymer films by hot-press casting. Referring to the extensive literature search within the thesis, this work is the first demonstration of the use of electrospinning to secure the dispersion and distribution of a network of inorganic fillers. Moreover, processing a fibrous-ZnO/PVDF flexible composite facilitate material handling and enable dielectric property measurement, in contrast to that on a fibrous mat of pure ZnO. Due to the high surface area of the short ZnO fibers and their polycrystalline structure, interfacial polarization is pronounced in the nanocomposite film. The dielectric constant is enhanced significantly—up to a factor of ten at low frequencies compared to the dielectric constant of constituent materials (both bulk ZnO and PVDF), and up to a factor of two compared to a bulk-ZnO/PVDF composite.

Similar effort is also presented for the fibrous-PZT/polyvinylester nanocomposite. Nanofibers are obtained by electrospinning a sol-gel based solution and polyvinyl pyrrolidone (PVP) polymer, and subsequent sintering of the electrospun precursor fibers. The average diameter of the precursor PZT/PVP green fibers is increased with the aging of the precursor solution along with an increase in the viscosity. Preparation of 3-3 nanocomposites by infusion of polyvinylester into the nanofiber mat facilitates successful handling of the mats and enables measurements of dielectric properties.

# FİBER YAPILI SERAMİK/POLİMER FONKSİYONEL NANOKOMPOZİTLERİN DİELEKTRİK DAVRANIŞ KARAKTERİZASYONU

**Canan Dağdeviren**

**Malzeme Bilimi ve Mühendisliği, Yüksek Lisans Tezi, 2009**

**Tez Danışmanı: Yar. Doç. Dr. Melih Papila**

## ÖZET

Bu çalışma temel olarak, fiber yapılı seramik/polimer nanokompozitlerin üretilmesi ve bunların dielektrik davranışının karakterize edilmesi üzerinde yoğunlaştırılmıştır.

Fiber yapılı ZnO/PVDF nano kompozit iki aşamada hazırlamıştır. İlk olarak, PVA/Zinc Acetate electro dokuması sinterlenerek, nano ölçekli ZnO fiberler elde edilmiştir. İkinci basamaktada, PVDF termoplastik filmlerin arasına yerleştirilmiş, örgü düzeni bulunmayan nano ölçekli fiber yapılı ZnO tabakası bu filmlerin arasına sıcak presleme ile sandöviç edilmiştir. Bu çalışma, kapsamlı kaynakça taraması sonucu erişilebilen bilgi dahilinde, elektrodokumanın organik olmayan katkı malzemeleri için dağılımlarını ve yayılmalarını sağladığını gösteren bir ilktir. Bununda ötesinde, fiber yapılı ZnO/PVDF esnek kompozitlerin yapımı ile saf fiberli ZnO tabakalarının aksine, malzemenin elle tutulması sağlanmış ve dielektrik özelliği için ölçüm alabilme yeteneği kazandırılmıştır. Kısa ZnO fiberlerin büyük yüzey alanları ve polikristalin yapılarına bağlı olarak, nano kompozit film içinde, ara yüzey kutuplaşması artmıştır. Dielektrik sabiti dikkat çekici biçimde artmıştır; kütlesel/yığın ZnO ve PVDF'e karşı, kompozitin dielektrik sabiti düşük frekanslarda 10 mertebe; yığın ZnO/PVDF kompozite karşı ise 2 mertebe artmıştır.

Benzer çalışma planı, fiber yapılı PZT/polyvinylester nanokompozit için de uygulanmıştır. Nano fiberler, sol-jel temelli PZT çözeltisi ve PVP'nin karışımının elektro dokuma yapılması ve sonrasında öncü fiberlerin sinterlenmesiyle elde edilmiştir. PZT/PVP yaş fiberlerin ortalama çapı, öncü karışımın zamanla yaşlanması ve artan akışkanlığı ile artmıştır. Polyvinylester içine emdirilen nano fiber tabakalar sonucu oluşan, 3-3 nano kompozitler malzemenin kırılmadan işleme tabi tutulabilmesini ve dielektrik özellikleri için ölçüm alınabilmesini sağlamıştır.

**PREFACE**

Prehistoric people figured out to use tools first consisting only of stones and bones for their needs, then learned how to shape those materials to adapt them to their needs. As time passed, they discovered new materials which were then processed to always more complex shapes. Again they used those tools to manufacture other tools, parts, and structures. Obviously, the materials used by different cultures in most cases were the only records left for anthropologists to define civilization and were the sources for scientists to manufacture structures for their needs for example, mechanic and electronic devices, and biological systems.

Now, in the later decades of the 20 and 21$^{st}$ centuries material science has been more interested in so called "Functional Materials" - materials showing the intrinsic ability to change their shape and improve their physical and chemical properties in cooperation with other materials; for instance those which lay the basis for novel applications in many fields such as aerospace, the electronic world and biomedicine. Functional materials, for example, sense changes in the environment around them and respond in a predictable manner. Increased demands for high performance control design in combination with recent advances in material science have produced a class of systems termed smart, intelligent, functional or adaptive systems. The research and development of these functional materials and smart structural systems has been actively pursued during the last decade, and the technological applications of this group of materials span a wide range from the complex structures such as aerospace systems to the daily used structures such as electronic circuits.

One such nanotechnology is nowadays a popular interdisciplinary field including many areas such as mechanics, electronics, optics, biology, medicine, and material science for obtaining functional systems and materials. Ceramic, polymer, and composites; especially fibrous- ceramic/polymer composites, are fascinating materials for nanotechnology. Because of their small characteristic dimension, high surface area, micro structural features; they provide unique mechanical, optical, electronic, magnetic, and chemical properties for a wide variety of materials and applications. They are mostly produced by the novel methods resulting in discontinuous fibers. The literature has noted that fibrous ceramic fibers improve electronic properties due to high surface area and polycrystalline morphology resulting in interfacial polarization. That is why there is a considerable interest in producing fibers at nano-scale thanks, in particular, to the electrospinning technique. This novel method makes possible the efficient production of elongated and very narrow diameter range (10-1000 nm) fibers. A number of polymer and ceramic nanofibers have been electrospun directly from polymer & ceramic precursor solutions as in our experiments within the thesis. It can be also easily seen in recent studies that ceramic fibers are also prepared with electrospinning using conventional sol-gel method, followed by a high-temperature pyrolysis. Additionally, the novelty of fibrous-ceramic/polymer nanocomposites that facilitate material handling and enable dielectric property measurement, in contrast to that on a fibrous mat of pure ceramic is described within this thesis.

*...and the God sent apple to Newton!*
(the importance of luck and true material )

*C. D.*

*to the stars in the sky. . . .*

## ACKNOWLEDGEMENT

I am indebted to Dr. Sait Eren San, Dr. Mustafa Okutan and Ahmet Demir from Gebze Institute of Technology for allowing the use of scientific equipments at Department of Physics; and also thankful to Prof. Kerim Allahverdi from TÜBİTAK Marmara Research Center, Materials Institute.

I would also like to thank Nancy Karabeyoğlu for her critical review and editing of my writing, which significantly improved the quality of my manuscripts. With her words: Thanks dear!

I would like to thank my close friends who are always willing to help me: Assist. Prof. Arun Anand Prabu from Vellore Institute of Technology (VIT) University, and Dr. Patrick Lake from Applied Science, Inc, and my room mate; Ayşe Ezgi Gürcan.

I am grateful for the friendship of Didem Ekinci, Orkun Karabaşoğlu, Emre Fırlar, Işıl Berkün, Mustafa Koz, Özge Malay, Anna Vanya Uluç, Zuhal Taşdemir, Gökhan Kaçar, Koray Aras, Can Kartoğlu, Murat Karalar, Murat Mülayim, Firuze Okyay, Ahmet Fatih Tabak, Eren Şimşek, İlhan Özen, Çınar Öncel, Sinem Taş, Yeliz Ekinci, Elif Özden, Burcu Genç, Shalima Sawuti, Gönül Kuloğlu, Filiz Dolapçı, Burak Abi--- who always inspired me with their positive attitudes. I wish to extend my thanks to all the former and present friends and colleagues for all the fun.

I am also grateful to the faculty staffs, Işıl Önal Karabudak, and Adnan İnce.

I thank my parents, Mine and Cavit; my sweet brothers Servet Caner and Hüseyin Emre; my grandparents, Melek-Ali Calışkanoğlu and İpek-Niyazi Boztepe; without the love and support of my family I could not have finished this thesis. Without them, I would not be where I am today; I mean I could not be Canan ☺ Thanks to my lovely family, I love you!

To whom it may concern: Thank the stars!

**TABLE OF CONTENTS**

# LIST OF FIGURES

# LIST OF TABLES

# LIST OF SYMBOLS

| | |
|---|---|
| $T_c$ | Curie Temperature |
| $\varepsilon$ | Dielectric response |
| $\varepsilon'$ | Real dielectric response |
| $\varepsilon''$ | Complex dielectric response |
| $C_p$ | The parallel capacitance |
| $d$ | The inter electrodes distance |
| $\varepsilon_0$ | The permittivity of free space |
| A | The space area |
| $\varphi$ | The phase angle |
| $\varepsilon^*(\omega)$ | The complex dielectric response |
| $\varepsilon_\infty$ | The limiting high-frequency dielectric response |
| $\tau$ | The average relaxation time |
| $\omega$ | The average angular frequency |
| $\alpha$ | The distribution parameter |
| $E_{bd}$ | dc dielectric strength |
| $\Delta H_{theo}$ | Theoretical heat of fusion value |
| $\tan \delta$ | Tangent loss |
| $R_a^2$ | Adjusted coefficient of determination |
| $f_c$ | Dielectric relaxation frequency |
| $\varepsilon_0'$ | Low frequency dielectric response |
| $\varepsilon_\infty'$ | High frequency dielectric response |
| $\varepsilon_{max}''$ | Max. dielectric response |
| T | Temperature |

# LIST OF ABBREVIATIONS

| | |
|---|---|
| ZnO | Zinc oxide |
| PVDF | Poly(vinyldene fluoride) |
| PZT | Lead zirconium titanate |
| PVP | Polyvinyl pyrrolidone |
| PAN | Polyacronitrile |
| DMF | N,Ndimethylformamide |
| PHB | Poly(3- hydroxybutyrate) |
| ZnAc | Zinc acetate |
| PVA | Polyvinyl alcohol |
| ZnOH | Zinc hydroxide |
| PVP | Polyvinyl pyrrolidone |
| PbO | Lead oxide |
| XRD | X-ray diffractometry |
| DSC | Differential scanning calorimetry |
| SEM | Scanning electron microscopy |
| MOCVD | Metal organic chemical vapor deposition |
| TGA | Thermo Gravimetric Analysis |
| VSSP | Viscous suspension spinning process |
| PNCs | Polymer nanocomposites |
| TGTG | trans-gauche–trans-gauche |
| TTTT | all-trans |
| AC | Alternating current |

**CHAPTER 1**


**1. INTRODUCTION**


The development of functional composites consisting of the electro-active particles embedded in a polymeric matrix is essential, because of the need to combine the inherent processability and flexibility of polymers with the electro-active response of the ceramics. This has also been the driving force in the course of this thesis. The functional fibrous-ceramic/polymer nanocomposites were investigated for their dielectric behavior essential for the electroactivity, when subjected to an applied electrical bias. The composites presented here are considered functional due to their electro-active properties along with their dielectric properties, low-cost, high surface area, low density and flexibility in contrast to the bulk form of electro-active ceramics.


## 1.1 Motivation


Among the several reasons for producing electro-active polymer composites that can be listed in favor of nanocomposites, the following three are particularly addressed within this thesis:


1) There is great potential to develop a stable structure (i.e. mechanically, chemically) by choosing the constituents, which have complementary properties. For instance, the composite is desired to improve on the mechanical properties of a functional brittle electro-active ceramic material by embedding its filler form within a polymer matrix that has mechanically favorable properties.

2) There is need to facilitate nano-scale material handling and enable electrical measurements on macro scale specimens representing a proptotype for an application. For instance, the specimens introduced herein may be considered as sensors or actuators due to their potential electroactivity.

3) It is known that there is great potential to benefit from high surface area of well dispersed nano-scale filler materials compared to bulk filler composites on the material response such as polar orientation and associated dielectric capability.

## 1.2 Focus

In multidisciplinary research involving the materials science and engineering, one of the intriguing paths is on functional smart materials for applications, such as dielectric storage, sensors and actuators.

Organic, inorganic and their composites, there are variety of choices for functional smart material applications. A polymeric material poly(vinylidene fluoride) -PVDF-, for instance, is known to have polar characteristics, piezoelectric, and pyroelectric properties. Correspondingly, PVDF films have been widely considered in sensor and actuator applications due to its electronic characteristic. On the other hand, ceramic materials such as lead zirconium titanate -PZT- are most frequently used in piezoelectric and ferroelectric devices due to their remarkable electro-active behavior. Another example for inorganic materials is zinc oxide -ZnO- which has been attracting attention in the last decade due not only to its being an optical material, but also to its showing useful electronic properties.

In the open literature, there has been substantial efforts reported on the production or the processing these materials. An intriguing technique for processing both polymeric and inorganic materials is electrospinning as it enables production of nano-scale or micro-scale ceramic or polymer fibers. The fiber mats can also be used for functional electro-active systems.

The ultimate outcome of this thesis is establishing the process flow to produce functional electrospun fibrous-ceramic/polymer nanocomposites, and their dielectric characteristics. With these in mind, the focus of this thesis is directed towards the dielectric enhancement over the sole matrix polymer by making the nanocomposites with the electro-active ceramic fillers. Characterization of the key constituent materials is also presented. Specifically, crystal structure of the PVDF samples by different processes, and the crystal structure of the fibrous-ZnO and PZT samples are studied.

The novelty in this thesis is the first demonstration of the use of electrospinning method to secure the dispersion and distribution of a network of inorganic fillers. The other contribution to the literature is that the processing and characterization of electrospun PZT fibers, and its precursor polymer solution aging factor is reported. By taking into the account aging factor, the optimum PZT fibers can be enhanced with a low amount of PVP concentration. In the end, the electronic measurements on the resultant composite are expected to carry on very effectively in contrast to that on a fibrous mat of pure PZT.

## 1.3 Objectives and Scope of the Thesis

The two primary objectives in this thesis within the course of functional nanocomposite research are :

- to establish process flow for making polymer matrix nanocomposites with well dispersed inorganic fibrous fillers by electrospinning
- to demonstrate and report the dielectric characterization of the electrospun inorganic fibers by embedding them into a polymer matrix, while otherwise is not practical due to handling difficulties.

The experiment-based work was mainly focused on the use of electrospinning technique in the process flow, and PVDF, ZnO and PZT were the three key constituents for the composite making. The work breakdown was in three parts, each reported as

separate chapters (Chapters 3-5) presenting the associated journal articles that are submitted for publication.

The work presented as paper 1 (Chapter 3), is "The Effect of Processing and Crystallinity upon Dielectric Behavior of PVDF". This paper, although not covering a nanocomposite effort, is considered as complementary since the thermoplastic polymer PVDF is one of the key constituents in this work. The paper is mainly focused on the dielectric behavior of PVDF and its dependence on the crystalline structure that may vary upon the processing of the polymer. Three different processes were employed to prepare the PVDF samples: electrospinning, melt casting, and cold-press casting. These processes are described, followed by the dielectric characterization of the PVDF samples under various frequencies and temperature along with the crystalline structure. Supporting evidence for the results and associated discussions regarding the correlation of the dielectric properties and the crystallinity of PVDF are provided by the x-ray diffractometry (XRD), differential scanning calorimetry (DSC) and scanning electron microscopy (SEM). The Cole-Cole plots are also presented for dielectric mechanism interpretation. The paper is completed in collaboration with Dr. Mustafa Okutan and Dr. Sait Eren San from Physics Department at Gebze Institute of Technology (GYTE).

The work titled "Dielectric Behavior Characterization of a Fibrous-ZnO/PVDF Nanocomposite" is presented as paper 2 (Chapter 4), and the first of the two functional nanocomposite demonstration in the thesis work. It introduces the concept of using electrospinning to form an inorganic filler network to secure the dispersion and distribution of the fillers in the polymer matrix. Specifically, the feasibility is reported for the use of fibrous ZnO fillers by electrospinning and their insertion into a PVDF polymer matrix to form the nanocomposite. The process for producing the fibrous-ZnO/PVDF nanocomposite is also described, followed by the dielectric characterization of the nanocomposite under various frequencies and temperatures along with the crystalline structure. Supporting evidence for the results and associated discussions are provided by the x-ray diffractometry (XRD), SEM, and Raman spectroscopy.

Finally, the paper 3 (Chapter 5) reported as "Processing Conditions and Aging Effect on the Morphology of PZT Electrospun Nanofibers and on Dielectric Properties of the Resulting 3-3 PZT/Polymer Composite" arose from a collaboration with Dr. Ebru Mensur Alkoy. The content of the paper covers the investigation of the processing conditions in electrospinning of polymeric precursor fiber mats followed by annealing for PZT nanofibers, and the examination of the phase and morphology of these nanofibers prior and posterior to the annealing process, along with the characterization of the dielectric properties of the resultant PZT/poly(vinylester) nanocomposite.

Following this introductory chapter, Chapter 2 presents a literature survey that is somewhat concentrated on the electrospinning and the key constituents of the nanocomposites presented herein. More literature discussions specific to the papers are also presented in the associated Chapters 3-5. Chapter 6 summarizes the conclusions from the three papers and followed by the description of the ongoing extension of the nanocomposite process and their electro-active characterization.

# CHAPTER 2

## 2. LITERATURE REVIEW

### 2.1 Materials

#### 2.1.1 Poly(vinylidene fluoride): PVDF

Poly(vinylidene fluoride) -PVDF- has been synthesized since the 1940s; however its ferroelectric property was not discovered until the late 1960s. Apart from PVDF's ferroelectric property [1-2], this pure thermoplastic fluoro polymer possesses other intriguing properties such as being pyroelectric [3], bio-compatible [4] and chemically resistive [5]. Additionally, the glass transition temperature of PVDF is typically around -40 °C so that at room temperature the polymer is flexible with good mechanical properties [6]. Due to these properties, PVDF and its copolymers have been widely studied [7-11]. Among the class of polymer materials, PVDF has a high dielectric constant ($\varepsilon_r$ = 11-14) and high dc dielectric strength ($E_{bd}$ = 770 MV/m) [11, 12], which make it also a promising polymeric dielectric material for use in electronic areas such as energy storage capacitors.
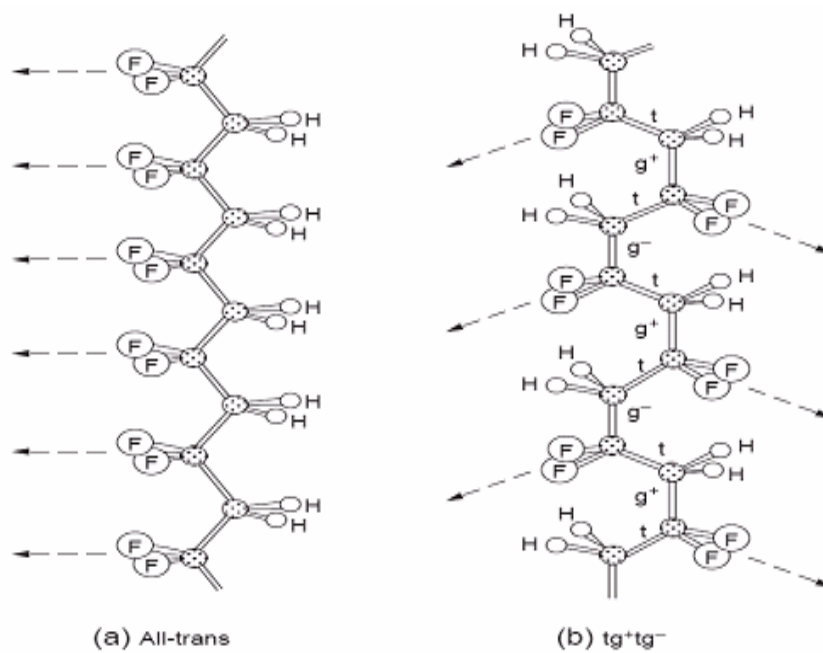
Figure 2.1: Schematic illustration of the two common crystalline chain conformations in PVDF (a) all-trans (TTTT) conformation and (b) tg+ tg- (TGTG-) conformation. The arrows indicate the projection of the $CF_2$ dipole on planes defined bye the carbon backbone. Courtesy of Kwan Chi Kao [12].

Depending on the temperature and the conditions at which the polymer crystallizes, for the most common polymorph PVDF produced is by cooling the melt and by solution casting,-- the unit cell predominantly consists of two chains in the TGTG configuration and possesses dipole moments of the chain axis. Therefore, the dipole moments of the two chains in the unit cell are anti-parallel, and the crystal does not exhibit spontaneous polarization. In this case, the nonpolar phase of PVDF is referred to as the $\alpha$ - phase. On the other hand, if the PVDF crystallizes at a temperature below 130 °C and at a high pressure or in conjunction with a special epitaxial technique, the morphology of PVDF is changed to a structure oriented to the *c - axis*, and the unit cell also consists of two all - trans chains packed with their dipoles pointing in the same direction. By mechanical stretching or electrical poling, this crystal structure renders PVDF in the most highly polar phase, which is generally referred to as the $\beta$ - phase [13, 14]. The chains take on a planar zigzag (TTTT) as shown in Figure 2.1.
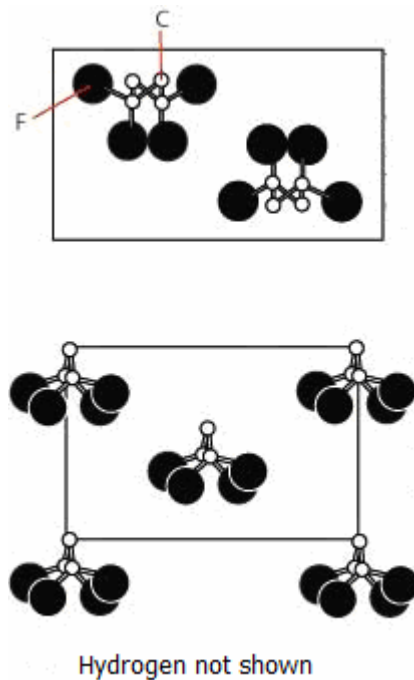
Figure 2.2: Unit cells of PVDF. Courtesy of [15].

TG molecules stack with a center of symmetry, thus form a nonpolar unit cell. Contrary to this; all trans molecules stack without giving rise to a center symmetry, forming a polar unit cell that is depicted in Figure 2.2.

In its solid state, PVDF is a semi-crystalline polymer with approximately 50% crystallinity that is known to change as a function of the processing [16]. The physical properties of the semi-crystalline polymers depend upon the processing conditions and the resulting crystal morphology developed within the processed sample [6, 17]. There are several polymorphs of this polymer, yet only four of them are well understood and described in the literature: $\alpha$, $\beta$, $\gamma$, and $\delta$ or phases II, I, III, IV respectively [3, 17-23]. The proportions of PVDF crystalline phases also depend on the method of preparation. The signature of total crystallinity, the phases and the polymorphs of PVDF, can be observed on several measurable properties of PVDF. The polymer chains with trans - gauche (TG) conformation in the $\alpha$ - phase are stacked with their respective polarization in alternating directions, resulting in a nonpolar phase and paraelectric behavior [22]. The $\beta$ - phase, on the other hand, has all-trans zigzag chain conformation and parallel dipole moments, and thus is the polar phase with large spontaneous

polarization resulting in ferroelectricity and piezoelectricity [22]. The $\beta$ type PVDF for instance, is applicable for a sensor material [24]. The typical dominant phase is $\alpha$-phase, as it is the most stable phase at room temperature [23].

The degree of the crystallinity as well as the size of the crystallites and the lamella thickness of PVDF samples may be influenced either by an externally applied electric field and mechanical stress or by thermal treatment. It should be noted also that space charge built up near the interface of the crystallites and amorphous matrix results in a change of dielectric relaxation hindering molecular motions [25].

Solution casting, melt casting, and spin coating are some of the techniques for processing polymer films or mats. Many of the researchers focuses on solution casting type to understand PVDF film properties due to the simplicity of solution casting in production. Nevertheless, by using the electrospinning process, which is a novel method to obtain distinct size of fiber diameters, micron-sized or nano-sized fibers of PVDF can easily be formed of a natural polymer solution. These fibrous forms have strong potential to be utilized in a wide range of applications from lithium battery electrolytes to flexible actuators. In addition, the most distinctive properties, such as porosity and higher surface area, are really important parameters in many applications, for instance, gas sensors, electronic coatings, and battery electrolytes [26, 27].

**2.1.2 Zinc oxide: ZnO**

In materials science, Zinc oxide -ZnO- is often called a II-VI semiconductor because zinc and oxygen belong to the 2nd B and 6th A group of the periodic table, respectively. This semiconductor has several favorable properties: good transparency, high electron mobility, wide band gap, strong room-temperature luminescence, etc. Therefore, ZnO has been focus of numerous studies due to its possible applications in sensing [28, 29], catalysis [30], optical emission [31, 32], piezoelectric transduction, and actuation [33-35]. The ability to obtain various forms of ZnO makes it even more appealing in using for different applications. Individual ZnO nanobelts, for instance,

were obtained, and their characterization via piezoresponse force microscope imparts promising results for the future of ZnO in nano-sensors and nano-actuators industry [36]. Zinc oxide is also of great interest as a suitable material for high temperature, high power electronic devices. It can be utilized either as the active material or as the substrate for the epitaxial growth of group III-nitride compounds due to its large, direct band gap (3.4 eV at 300 K) and high excitonic binding energy (60 meV) [37, 38]. Therefore, pure ZnO is colorless and transparent. The advantages connected with a large band gap include higher breakdown voltages, ability to sustain large electric fields, lower electronic noise, and high-temperature and high-power operation. Additionally, the dielectric constant of bulk ZnO is between 9.9 and 11 [39]. This dielectric constant value range is available for the coatings used for most automotive / aerospace / electronics applications.

ZnO is a chemical compound that commonly exists in white hexagonal crystals in a stable wurtzite crystal with lattice constants *a = 0.325 nm* and *c = 0.521 nm*; the ratio of *c/a ~1.60* is close to the ideal value for the hexagonal cell *c/a = 1.633*. So, the crystal structure is a hexagonal close pack structure, where the atoms are stacked together in the *ABABAB...* as depicted in Figure 2.3. Yellow balls represent O atoms; brown balls, Zn atoms.
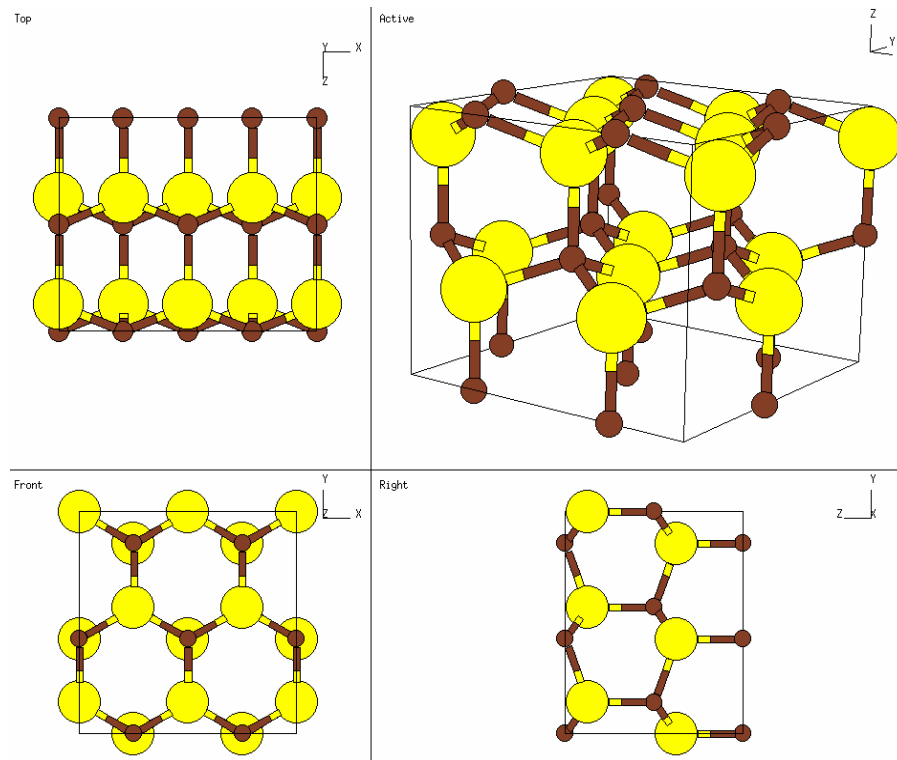
Figure 2.3: Zinc oxide crystal wurtzite structure. Courtesy of [40].

There are various fabrication methodologies to produce ZnO films and structures such as sputtering techniques, chemical vapor deposition [28], solid vapor phase process [41], thermal evaporation, and electro deposition [42, 43]. Selective growth of ZnO nanorod arrays grown on C-plane sapphire substrates are shown in Figure 2.4, can be generated by these methods at different process conditions. The control in structural formation and repeatability however are somewhat problematic for each of these fabrication methods.
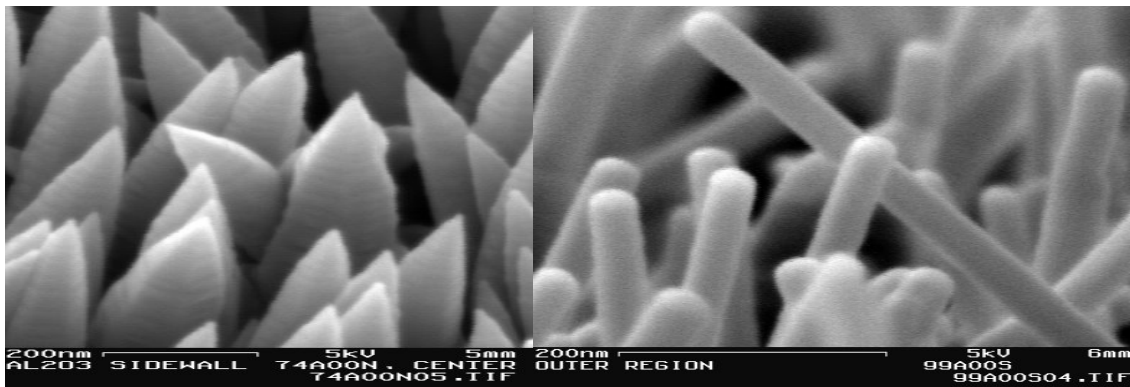


Figure 2.4: Selective growth of ZnO nanorod arrays grown on C-plane sapphire substrates. Courtesy of Muthukumar et *al.* [44].

11

It is well known that ZnO nano materials are promising candidates for nano electronic and photonics. Compared with other semiconductor materials, ZnO has higher excitonic binding energy (60 meV), more radiation hard, and is electronically functional (piezoelectric, dielectric and ferroelectric) when poled. As a good example, well-aligned ZnO nanowires can be grown on various substrates at low temperature by metal organic chemical vapor deposition (MOCVD) as seen in Figure 2.5. These nano structures have potential applications in field emission devices, near-field microscopy, and UV photonics.
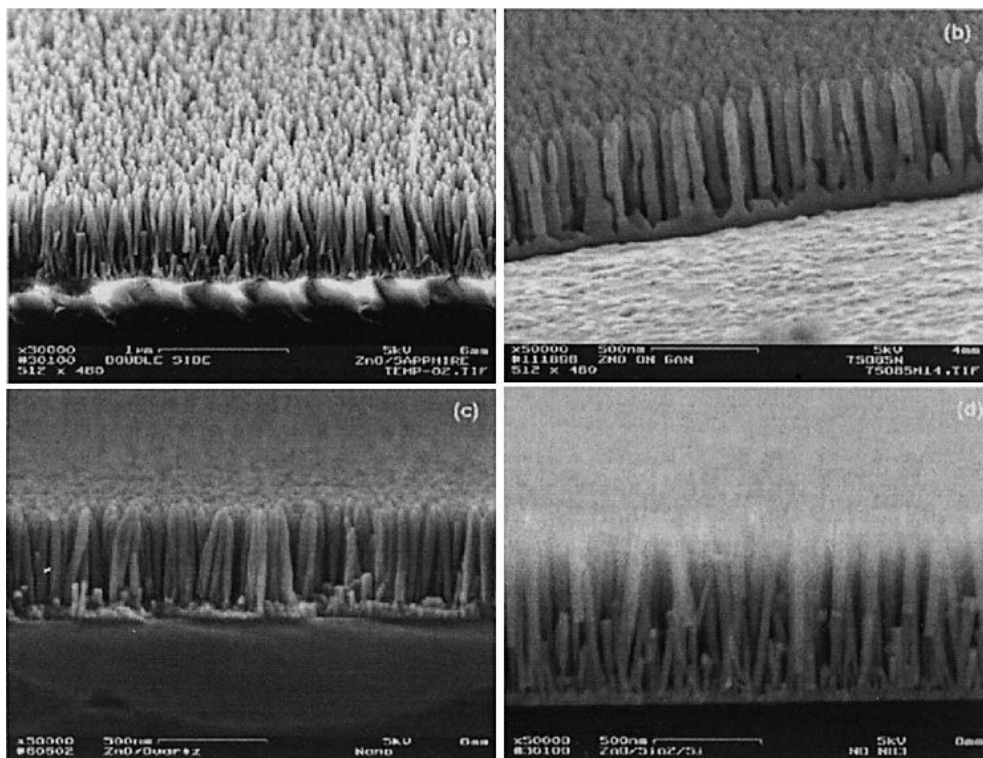


Figure 2.5: Field Emission Scanning Electron Microscope images of columnar growth of ZnO on (a) c −$Al_2O_3$, (b) epi GaN, (c) fused silica, and (d) SiO/Si substrates. Courtesy of Muthukumar et al. [44].

An alternative novel and easy to use manufacturing technique for nano-scale fibrous formations is by a sequence of electrospinning and heat treatment. Polyacronitrile (PAN) for instance, was electrospun and exposed to thermal treatment to produce a high purity carbon nanofiber web, a potential anode material for high-power lithium-ion batteries [45]. Bioactive glass nanofibers were also produced by electrospinning a sol-gel precursor solution followed by thermal treatment [46]. The

network of ZnO nano-scale fibers can also be produced by this process sequence [47-50]. The control of pattern and the problem of resultant morphology can be overcome in the electrospinning of the polymer precursor fiber; methods have been proposed and proven for controlling the fiber alignment, for instance the work by Dzenis [51]. The effect of thermal treatment of the precursor fibers on the as spun pattern and morphology, however, is still under investigation. Wu and Pan, for instance, concentrated on the change in fiber diameter due to the varying calcination time [50], and recently Kim et *al.* reported their results concerning the morphology variation due to several effects and concluded  that calcination conditions were the most significant [52].

### 2.1.3 Lead zirconate titanate: PZT

Piezoelectric $Pb(Ti,Zr)O_3$ -PZT- solid-solution ceramics are widely used in electronic devices because of their superior piezoelectric properties. The phase diagram of the PZT system $(Pb(Zr_xTi_{1-x})O_3)$ is shown in Figure 2.6.
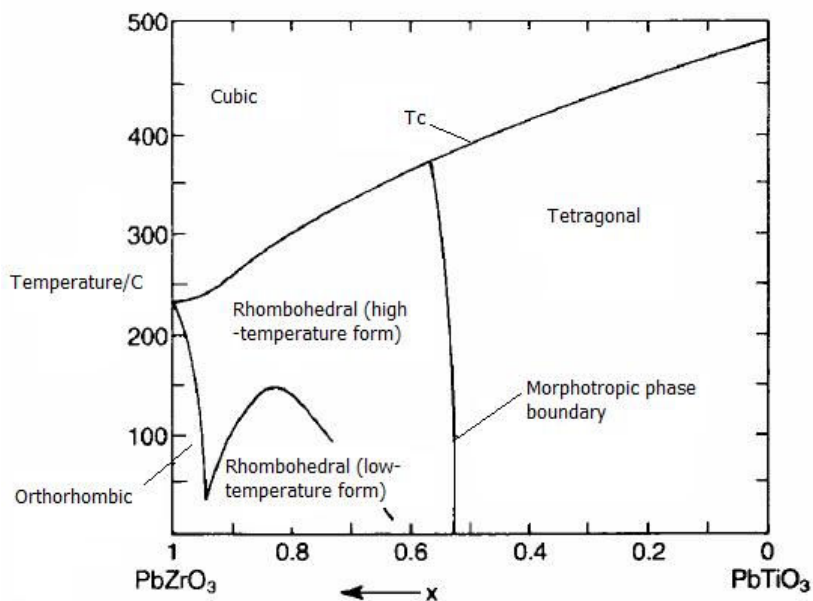


Figure 2.6: Phase diagram of the PZT system [53].

The ratio of Zr/Ti determines the structural type of PZT and the distinct working temperature that is the limit temperature for one of the usage parameters as being piezoelectric for the wide area applications of PZT. The Zr/Ti molar ratio is 1:1 in our experiments within this thesis. The composition of $Pb(Zr_{0.50}Ti_{0.50})O_3$ has approximately a 400 °C working temperature as seen in Figure 2.7. Actually, $Pb(Zr_{0.52}Ti_{0.48})O_3$ shows stronger piezoelectric behavior than $Pb(Zr_{0.50}Ti_{0.50})O_3$. However, we prepared a $Pb(Zr_{0.50}Ti_{0.50})O_3$ solution, due to its simplicity in preparation.



Figure 2.7: Prototype ferroelectric material ($PbTiO_3$) with perovskite structure.

Under the Curie temperature ($T_c$), PZT transforms to a ferroelectric phase with a perovskite type tetragonal crystal structure. As seen in Figure 2.7, due to the position of the Ti atom, the polarization vector of the PZT unit cell changes; thus this change results in a tetragonal ferroelectric structure that is known as a perovskite structure.

PZT is the most widely used ferroelectric material in ultrasonic transducers, non-volatile random access memory devices, microelectromechanical devices, sensors, and actuators applications due to its high dielectric constant, high electromechanical coupling coefficient, and large remnant polarization [54, 55]. This material can be processed into various forms such as bulk ceramics, thin films, and fibers depending on the application area. PZT in fiber form is appealing because of its increased anisotropy, improved flexibility and strength over that of monolithic PZT ceramics. Microscale PZT fibers are usually incorporated into a polymer matrix to obtain smart

piezocomposite structures [56]. They can also be used as individual fibers in novel actuator and sensor devices, such as energy harvesting and self-powered in-vivo medical devices, high-frequency transducers, non-volatile ferroelectric memory devices [57]. Nanoscale PZT fibers are also expected to find wide applications particularly in nanoelectronics, photonics, sensors, and actuators [58].

There are several methods to obtain PZT in fiber form. Sol-gel, dicing of the bulk ceramic, and extrusion, for instance, are applied to produce PZT fibers typically in the micron scale [58-60]. The electrospinning technique has recently received attention because the fibers at micro and even nanoscale can be produced effectively by this method. Nanoscale PZT fibers have been also produced by the electrospinning method [57, 62-64]. Zhou et *al.* [64] have produced PZT nanofibers by electrospinning and found that these fibers exhibit significant reversible piezoelectric strains under applied electric field. The level of this strain was measured to be about 4.2% which is reportedly six times larger than that observed in thin films.

One of the responses of electro-active PZT nanofibers is its dielectric property. Undoped PZT has a substantially higher dielectric constant (800 at 1 kHz) [66]. This dielectric value makes it also a promising ceramic dielectric material for use in electronic areas such as energy storage capacitors.

PZT electro-active nanofibers can be fabricated (e.g. fibers with diameters in a range of tens to hundreds of nanometers) by electrospinning sol-gel precursors and calcinated and sintered the collected fibers at distinct temperatures. It is a promising technique for fabricating ceramic nanofibers and other ceramic nanostructures which have more excellent electrical properties than their bulk forms. Such nanofibers may be used directly as sensors or as actuators in micro-scale or nano-scale devices. With appropriate surface functionalization, nanofiber resonators could be used as biosensors. Furthermore, such nanofibers may be used as active structures in applications for which thin films could not be used.

## 2.2 Method

### 2.2.1 The Novel Technique for Forming Fibrous Mats: Electrospinning

Since the beginning of the 20th century electrostatic forces have been applied to a solution for creating fibers. Rayleigh and Zeleny first independently investigated this novel technique, although the first patent of an electrospinning apparatus was created by Formhals in 1934 [67-70].

Between 1964 and 1969 Taylor developed the fundamental theory of electrospinning [71-73]. Taylor investigated the electrospinning technique by mathematical modeling the shape of the fiber cone formed by the fluid droplet under the effect of an applied electric field. This characteristic droplet shape is now referred as the Taylor cone. Firstly, by applying the electric field, the body of the liquid is charged, and then electrostatic repulsion counteracts the surface tension of the droplet and finally droplet is stretched. A flow of liquid erupts from the surface at a critical point. As indicated before, this point of eruption is called the Taylor cone (Figure 2.8).
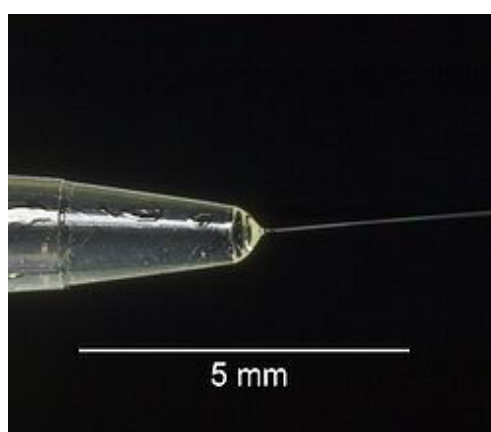


Figure 2.8: Photograph of a meniscus of polyvinyl alcohol in aqueous solution showing a fiber being electrospun from a Taylor cone. Courtesy of [74].

If the molecular cohesion of the liquid is sufficiently high, stream breakup does not occur and then a charged liquid jet is formed. However if it does, droplets are electrosprayed instead. There have been various theoretical developments of the mechanisms of the electrospinning process since 1995. Reznik et *al.* describes comprehensive work on the shape of the Taylor cone and the associated ejection of a fluid jet [75].
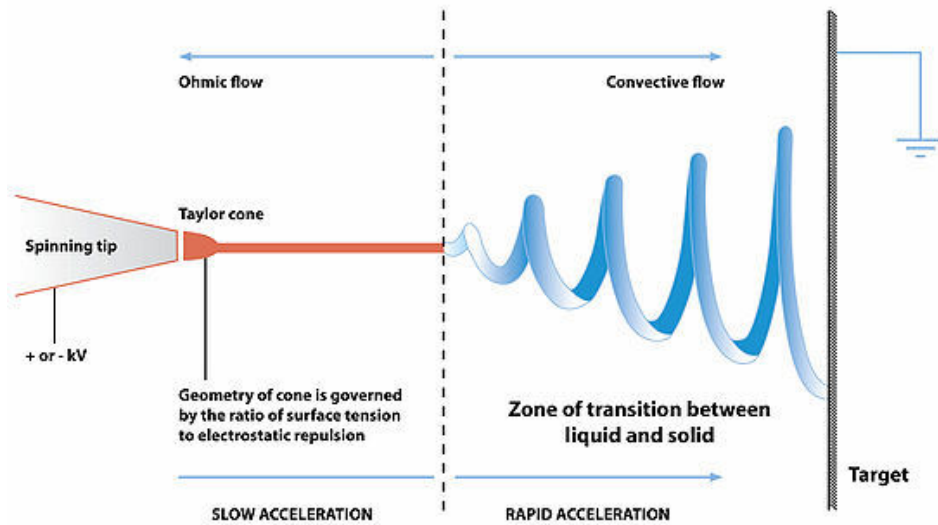


Figure 2.9: Diagram showing fiber formation by electrospinning. Courtesy of [74].

The process of a fiber formation is depicted in Figure 2.9. In the ohmic flow step, a Taylor cone is formed. On the other hand, in a convective flow step, the spiral fiber is formed, and its diameter is reduced significantly due to loss of the solvent-zone of the transition between liquid and solid. Thus, nano to micron scale-fibers are collected on the target typically to form a randomly oriented fiber mat.

In the early 1990s several research groups –specifically, Reneker who popularised the name electrospinning for the process- [76] demonstrated that many polymers could be electrospun into nanofiber form. Then, the number of publications regarding electrospinning has been increasing exponentially year by year [77].

As reported in the open literature, electrospinning has number of parameters such as applied voltage, the syringe diameter, the distance between the tip of the syringe needle and the collector, the viscosity and pumping rate of the polymer solution. Their

effects on the fiber formation has been widely studied for producing polymer or ceramic fibers with nano- to micron-scale diameters, as changing these major parameters, allows adjustment on the size of the fibers.

In recent studies, researchers have attempted to fabricate ceramic particle-reinforced fibers using electrospinning followed by post-spinning treatment [78-80]. The particles were formed in polymeric fibers using a sol-gel method. Their results were impressive, suggesting a uniform distribution of particles in the fiber. However, this sol-gel method is usually followed by a sintering process to oxidize the particles, in order to retrieve the properties of these compounds properly. During the sintering process, the polymer was removed, and enough time was given to enable the sintering of the ceramic grains, resulting in the formation of thin ceramic nanofibers. The disadvantage of this method is the lack of flexibility due to the removal process of polymer.

Electrospun fibers and their corresponding membranes also have their own unique properties, such as average fiber diameters in the nano-scale range, high porosities, large surface areas, and sufficient mechanical strengths. These outstanding properties make electrospun fibers attractive for a wide range of applications such as tissue engineering, wound dressing, military protective clothing, filter media, as well as nanosensor and electronics applications [81].

## 2.3  Nanocomposites

The properties of nanocomposites depend not only on the properties of their individual constituents, but also on their dispersion and interfacial characteristics. The material properties such as brittleness, porosity, hardness, high surface area, polarizibility, conductivity, insulation, light absorption, are often decisive properties for the application of resultant nanocomposites.

The synthesis of polymer nanocomposites (PNCs) is an integrative aspect of polymer nanotechnology. The presence of nanofillers endows the PNCs with unique properties that conventional polymers or polymers with traditional micron-scale fillers do not possess. While the fillers by themselves may be of no practical use, the resultant composites can be used in a variety of scientific and technological applications. As the ability to synthesize materials of nano-scale formations-nanoparticles, nanofibers- using them as fillers in composite materials for new or modified physical properties have become much more appealing. Nano-scale fillers and the associated increase in surface area that introduce more advantageous properties compared to their bulk form and traditional micron-size fillers. As indicated in several scientific articles, the nano-scale particles/fillers embedded into polymers would lead to intriguing electrical properties of composites [82, 84]. Polymeric nanocomposites of high dielectric response, for instance, are considered in a variety of high-$k$ electronics applications and electronic coupling devices, such as transducers, piezo-sensors, hydrophones [85] and in making electromagnetic antennas. It has also been noted that the composite properties depend on the size, geometry and surface quality of the filler materials and could be tailored if the dispersion of the fillers is controlled [82]. Hong et *al.* [82] studied dielectric response of ZnO/LDPE composite material and the effect of the ZnO filler particle size and spatial distribution. Just recently, dielectric properties of radial-ZnO/PVDF composites were reported by Wang et *al.* [83]. They highlighted the effect of percolation and the morphology of the fillers. Their results demonstrated that the significant increase of dielectric response can be achieved by the addition of R-ZnO fillers into the polymer matrix provided that the filler volume fraction is below the percolation threshold.

## 2.4 References

[1] Rankin, C.; Chou, C.-H.; Conklin, D.; Bonnell, D. A. Polarization and Local Reactivity on Organic Ferroelectric Surfaces: Ferroelectric Nanolithography using Poly (vinylidene fluoride), *ACS Nano*, 1, 2007, 234-238.

[2] Geschke, D.; Leister, N.; Steffen, M.; Glasel, H. J.; Hartmann, E. Pyroelectric measurements on BaTiO3 / polymer composites by using laser intensity modulation method, *J. Mater. Sci. Lett.*, 16, 1997, 1943-1947.

[3] Wada Y.; Hayakawa R., Piezoelectricity and Pyroelectricity of Polymers, *Jpn. J. Appl. Phys.*, 15, 1976, 2041-2057.

[4] Ryu, J.; Park, J.; Kim, B.; Park, J.-O. Design and fabrication of a largely deformable sensorized polymer actuator, *Biosensors and Bioelectronics*, 21, 2005, 822–826.

[5] Jiang, Y.; Ye, Y.; Yu, J.; Wu, Z.; Li, W.; Xu, J.; Xie, G. Study of thermally poled and corona charged poly(vinylidene fluoride) films, *Polym. Eng. Sci*, 47, 2007, 1344–1350.

[6] Dargaville, T. R.; Celina, M. C.; Elliott, J. M.; Chaplya, P. M.; Jones, G. D.; Mowery, D. M.; Assink, R. A.; Clough, R. L.; Martin, J. W. Verification and Operation of Adaptive Materials in Space, *Sandia National Laboratories,* 2006.

[7] Kawai, H. The Piezoelectricity of Polyvinylidene Fluoride, *Jpn. Appl. Phys*, 8, 1969, 975.

[8] Fuhrmann, J.; Hofmann, R.; Streibel H.J.; Jahn, U. Electron Injection at PVDF/Metal Interfaces, *IEEE Transactions on Electrical Insulation,* 3, 1986.

[9] Reddy, P. J.; Sirajuddin, M. Pyroelectric polymer films for infrared detection, *Bulletin of Materials Science*, 8, 1986.

[10] Osaki, S. High Temperature Dielectric Anisotropy of Poly(vinylidene fluoride) Films at Microwave Frequencies, *J. Polym. Sci.*, *B,* 33, 1995, 685.

[11] Jow, T.R.; Cygan, P.J. Anomalous Metal-Polymer Interface Dependence of Dielectric Breakdown in Polyvinylidene Fluoride, *J. Appl. Phys*, 73, 1993, 5147.

[12] Elashmawi, I.S.; Hakeem, N.A. Spectroscopic, thermal, and electrical investigations of PVDF films filled with BiCl$_3$, *Journal of Applied Polymer Science*, 102, 2006, 2125–2131.


[13]    http://repositorium.sdum.uminho.pt/bitstream/1822/5170/1/872-876.pdf    last accessed on March 1, (2008).


[14] Seol, W.-H.; Lee, Y. M.; Park, J.-K.  Enhancement of the mechanical properties of PVdF membranes by non-solvent aided morphology control, *Journal of Power Sources,* 170, 2007, 191–195.


[15] Mhalgi, M. V.; Khakhar, D. V.; Misra, A. Stretching induced phase transformations in melt extruded poly(vinylidene fluoride) cast films:Effect of cast roll temperature and speed, *Polym. Eng. Sci*, 47, 2007, 1992–2004.


[16] Cebet, P.; Grubb, D.T. High-temperature dielectric relaxation in α- and γ-phase poly(vinylidene fluoride), *Macromolecules*, 17, 1984, 1374–1384.


[17] Mago, G.; Kalyon, D. M.; Fisher, F. T. Membranes of Polyvinylidene Fluoride and PVDF Nanocomposites with Carbon Nanotubes via Immersion Precipitation, *Journal of Nanomaterials*, 8, 2008.


[18] Pawlowski, K. J.; Belvin, H. L.; Raney, D. L., Su J., Harrison, J. S.; Siochi, E. J. Electrospinning of a micro-air vehicle wing skin, *Polymer*, 44(4), 2003, 1309-1314.


[19] Kwan Chi Kao, Dielectric Phenomena in Solids, With Emphasis on Physical Concepts of Electronic Process, Academic Pr., 2004.


[20] http://www.doitpoms.ac.uk/tlplib/pyroelectricity/pvdf.php last accessed on March 1, (2008).


[21] Pallathadka, P. K.; Tay, S.S. Solid state ^{19}F NMR study of crystal transformation in PVDF and its nanocomposites, *Polym. Eng. Sci.*, 46, 2006, 1684–1690.


[22] Andrew, J. S.; Clarke, D. R. Enhanced Ferroelectric Phase Content of Polyvinylidene Difluoride Fibers with the Addition of Magnetic Nanoparticles, *Langmuir*, 24 (16), 2008, 8435–8438.


[23] Harrison, J. S.; Ouniaes, Z. Piezoelectric Polymers. NASA Langley Research Center, 2001, 43, NASA/CR-2001-211422.

[24] Chung, M.Y.; Lee, D.C. Electrical Properties of Polyvinylidene Fluoride Films Prepared by the High Electric Field Applying Method, *Journal of the Korean Physical Society*, 38, 2, 2001, 117-122.

[25] Kułek, J.; Hilczer, B. The Effect of Dielectric Heterogeneity on the Pyroelectric Response of PVDF, *IEEE Transactions on Dielectrics and Electrical Insulation*, 5, 1998.

[26] Choi, S. S. Electrospun PVDF nanofiber web as polymer electrolyte or separator, *Electrochimica Acta*, 50(2), 2004, 339-343.

[27] Kim, J. R. Electrospun PVDF-based fibrous polymer electrolytes for lithium ion polymer batteries, *Electrochimica Acta,* 50(1), 2004, 69-75.

[28] Roy, S.; Basu, S. Improved zinc oxide film for gas sensor applications, *Bulletin of Materials Science*, 25(6), 2002, 513-515.

[29] Zhang, Q.; Chou, T. P; Russo, B.; Jenekhe, S. A.; Cao, G. Polydisperse Aggregates of ZnO Nanocrystallites: A Method for Energy-Conversion-Efficiency Enhancement in Dye-Sensitized Solar Cells, *Advance Materials,* 18, 2008, 1654-1660.

[30] Pal, B.; Sharon, M. Enhanced photocatalytic activity of highly porous ZnO thin films prepared by sol–gel process, *Materials Chemistry and Physics*, 76, 2002, 82-87.

[31] Xu, C. X.; Sun, X. W. ; Chen, B. J.; Shum, P. Nanostructural zinc oxide and its electrical and optical properties, *Journal of Applied Physics*, 95(2), 2004, 661-666.

[32] Viswanathamurthi, P.; Bhattarai, N.; Kim, H. Y.; Lee, D. R. The photoluminescence properties of zinc oxide nanofibres prepared by electrospinning, *Nanotechnology*, 14, 2004, 320-323.

[33] Martin, P. M.; Good, M. S.; Johnston, J. W.; Bond, L. J.; Lin J. D. Piezoelectric films for 100MHz ultrasonic transducers, *Thin Solid Films*, 379, 2000, 253-258.

[34] Zhang, Q.; Chou, T.P; Russo, B.; Jenekhe, S.A.; Cao, G. Polydisperse Aggregates of ZnO Nanocrystallites: A Method for Energy-Conversion-Efficiency Enhancement in Dye-Sensitized Solar Cells, *Advance Materials,* 18, 2008, 1654-1660.

[35] Wang, L. Z.; Kong, X. Y.;  Ding, Y.; Gao, P.; Hughes, W. L.; Yang, R.; Zhang, Y. Semiconducting and piezoelectric oxide nanostructures induced by polar surfaces, *Advance Materials*, 14, 2004, 10.

[36] Zhao, M. H.; Wang, Z. L.; Mao, S. X. Piezoelectric characterization of individual zinc oxide nanobelt probed by piezoresponse force microscope, *Nano Letters*, 4(4), 2004, 587-590.

[37] Mbenkum, B. N.; Ashkenov, N. Schubert, M.; Lorenz, M.; Hochmuth, H. D.; Michel, M.; Grundmann, M. Temperature-dependent dielectric and electro-optic properties of a ZnO-BaTiO3-ZnO heterostructure grown by pulsed-laser deposition, *Journal of Applied Physics. Letters,* 86, 2005, 091904-1.

[38] Nandi, S. K.; Chatterjee, S. S.; Samanta, K. G.; Dalapati, K.; Bose, P. K.; Varma, S.; Shivprasad, P.; Maiti, C. K. Electrical properties of Ta2O5 films deposited on ZnO *Bull. Mater. Sci.,* 26(4), 2003, 365-369.

[39] IEEE Micro Electro Mechanical Systems Workshop, Jan-Feb 1991, Nara, Japan, p.118.

[40] http://cst-www.nrl.navy.mil/lattice/struk.picts/b4.s.png last accessed on January 1, (2008).

[41] Gao, P. X.; Wang, Z. L. Nanoarchitectures of semiconducting and piezoelectric zinc oxide, *Journal of Applied Physics.,* 97, 2005, 044304.

[42] Wang, Y. C.; Leu, I. C.;  Hon, M. H. Deposition Characteristics of ZnO Nanowire Arrays by Electrophoretic Deposition *Electrochemical Solid State Letters,* 237-239(1), 2002, 564-568.

[43] Li, Y.; Meng, G. W.; Zhang, L. D.; Philipp, F. Ordered semiconductor ZnO nanowire arrays and their photoluminescence properties, *Applied Physics Letters*, 76, 2001, 2011-2013.

[44] , Muthukumar, S.; Sheng, H,; Zhong, J.; Zhang, Z.; Emanetoglu, N.W., Lu, Y. Selective MOCVD growth of ZnO nanotips, *Nanotechnology,* 2, 2003.

[45] Kim, C.; Yang, K.; Kojima, M.; Yoshida, K.; Kim, Y. J.; Kim, Y.; Endo, M. Fabrication of electrospun-derived carbon nanofiber web for the anode material of lithium-ion secondary batteries, *Advanced Functional Materials*, 16, 2006, 2393-2397.

[46] Kim, H. W.; Kim, E.; Knowles, J. C. Production and potential of bioactive glass nanofibers as a next-generation biomaterial, *Advanced Functional Materials*, 16, 2006, 1529-1535.

[47] Chronakis, I. S. Novel nanocomposites and nanoceramics based on polymer nanofibers using electrospinning process – Review, *Journal of Materials Processing Technology*, 167, 2005, 283-293.

[48] Sigmund, W.; Yuh, J.; Park, H.; Maneeratana, V.; Pyrgiotakis, G.; Daga, A.; Taylor, J.; Nino, J. C. Processing and structure relationships in electrospinning of ceramic fiber systems, *Journal of American Ceramic Society*, 89(2), 2006, 395-407.

[49] Wang, Y.; Aponte, M.; Leon, N.; Ramos, I.; Furlan, R.; Pinto, N. Synthesis and characterization of tin oxide micro/nano fibers using electrospinning, *Journal of American Ceramic Society*, 88(8), 2005, 2059-2063.

[50] Wu, H.; Pan, W. Preparation of Zinc Oxide Nanofibers by Electrospinning, *Journal of American Ceramic Society*, 89, 2006, 699.

[51] Dzenis, Y. A. Spinning Continuous Fibers for Nanotechnology Science, 304, 2004, 1917.

[52] Kim, Y.; Lee, D. Y.; Lee, M.-H.; Cho, N.-I.; Song, Y.-S.; Lee, S.-J. Characterization of Electrospun ZnO Nanofibers, *Journal of the Korean Physical Society,* 53(1), 2008, 421-425.

[53] Cross. L. E. Ferroelectric Ceramics-Tutorial Reviews, Theory, Processing and Applications, N. Setter, and E. L. Colla, ed., 1 (Birkhauser Verlag, Basel) 1993.

[54] Maeda, R.; Tsaur, J. J.; Lee S. H.; Ichiki, M. Effect of multi-coating process on the orientation and microstructure of lead zirconate titanate (PZT) thin films derived by chemical solution deposition, *J. Electroceram.,* 12, 2004, 89.

[55] Setter, N.; Waser, R. Electroceramic materials, *Acta Mater.,* 48, 2000, 151.

[56] Ouellette, J. How smart are smart materials?, *The Industrial Physicist,* 2,1996, 10.

[57] Xu, S.; Shi, Y.; Kim, S. Fabrication and mechanical property of nano piezoelectric fibers, *Nanotechnology*, 17, 2006, 4497-4501.

[58] Zhang, X. Y.; Zhao, X.; Lai, C. W.; Tang, X. G.; Dai., J. Y. Synthesis and piezoresponse of highly ordered $Pb(Zr_{0.53}Ti_{0.47})O_3$ nanowire arrays, *Appl. Phys. Lett.,* 85, 2004, 4190.

[59] Meyer, Jr. R.; Shrout T.; Yoshikawa, S. Lead zirconate titanate fine fibers derived form alkoxide-based sol-gel technology, *J. Am. Ceram. Soc.,* 81 [4], 1998, 861-868.

[60] Zhang, M.; Salvado, I. M. M.; Vilarinho, P. M. GC-MS and 13C NMR investigation of lead zirconate titanate precursor sols for fiber preparation, *J. Am. Ceram. Soc.,* 90 [2], 2007, 358-363.

[61] Kitaoka, K.; Kozuka H.; Yoko, T. Preparation of lead lanthanum zirconate titanate (PLZT, (Pb,La)(Zr,Ti)$O_3$ fibers by sol-gel method, *J. Amer. Ceram. Soc.,* 81 [5], 1998, 1189-1196.

[62] Wang, Y.; Furlan, R.; Ramos, I.; Santiago-Aviles, J. J. Synthesis and characterization of micro/nanoscopic Pb($Zr_{0.52}Ti_{0.48}$)$O_3$ fibers by electrospinning, *Appl. Phys. A*, 78, 2004, 1043-1047.

[63] Dharmaraj, N.; Kim, C. H.; Kim, H. Y. Pb($Zr_{0.5}Ti_{0.5}$)$O_3$ nanofibres by electrospinning, *Mat. Lett.* 59, 2005, 3085-3089.

[64] Sigmund, W.; Yuh, J.; Park, H.; Maneeratana, V.; Pyrgiotakis, G.; Daga, A.; Taylor J. Nino, J. C. Processing and Structure Relationships Electrospinning of Ceramic Fiber Systems, *J. Am. Ceram. Soc.*, 89 [2], 2006, 395-407.

[65] Zhou, Z. H.; Gao, X. S.; Wang, J.; Fujihara, K.; Ramakrishna S.; Nagarajan, V. Giant strain in Pb($Zr_{0.2}Ti_{0.8}$)$O_3$ nanowires, *Appl. Phys. Lett.,* 90, 2007, 052902.

[66] Lee, B.; Lee, J., Effects of complex doping on microstructural and electrical properties of PZT ceramics, *Electroceram.,* 17, 2-4, 2006, 597-602.

[67] Huang, Z. M.; Zhang, Y. Z.; Kotaki, M. A Review on Polymer Nanofibers by Electrospinning and their Applications in Nanocomposites, *Composites Science and Technology,* 63(15), 2003, 2223-2253.

[68] Subbiah, T.; Bhat, G.; Tock, R.; Electrospinning of Nanofibers, *Journal of Applied Polymer Science,* 96(2), 2005, 557-569.

[69] Teo, W.; Ramakrishna, S., A Review on Electrospinning Design and Nanofibre Assemblies, *Nanotechnology*, 17(14), 2006, R89-R106.

[70] Reneker, D. H.; Yarin, A. L.; Fong, H. Bending Instability of Electrically Charged Liquid Jets of Polymer Solutions in Electrospinning, *Journal of Applied Physics*, 87, 2000, 4531.

[71] Taylor, G. Disintegration of Water Drops in an Electric Field. *Proceedings of the Royal Society of London A: Mathematical, Physical & Engineering Sciences,* 280, 1964, 383-397.

[72] Taylor, G. The force exerted by an electric field on a long cylindrical conductor. *Proceedings of the Royal Society of London A: Mathematical, Physical & Engineering Sciences,* 291, 1965, 145-158.

[73] Taylor, G. Electrically Driven Jets. *Proceedings of the Royal Society of London A: Mathematical, Physical & Engineering Sciences*, 313, 1969, 453-475.

[74] http://en.wikipedia.org/wiki/Electrospinning last accessed on May 1, (2007).

[75] Reznik, S. N.; Yarin, A. L.; Theron, A; Zussman, E. Transient and steady shapes of droplets attached to a surface in a strong electric field, *Journal of Fluid Mechanics*, 516, 2004, 349-377.

[76] Doshi, J.; Reneker, D. H. Electrospinning Process and Applications of Electrospun Fibers, *Journal of Electrostatics*, 35, 1995, 151-160.

[77] Li, D.; Xia. Y. Electrospinning of Nanofibers: Reinventing the Wheel?. *Advanced Materials.* 16, 2004, 1151-1170.

[78] Viswanathamurthi, P.; Bhattarai, N.; Kim, C. K.; Kim, H. Y.; Lee, D. R. Ruthenium doped TiO2 fibers by electrospinning, *Inorganic Chemistry Communications,* 7(5), 2004, 679.

[79] Madhugiri, S.; Sun, B.; Smirniotis, P. G.; Ferraris, J. P.; Balkus, J. K. J. Electrospun mesoporous titanium dioxide fibers, *Microporous and Mesoporous Materials*, 69(1-2), 2004, 77.

[80] Viswanathamurthi, P.; Bhattarai, N.; Kim, H. Y.; Khil, M. S.; Lee, D. R.; Suh, E. K. GeO2 fibers: preparation, morphology and photoluminescence property, *J. Chem. Phys.* 121(1):441, 2004, 445.

[81] Choi, S. W.; Kim, J. R.; Ahn, Y. R.; Jo, S. W.; Cairns, E. J. Characterization of Electrospun PVdF Fiber-Based Polymer Electrolytes, *Chem. Mater.,* 19, 2007, 104-115.

[82] Hong, J. I.; Winberg, P.; Schadler, L. S.; Siegel, R.W. Dielectric properties of zinc oxide / low density polyethylene nanocomposites, *Materials Letters*, 59, 2005, 473-476.

[83] Wang, G.; Deng, Y.; XiangY.; Guo, L.; Fabrication of radial ZnO nanowire clusters and radial ZnO/PVDF composites with enhanced dielectric properties, *Advanced functional materials,* 18, 2008, 2584-2592.

[84] Lewis, T. J. Nano-Composite Dielectrics: The Dielectric Nature of the Nano-Particle Environment, *IEEJ Transactions on Fundamentals and Materials,* 126 (11), 2006, 1020-1030.

[85] Chiang, C. K.; Popielarz, R. Polymer composites with high dielectric constant, *Ferroelectrics,* 275, 2002, 1–9.

**CHAPTER 3**

**3 PAPER-1**

**The Effect of Processing and Crystallinity Upon Dielectric Behavior of PVDF**

Paper-1 was submitted to the Journal of Applied Polymer Science.

Road map of the paper-1 is given above.

EXPERIMENTAL

Electrospinning of polymer solution

Making polymer pellets

Melt casting of polymer pellets

20% w/w homopolymer PVDF (CAS:24937-79-9 Alfa Aesar) and 1:1 volume mixture of acetone and N,N dimethylformamide (DMF, Aldrich)
Voltage: 12 kV
Distance: 22,5 cm

Specac Cold Press

Pressure:170 MPa
Mass: 10 g PVDF
Diameter of the press holder: 6 mm

Home-made Hot Press

Temperature: 180 $^{o}$C
Pressure: 19 MPa
Under pressure until cooling down to room T.

CHARATERIZATION

SEM

**Crystallinity by DSC**

**Crystalline Phases by XRD**

Dielectric Analysis
Temperature: 30-150 $^{o}$C
Frequency: 100 Hz-1 MHz

# The Effect of Processıng and Crystallinity Upon Dielectric Behavior of PVDF

Canan Dagdeviren[1], Mustafa Okutan[2], Sait Eren San[2], Melih Papila[1]

*1- Sabancı University, Faculty of Engineering and Natural Sciences, Material Science and Engineering, Tuzla, Istanbul, 34956 (Turkey)*

*2- Gebze Institute of Technology, Department of Physics, Gebze, Kocaeli, 41400 (Turkey)*

## 3.1 ABSTRACT

In this study the dielectric behavior of PVDF is investigated along with its dependence on the crystalline structure that varies with processing of the polymer. Cold press pellet, melt cast film and electrospun (e-spun) fibrous mat are tested to determine the effect of different processes and the crystallinity upon the dielectric properties of PVDF. The results indicate a negative correlation between the crystallinity and dielectric response. Specifically, the dielectric response decreases while the crystallinity increases in the following order: e-spun fibrous mat, melt cast film and cold press pellet. Cole-Cole plots are also reported to investigate the relaxation frequencies as a part of the relations with the crystallinity of the samples. The Cole-Cole plot distribution parameter; $\alpha$, values suggest that the dielectric behavior of the samples is a high-frequency relaxation process with non-Debye-type behavior. This behavior is attributed to the dipolar rotation around the long molecular axis. The distribution parameter values also suggest that dipolar rotation in the melt cast sample decreases with the elevated temperature. The $\alpha$ values remain around the same level in the e-spun specimen that is lower than for the melt-cast. The stable dipolar rotation behavior of the e-spun sample is attributed to the higher crystallinity.

**Key words:** PVDF, dielectric characterization, cystallinity, electrospinning.

**3.2 INTRODUCTION**

Poly(vinylidene fluoride), PVDF, is a pure, thermoplastic fluoropolymer possessing technologically attractive properties, such as being ferroelectricity [1-3], pyroelectricity [3, 4], bio-compatibility [5], and chemically resistivity [6]. The glass transition temperature of PVDF is typically around -40 °C, such that at room temperature, the polymer is flexible with durable, highly elastic and lightweight properties [7]. Due to these properties, PVDF and its copolymers have been widely studied [8-14]. Among the polymer materials, PVDF has a high dielectric constant ($\varepsilon_r$ = 11-14) and high dc dielectric strength ($E_{bd}$ = 770 MV/m) [14, 15], which make it also a promising polymeric dielectric material for use in energy storage capacitors.

The physical properties of the semicrystalline polymers depend upon the processing conditions and the resulting crystal morphology developed within the processed sample [7, 16]. In its solid state, PVDF is also a semi-crystalline material with approximately 50% crystallinity that is known to change as a function of the processing [17]. There are several polymorphs of this polymer, with four of them being well understood and described in the literature: α, β, γ, and δ, or phases II, I, III, IV respectively [3, 16, 18-23]. The proportions of the phases also depend on the method of preparation [24, 25]. Non-polar trans-gauche–trans-gauche (TGTG) conformation, $\alpha$-phase, for instance, is readily formed on cooling the melt and on solution casting, whereas the polar, slightly twisted, planar zigzag all-trans (TTTT) conformation, $\beta$-type typically requires transformation from TGTG by mechanical stretching [26, 27], and electrical poling. The polymer chains with trans-gauche (TG) conformation in the $\alpha$-phase are stacked with their respective polarization in alternating directions, resulting in a nonpolar phase and paraelectric behavior [22]. The $\beta$-phase, on the other hand, has an all-trans zigzag chain conformation and parallel dipole moments, and thus is the polar phase with a large, spontaneous polarization resulting in ferroelectricity and piezoelectricity [22]. The typical dominant phase is the $\alpha$-phase, as it is the most stable phase at room temperature [23]. However, $\beta$-phase PVDF is often preferred as in sensor applications [28].

Dielectric relaxation in PVDF polymer is influenced by its complex structure, both at the molecular and the crystalline level. The degree of the crystallinity as well as the size of the crystallites and the lamella thickness may be influenced either by externally applied electric field and mechanical stress or by the thermal treatment. It should be noted also that (B. Hilczer et *al*. [25]) the space charge built up near the interface of the crystallites and amorphous matrix results in a change of dielectric relaxation, thereby hindering the molecular motions [29]. For example, charges pile up in the volume or on the surface of the material, predominantly due to charge in conductivity that occurs at boundaries, imperfections such as cracks and defects, and boundary region between the amorphous and crystalline regions within the same polymer. In this respect, this kind of polarization is different from the three dielectric mechanism, namely, the electronic, orientational and atomic polarization, all of which are due to displacement of bound charges. Interfacial polarization, also known as space charge polarization arises as a result of accumulation of charges locally as they drift through the material. In the case of interfacial polarization large scale distortions of the field takes place. The atoms and molecules within the polymer are subjected to a locally distorted electric field that is the sum of the applied field and various distortion mechanism apply.

This work is mainly focused on the dielectric behavior of PVDF and its dependence on the crystalline structure that may vary upon the processing of the polymer. Three different processes were employed to prepare the PVDF samples: e-spun, melt casting and cold press casting. These processes are described in the next section, followed by the dielectric characterization of the PVDF samples under various frequencies and temperatures, along with the crystalline structure. Supporting evidence for the results and associated discussions regarding the correlation of the dielectric properties and the crystallinity of PVDF are provided by the x-ray diffractometry (XRD), differential scanning calorimetry (DSC) and scanning electron microscopy (SEM). The Cole-Cole plots are also presented for interpreting the dielectric mechanism.

31

## 3.3 EXPERIMENTAL

*Electrospinning of the polymer solutions:* In a homemade electrospinning set-up, as depicted in Figure 3.1, a polymer solution is placed in a syringe that has a nozzle diameter of 300 micrometer. The solution is charged by a high voltage power supply, typically at 5 to 15kV, while a grounded collector is placed at a specified distance. The rate of the polymer flow from the syringe is continuously controlled by a syringe pump (New Era NE-1000 Syringe Pump along with Pumpterm Software) and an RS-232 unit linking the experimental set-up and a computer [30, 31]. Under the applied electric field, the polymer solution is ejected from the nozzle towards the collector due to high electrostatic force acting on the polymer droplet at the tip of the nozzle. As the polymer jet travels in air, the fiber is formed, and its diameter is reduced significantly due to loss of the solvent. Randomly oriented fibers are typically collected on the grounded target plate (collector) and depending on the process parameters a mat of nano to micron scale-fibers is produced.
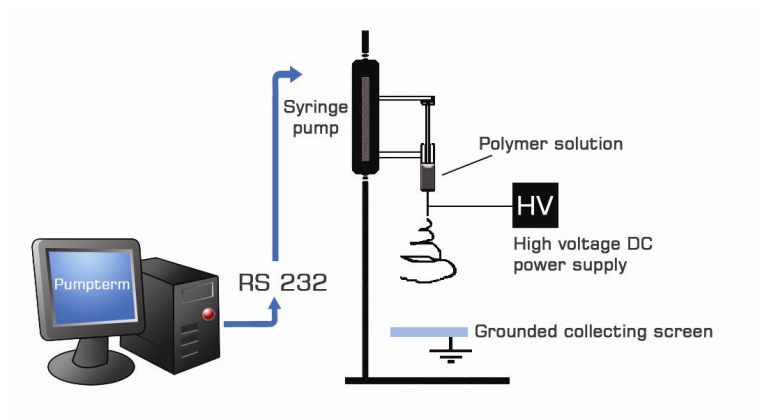


**Figure 3.1:** Schematic representation of the computer controlled electro-spinning setup [31].

The electrospinning polymer solution in this research contains 20% w/w homopolymer of PVDF (CAS: 24937-79-9 Alfa Aesar) within 1:1 volume mixture of acetone and N,Ndimethylformamide (DMF, Aldrich). The use of acetone is to generate high surface tension and solubility of the polymer. Such a surface tension is essential in the electrospinning, because if it is too low, the polymer solution leaves the needle at a high and uncontrolled rate, and the process becomes one of electro-spraying, rather than

electro-spinning. The solvent DMF, on the other hand, relaxes the produced fibers to reach the conducting surface because the DMF molecule has double bonds, leading to partial electrical conductivity due to the delocalization of electrons. DMF also alters the surface tension and the viscosity of the solution, yielding a more homogeneous solution [22]. For each electrospinning trial, a syringe of 2 ml capacity was filled with the polymer solution. The voltage applied to the needle was 12kV, which was supplied by a high voltage generator (Van de Graff). The distance from the nozzle tip to the collector and the pumping rate were 22.5 cm and 2ml/hour, respectively.

*Making the polymer pellets:* A Specac Cold Press was used to make the PVDF pellets by applying approximately 170 MPa on 10 g of poly(vinylidene fluoride) powder, which is placed in a cold press holder of 6 mm diameter.

*Melt casting the polymer pellets:* Home-made hot press molding was used to make the melt cast PVDF film from cold pressed pellets. The temperature of the heating elements was increased to 180 °C, and a pressure of about 19 MPa was applied by the molding blocks. The casting time at 180 °C was about 1 hour, and the molded PVDF film was kept under pressure until cooled down to room temperature.

## 3.4 RESULTS and DISCUSSIONS

The poly(vinylidene fluoride) samples produced by the three processes described above were characterized for morphology, crystalline structure, and dielectric behavior in support of scanning electron microscopy (SEM), x-ray diffractometry (XRD), differential scanning calorimetry (DSC) and dielectric spectroscopy.

## 3.4.1 Morphology by Scanning Electron Microscopy

Scanning electron microscope (LEO SUPRA 35VP) was used to investigate the morphology of the PVDF samples by cold pellet casting, melt casting, and electrospinning techniques. Figure 3.2 shows images from the three samples. Cold pellet pressing yielded PVDF particles of about 300 nm in a compacted form, although

the particulate structure was still retained (Fig. 3.2*a*). Heat was applied on the same pellets until the PVDF reached the melting temperature, while a simultaneous pressure enabled the particles to infuse into one another. Figure 3.2 b also shows that peeling from the surface of the melt cast film occurred while de-molding. A substantial difference in morphology was obtained by electrospinning as it resulted in fibrous formations. It is worth noting that the surface of the fibers is not smooth due to begin decorated by spherical particles of ~300 nm in diameter. These particles appear to be similar, particularly in terms of size, to the particles on the cold pellet sample as shown in Figure 3.3.



(a)                                                          (b)



(c)
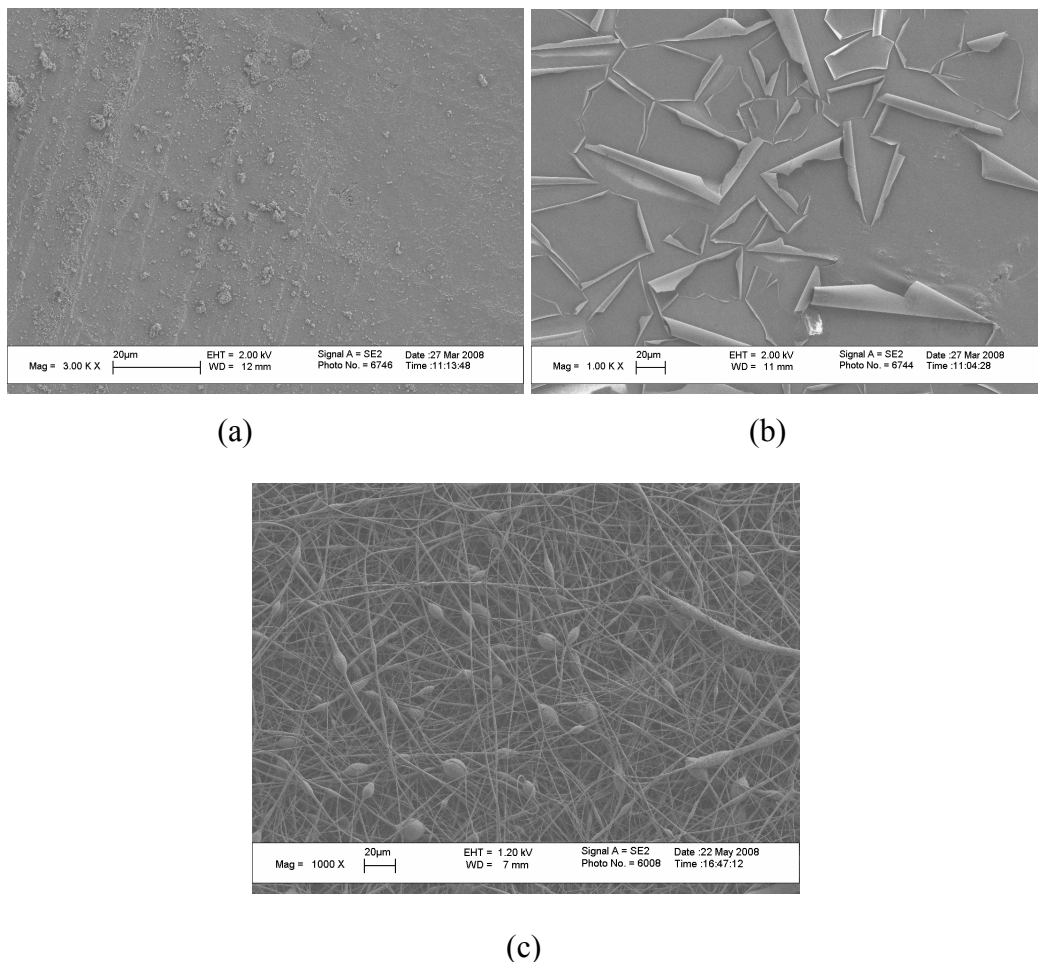
**Figure 3.2:** SEM images of samples a) cold pellet b) melt cast and c) e-spun.

(a)                                                                                  (b)
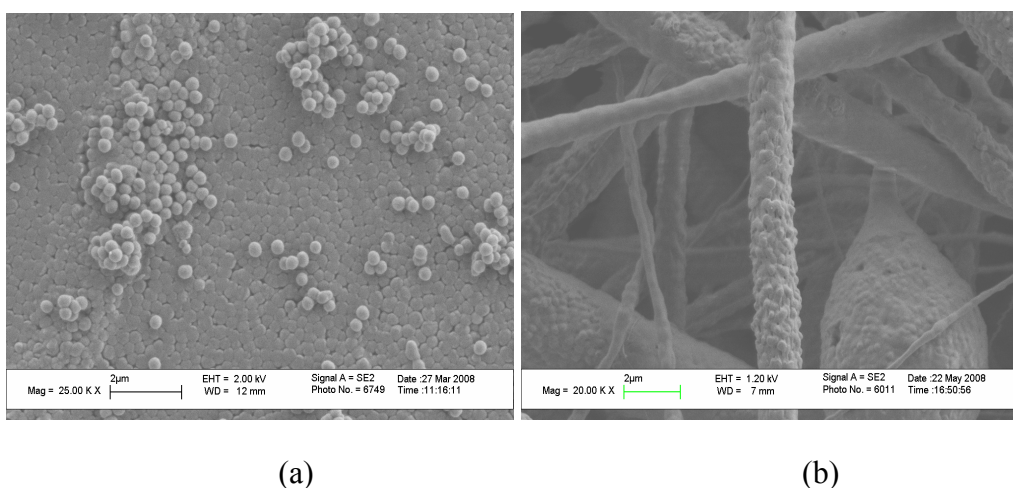
**Figure 3.3:** PVDF particles on a) cold pellet and b) e-spun samples.

## 3.4.2 Crystallinity Measurements by Differential Scaning Calorimetry

The differential scanning calorimeter (DSC) (Netzsch DSC 204 Phoenix) was used to determine the percent crystallinity of the PVDF samples. Two heating and cooling cycles were performed on each sample. At each cycle, the samples were heated, beyond the melting point up to 200 °C, at a rate of 10 °C /min and cooled down to room temperature, at the same rate. While the first cycle is expected to reflect the effect of processing on the crystallinity, the second cycle should demonstrate the pristine crystallographic state of PVDF that is presumed to result in following the first melting with no subsequent morphological changes. In order to calculate the percent crystallinity of the samples, a heat of fusion for 100% crystalline PVDF film is also needed, and its theoretical value is 105 J/g [20, 32]. Table 3.1 summarizes the DSC data, which includes melting temperature, and associated crystallinity values for the three different samples. The total crystallinity of the samples at $1^{st}$ and $2^{nd}$ DSC cycles is also shown in Figure 3.4.

|  | **Pellet** | **Melt cast film** | **E-spun** |
|---|---|---|---|
| **1.cycle** $\Delta H_{meas}$ **(J/g)** | 52.8 | 58.9 | 62.7 |
| **Crys%** | 50.2 | 56.1 | 59.7 |
| **Melting point** °C | 159.5 | 160.0 | 156.4 |
| **2.cycle** $\Delta H_{meas}$ **(J/g)** | 52.2 | 50.5 | 53.3 |
| **Crys%** | 49.7 | 48.1 | 50.7 |
| **Melting point** °C | 159.5 | 158.3 | 158.3 |

**Table 3.1:** DSC data of the PVDF samples. Crystallinity data are computed with respect to theoretical heat of fusion value for 100% crystalline PVDF is $\Delta H_{theo} = 105$ J/g

[20, 32]. Crys% = $\Delta H_{meas} / \Delta H_{theo}$ .
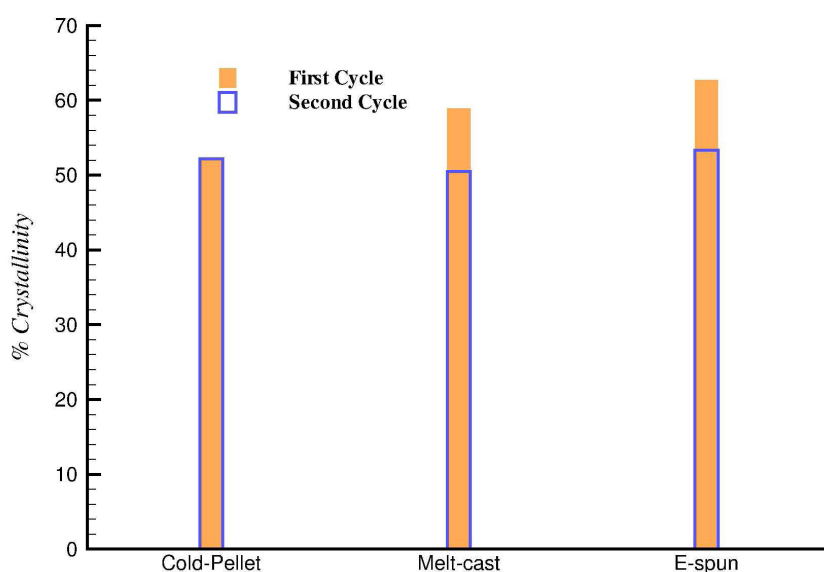


**Figure 3.4:** Total crystallinity of the samples at 1ˢᵗ and 2ⁿᵈ DSC cycles.

For the cold press pellet sample, we used as is PVDF powder and did not perform any prior heating and/or other process on the sample. The two cycles of DSC performed on the cold-pressed pellet specimen also show that there is no significant difference in the crystallinity percentage, as anticipated. For the e-spun and melt cast samples, in contrast, the crystallinity difference between the two cycles suggests that both procedures increase the total crystallinity. It appears that casting under high pressure

when the sample is in a molten state resulted in higher total crystallinity as compared to cold pressing, Crys% = 56% and 50%, 48% at end with respect to that obtained by hot press melt casting. The highest Crys% measured on the e-spun sample is consistent with the comparison of e-spun and raw PVDF samples results reported in the work of Zhao [33]. This increase is attributed to the effect of electrostatic force within the electrospinning process, which can induce mechanical stretching (typically done on the commercial piezoelectric PVDF films) and associated changes in the crystalline structure. The melting points measured at the completion of the first cycles also indicate the effect of the processing. The lowest melting temperature was for the electrospun fibers, at 156 °C. The melting point of the second cycle is higher than the melting point of the first cycle, suggesting that the increased $\beta$-phase content, which was expected for the crystalline structure due to electrospinning, had led to a decrease in the melting temperature. These results based on the DSC analyses confirm that the crystallinity of the PVDF significantly depends on the process conditions and thermal history of the PVDF, as was also noted in Harrison et *al*. [23].

**3.4.3 Crystalline Phases Determined by X-Ray Difractometry**

X-ray diffraction (XRD) (Bruker AXS D8) was utilized to observe the distinct crystalline phases of PVDF samples. In particular, the diffraction angle ($2\theta$) peaks associated with the $\alpha$-phase and $\beta$-phase were noted in XRD graphs shown in Figure 3.5. It was found that the crystalline phase peaks of PVDF depended on the conditions of crystallization: crystalline transformations when crystallized from melt polymer or amorphous solid polymer [34]. The heat of fusion by DSC shows that electrospinning method increases the percentage of cystallinity. The presence of the distinct and dominating peaks of the pellet, melt cast and e-spun PVDF samples were between 14.04 and 25.52, 17.54 and 26.54, 18.42 and 20.34 respectively, and in accordance with [16, 23, 36-39].

The maximum intensity peak which appeared to be dominant on the XRD measurement of the e-spun sample is at $2\theta = 20.34°$ for the (101) and is associated with the $\beta$-phase [39]. This observation suggests that a high percentage of $\beta$-phase that is

considered to be in possession of better electric properties [35] was present in the e-spun PVDF sample, although processed at room temperature. In addition, the relatively small $\alpha$-phase peak at $2\theta = 18.42°$ for the (020) [40] was present in the XRD pattern. The crystalline $\beta$-phase type typically required transformation from TGTG by electrical poling (Seol et *al*. [27]) and mechanical stretching at an elevated temperature. In contrast, the dominant crystalline phase for the pellet and the melt cast samples was the $\alpha$-phase along with the non-dominant $\beta$-phase presence. The associated $\alpha$-phase peaks in the XRD data from the pellet sample were seen at $2\theta = 16.86°$ and $18.86°$ for the (020), and $19.92°$ for the (110) [40]. The XRD data on the melt cast sample also reveals peaks at similar diffraction angles of $18.24°$ for the (020) and $19.76°$ for the (110), in addition to a few more peaks of considerable intensity at $2\theta = 17.54°$ for the (100) and $26.56°$ for the (021) [40].
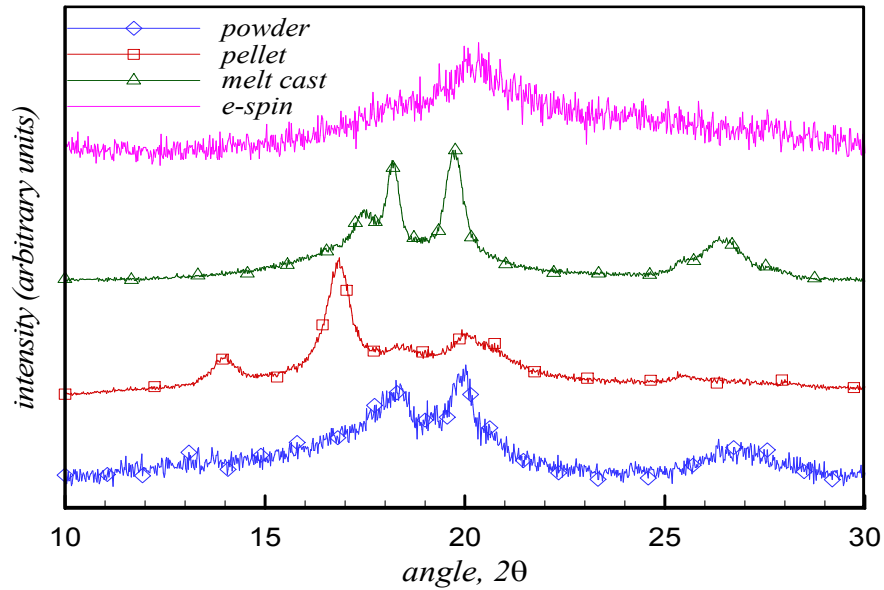


**Figure 3.5:** XRD results for the PVDF samples.

### 3.4.4 Dielectric Behavior Characterization

Complex dielectric expression is written in terms of the dielectric response $\varepsilon'$ and the dielectric loss $\varepsilon''$,

$$\varepsilon^* = \varepsilon' + i\varepsilon'' \tag{3.1}$$

The real part of complex dielectric response $\varepsilon'$ of a material is the normalized permittivity with respect to the permittivity of vacuum. It is a measure of the amount of polarization in a material [41] and calculated from the following equation,

$$\varepsilon' = C_p d /(\varepsilon_0 A) \qquad\qquad (3.2)$$

where $C_p$ is the parallel capacitance, $d$ is the inter electrodes distance, $\varepsilon_0$ is the permittivity of free space, A is the sample electrode area. Moreover, the dielectric loss $\varepsilon''$ was calculated from Eq. (3.3)

$$\varepsilon'' = \varepsilon' \tan\delta \qquad\qquad (3.3)$$

where $\delta = 90 - \varphi$ and $\varphi$ is the phase angle. The tangent loss, $\tan\delta$, is also typically considered as a characteristic dielectric quantity. These dielectric properties of the samples were characterized by the Hewlett-Packard 4194A Impedance Analyzer. Dielectric response was measured between 100 Hz and 1 MHz. The AC dielectric properties were analyzed from the capacitance and the conductivity values in the temperature range of 30 – 150 °C with an accuracy better than 0.1 °C, provided by NOVOTHERM Temperature Control System that was connected to a PT 100 resistor in direct thermal contact with the sample. The parallel capacitance of each samples are measured, and then the dielectric constant of the samples are calculated from Eq. (3.2) for the sample area $A$ and thickness $d$. At each prescribed temperature, the measurements were taken for about thirty frequency levels. The time for one frequency sweep at a fixed temperature was approximately one minute. For each temperature point, the dielectric response and tangent loss as well as time, temperature and frequency were recorded [31, 35, 42, 43]. The applied temperature and frequency ranges in our study are reasonably consistent with the work by S. Abdul Jawad et *al*. [3], where temperatures of 20−100 °C, frequencies of 10 Hz−4 MHz were investigated.

### 3.4.5 Dielectric Response

Given the parameters of Eq. (3.2) *A* and *d* accordingly (see Table 3.2) and assuming that the specimens do not possess any voids, the dielectric constant was computed in reference to the capacitance measurements via impedance analyzer. The summary of the dielectric response measurements on the specimens associated with the three different processes is given in Figure 3.6. It shows that when the temperature increased, so did the dielectric response. The results varied between 2 and 12, between 0.5 and 8 and between 0.4 and 3 for the pellet, melt-cast, and e-spun samples, respectively, in the temperature and frequency ranges studied. Looking into these ranges and the associated frequencies, the dielectric response of the melt-cast and e-spun samples at high frequencies (100 kHz-1 MHz) appeared to be an anomaly being lower than that of vacuum permittivity. This anomaly is attributed to the existence of the voids in the samples. The samples obtained by electrospinning, for instance are normally porous and the geometric parameters of the sample volume in Eq. (3.2) should effectively be different as opposed to no void assumption. Here the effective sample volume is determined by predicting the void content and its effect is mapped to an effective sample area $A_e$. This mapping schematically represented in Figure 3.6 is to smear the distributed voids within the volume into a localized through-the-thickness channel. Specifically, the samples were weighed, $m_e$ and an effective volume is computed by using the density of the PVDF ($\rho$=1.78 g/cm$^3$) $V_e=m_e/\rho$. Then, an effective dielectric constant is proposed in such a way that the effective sample area $A_e$ is used rather than original sample area in Eq. (3.2). That is, the dielectric constant range that has shown anomaly can now be re-calculated by the factor $A/A_e$ as reported in Table 3.2. This approach can only be claimed as a way of defining a limit case to explain the anomaly, rather than a precise correction on the dielectric constant calculations via Eq. (3.2).

|  | Pellet | Melt cast Film | E-spin |
|---|---|---|---|
| *Sample area A* (cm$^2$) | 1.13 | 1.3 | 1.3 |
| **Sample Thickness,** *d* **(cm)** | 0.1 | 0.1 | 0.1 |
| **Mass,** $m_e$ **(g)** | 0,0957 | 0,0776 | 0,0768 |
| **Volume** $V_e = m_e/\rho$ **(cm$^3$)** | 0.0537 | 0.0436 | 0.0431 |
| *Effective $A_e =$* $V_e/d$ **(cm$^2$)** | 0.537 | 0.436 | 0.431 |
| $A/A_e$ | 2.1 | 2.98 | 3.01 |

**Table 3.2:** The calculations for correction factors due to the existence of voids

The re-calculated values value of the dielectric response varied between 6 and 18, between 3 and 16 and between 2 and 8 for the pellet, melt-cast, and e-spun samples, respectively, in the temperature and frequency ranges studied as seen in Figure 3.6.
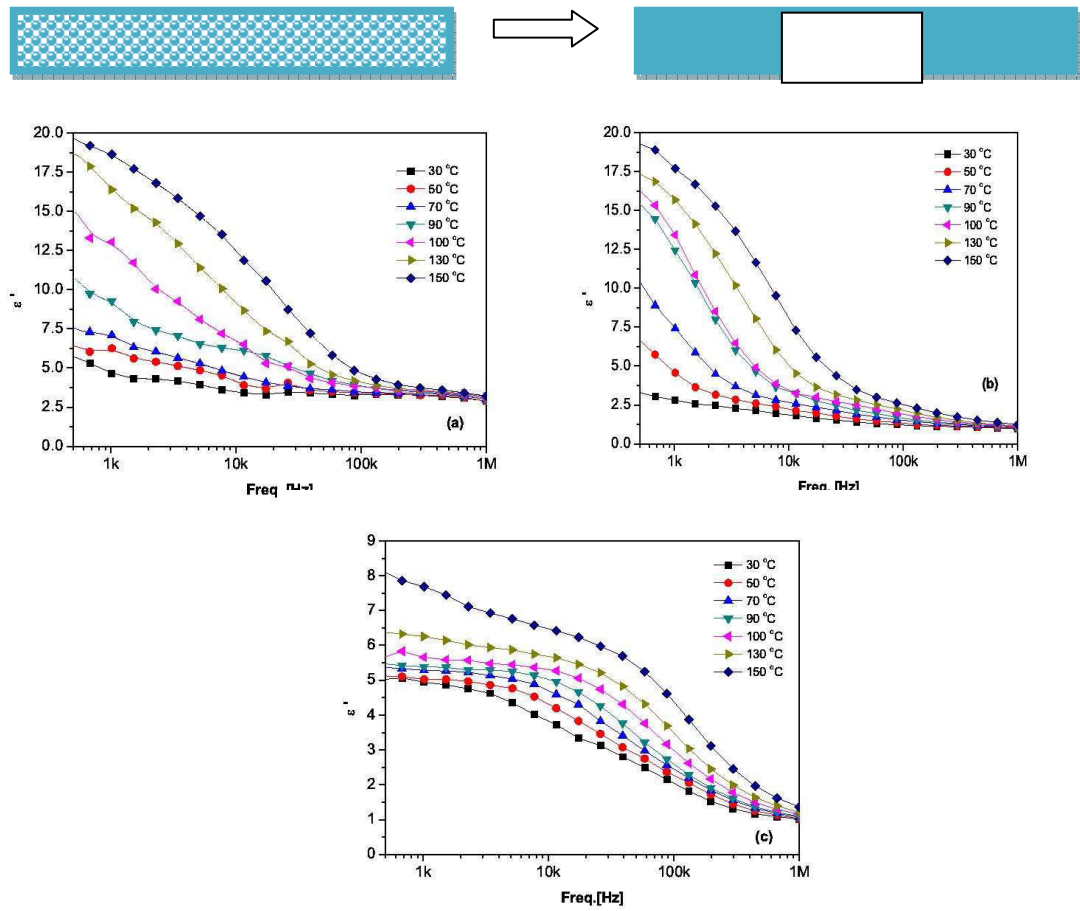
**Figure 3.6:** Temperature-frequency scan for dielectric response calculated via Eq. 3.2 based on presumably smeared voids creating the effective sample area $A_e$ and thickness $d$: a) pellet, b) melt cast and c) e-spun samples.

The dielectric constant measurements on the specimens associated with the three different processes are now summarized also in Figure 3.6. It shows that the dielectric response increases with the increase in temperature. Overall, descending order of the dielectric response is observed as the cold press pellet, melt cast, and e-spun samples. The measurements along with the DSC analyses suggest that there is a negative correlation between the total crystallinity and the dielectric response. That is, lower the crystallinity, higher the dielectric response. Regarding the effect of total crystallinity in polymeric materials, this is expected as the higher mobility of the chains in the polymer (the lower the degree of crystallinity) results in the higher dielectric response [44, 45]. It is also known that dielectric response depends on the available polarization possessed by the material. Considering the existence of process driven polar and non-polar

crystalline phases in PVDF, the next factor to look at is their effect on the dielectric response. The XRD data in Figure 3.5 suggest that signature of the polar $\beta$ - phase was particularly observed in the e-spun sample as anticipated. The polarity is expected to increase the dielectric response of e-spun sample. Test results, however show that dielectric response of the e-spun sample was generally the lowest, compared to the cold pellet in particular. This dielectric response difference was attributed to the dominance of the total crystallinity effect as opposed to the phase affect. The e-spun sample was recorded to have the highest total crystallinity with lower dielectric response than the cold pellet and melt cast samples.

The effect of the polar phase is more pronounced when we compare the melt cast and e-spun samples that have relatively similar total crystallinity. Figure 3.6 shows the comparison of the frequency dependence of the dielectric behavior at several temperatures (30 °C, 60 °C, 150 °C). At around the room temperature, the dielectric response of the e-spun sample was higher than the melt cast sample although the total crystallinity of the melt cast sample was lower. It is concluded that notable existence of the $\beta$ - phase in e-spun sample provided the overriding polarization mechanism as the difference between total crystallinities was about 3%. However at elevated temperatures, the dominance of the polar phases appeared to diminish as opposed to total crystallinity. This dielectric response decrease is attributed to the fact that as the temperature increases, the effect of the mobility of the chains is also higher for the lower percentage crystalline structure.
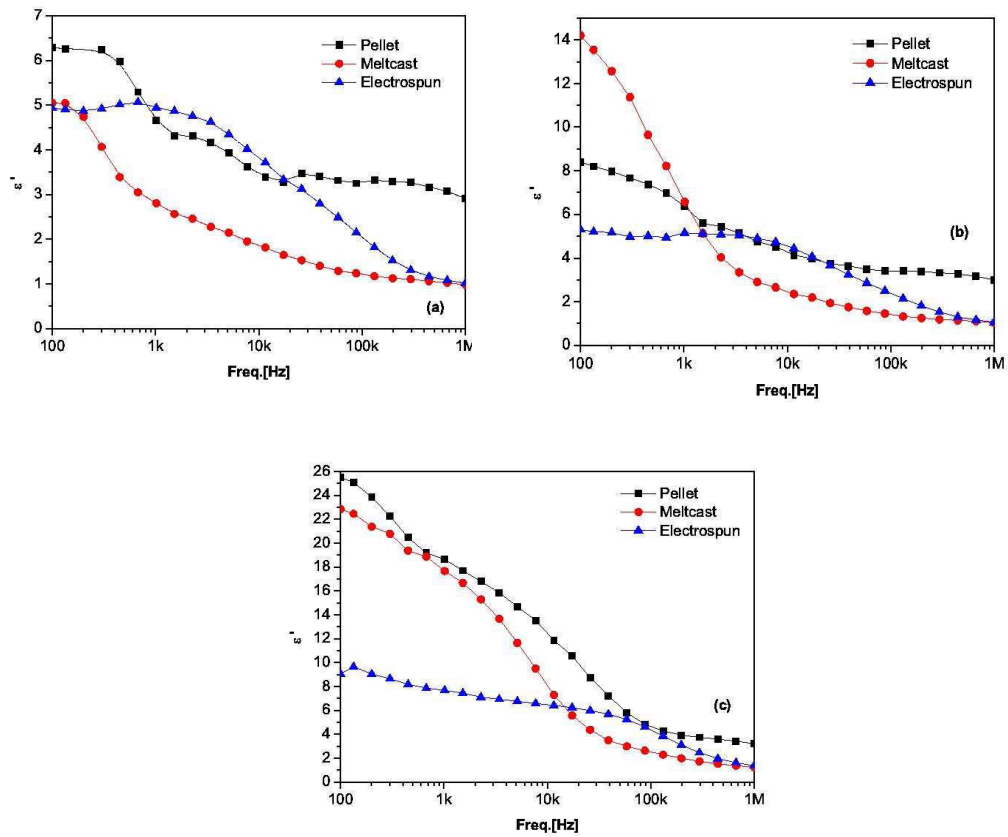
**Figure 3.7:** Comparison of the frequency scan for dielectric response on the pellet, melt cast, and e-spun samples at a) 30 °C b) 60 °C and c) 150 °C.

Figure 3.7 shows the sensitivity of the dielectric response to the temperature. At 1 kHz, for instance, the recorded range of dielectric response was about 4-to-25 for the cold pellet sample. It was 2-to-23 for the melt cast sample. The least sensitive measurements appeared to be on the e-spun sample. At much higher frequencies (beyond 100 kHz), however, temperature dependence on the pellet and melt cast samples diminished whereas the temperature sensitivity of the dielectric response of the e-spun sample was somewhat more stable within the whole frequency range. These observations suggest that the polar $\beta$ - phase with permanent dipoles is less prone to effect of temperature-frequency interaction. The dielectric behavior presented here is consistent with the results in Su-Hong Park et *al.* [3] and S. Abdul Jawad et *al.* [46].

## 3.4.6 Dielectric Loss
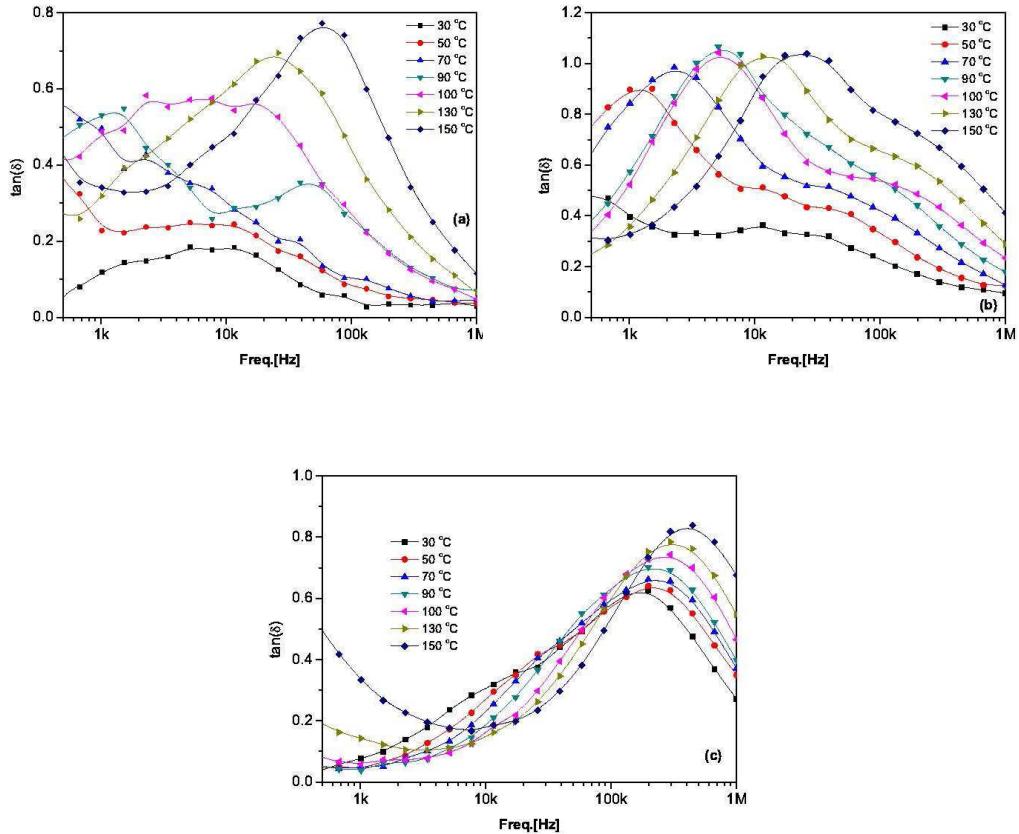


**Figure 3.8:** Temperature-frequency scan for loss tangent: a) pellet, b) melt cast and c) e-spun.

Loss tangent data of the three samples was also recorded and shown in Figure 3.8. Despite the differences between the dielectric response scale of the pellet, melt cast and e-spun samples, the loss tangent for the three samples remained in the same scale. The qualitative behavior however, differed.

Below 100 °C, there are more than one resonance peak for the pellet sample. This can be attributed to structural rearrangement of the chains of the polymer. Within the PVDF, the $\alpha$-relaxation process connects with segment motion [47]. This means that the $\alpha$-process is related to the molecular motion in the crystalline region. Above 100 °C, the crystalline phases become less influential in resonance response and only one resonance peak appears to remain at near 100 kHz which corresponds to the resonant

loss of the $CF_2$–$CH_2$ dipoles within pellet. This is also evident in the decrease of $\varepsilon^{'}$, as the rotational dipole motion cannot keep up at high frequency ($>10^4$ Hz) as seen in Figure 3.6$a$.

The relaxation processes in the melt cast film also lead to additional peaks usually located in kHz–MHz region. The two observed peaks (Figure 3b) are attributed to the multiple relaxation peaks for different dominantly no-polar phases, in the material [48]. The relaxation peak on the e-spun sample, on the other hand, was measured at relatively higher frequencies compared to the pellet and the melt-cast sample response. This increase in the resonance frequency is attributed to the more dominant existence of the polar $\beta$ –phase.

Moreover, a shift in the polarization relaxation frequency associated with the peak of dielectric loss was observed, as also stated by Park et $al$. [43]. It is evident that dielectric loss tends to increase at elevated temperatures (Figure 3.8 b and c) [31]. The dependence of the loss tangent of the pellet sample to the temperature and frequency is somewhat unstable, whereas the dissipation factor for the melt cast and e-spun samples exhibited notable trends. The change in the peak values for the dielectric loss was not significant for the melt cast sample as the temperature varied, but a shift was observed. On the other hand, both the peak value and its associated frequency measured on the e-spun sample increased with the elevated temperature. Frequency scans for dielectric loss $\varepsilon^{\prime\prime}$ at 30 °C, 60 °C, and 130 °C for the melt cast and the e-spun samples are shown in Figure 3.9, accompanied by Figure 3.8, in order to evaluate the relation between dielectric loss $\varepsilon^{\prime\prime}$ and the temperature. As seen in Figure 3.8, the tangent loss or dissipation factor (DF) increases with elevated temperature, as the energy loss increases. Generally, the dielectric relaxation frequency of the e-spun sample is higher than the melt cast sample. In Table 3.3, dielectric relaxation frequency data is also reported.

## 3.4.7 The Cole-Cole Plots

It is known that PVDF based ferroelectric polymers exhibit rich relaxation processes due to their semi-crystalline nature that is the molecular relaxations in amorphous and crystalline domains, as well as at the crystal-amorphous interface [49]. The relaxation parameters that are found by the dielectric spectroscopy technique offer information regarding the microstructural characteristics of the materials, such as the molecular mobility/ability to move within the material. Moreover, a semi-circular Cole-Cole plot based on dielectric measurements [50] shows that the material has resistance-capacitance (RC) type circuit characteristics. Thus, the Cole- Cole plots are significantly valuable to figure out the movement mechanism of molecules in materials under the applied electric field.

The complex dielectric dispersion curves are described by the Cole–Cole relation that is represented by the following Eq. (3.4) [50, 51].

$$\varepsilon^*(\omega) = \varepsilon_\infty + \frac{\varepsilon_0 - \varepsilon_\infty}{1 + (i\omega\tau)^{1-\alpha}} \tag{3.4}$$

where $\varepsilon^*(\omega)$ is the complex dielectric response. $\varepsilon_0$ and $\varepsilon_\infty$ are the low-frequency and high frequency dielectric response, respectively, $\tau$ is the average relaxation time, $\omega$ is the average angular frequency, and $\alpha$ is the Cole-Cole plot distribution parameter. The relaxation curve for $\alpha = 1$ corresponds to the Debye-type relaxation and a smaller $\alpha$ value gives a broader symmetric relaxation curve [52].

We have calculated the relaxation time $\tau$ from the Debye-type equation that is represented via Eq. (3.4) [53] by fitting the data shown in Figure 3.9. The average relaxation time $\tau$ values are given in Table 3.2. The values of $\alpha$ were also determined from the Figure 3.9 plots by fitting Eq. (3.4) to these Cole-Cole Plots and reported in Table 3.2.
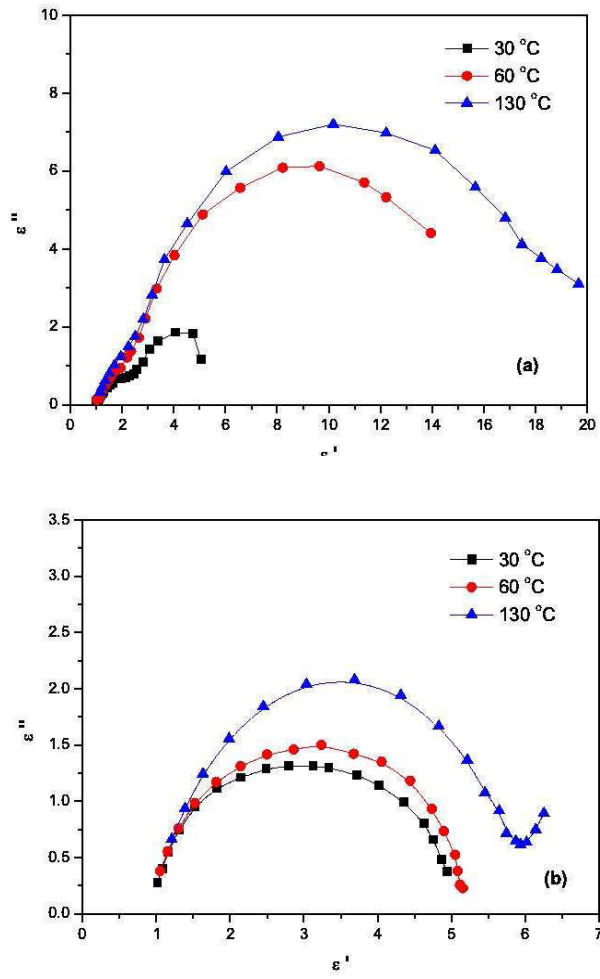
**Figure 3.9:** Cole-Cole plot of (a) melt cast at 30 °C, 60 °C, and 130 °C (b) e-spun at 30 °C, 60 °C, and 130 °C.

| Samples | T [°C] | Adj. R-Square | $\alpha$ | $\tau$ | $\varepsilon'_\infty$ | $\varepsilon'_\infty$ | $\varepsilon''_{max}$ | $f_c$ |
|---|---|---|---|---|---|---|---|---|
| Meltcast | 30 | 0.9745 | 0.45001 | $2.693 \times 10^{-4}$ | 5.05 | 1.03 | 1.81 | 303.13 |
| | 60 | 0.9916 | 0.25646 | $2.129 \times 10^{-4}$ | 14.19 | 1.04 | 6.08 | 530.95 |
| | 130 | 0.9983 | 0.26228 | $0.502 \times 10^{-4}$ | 19.71 | 1.08 | 7.16 | 3362.20 |
| E-Spin | 30 | 0.9920 | 0.27371 | $0.0518 \times 10^{-4}$ | 4.92 | 1.01 | 1.32 | 33462.63 |
| | 60 | 0.9969 | 0.24096 | $0.0366 \times 10^{-4}$ | 5.26 | 1.07 | 1.49 | 38891.11 |
| | 130 | 0.9944 | 0.19509 | $0.0201 \times 10^{-4}$ | 6.25 | 1.2 | 2.05 | 99328.25 |

**Table 3.3:** Cole-Cole plot characteristics from the dielectric: adjusted coefficient of determination $R_a^2$, distribution parameter $\alpha$, relaxation time $\tau$, dielectric relaxation frequency $f_c$, low frequency dielectric response $\varepsilon'_0$, high frequency dielectric response $\varepsilon'_\infty$, max. dielectric response $\varepsilon''_{max}$ values of melt cast and e-spin samples.

Table 3.3 reveals that both the distribution parameter $\alpha$ and average relaxation time $\tau$ decreased as the temperature increased. The meaning of decreasing $\tau$ is that samples can rapidly go along with the applied electric field, at elevated temperatures. Moreover, the $\alpha$ values suggest a high-frequency relaxation process with non-Debye-type behavior. It is believed that this behavior is due to the dipolar rotation around the long molecular axis of polymer [53]. The $\alpha$ values at elevated temperature reported in Table 3.2, indicate the dipolar rotation in the melt cast sample decreased whereas dipolar rotation in the e-spun sample did not change so much. That is the dielectric behavior of the e-spun sample, owing to higher crystallinity, was more stable than was the melt cast sample, as could be seen in the frequency scan-dielectric response graphs in Figure 3.7. The polymer chains within melt cast have more freedom of movement than they do in e-spun. Therefore, the dipoles in e-spun samples do not change their places more easily that in melt cast sample due to higher crystallinity of e-spun structure.

The radius of a circular Cole-Cole curve corresponds to the relaxation coefficient of the sample [42]. In addition, the existence of multiple relaxation modes results in an elliptical curve compared to single mode circular Cole-Cole plot. The dielectric response associated with the maximum loss is denoted as $\varepsilon''_{max}$ and its values are

determined from these plots as well at various temperatures (30 °C, 60 °C, 130 °C) as reported in Table 3.3.

## 3.5 CONCLUSION

Three different samples that were prepared as cold press pellet, melt cast film and e-spun fibrous mat were tested for figuring out the crystallinity effect upon their dielectric properties. As seen from DSC results, the crystallinity correlated negatively with the dielectric response. Specifically, the dielectric response descends while the crystallinity ascends in the following order; e-spun fibrous mat, melt cast film and cold press pellet.

X-ray diffraction was then utilized to observe the distinct crystalline phases and to discuss on their dominance. In particular, the refraction angle ($2\theta$) peaks associated with the $\alpha$ - phase and $\beta$ - phase were noted in XRD graphs. It is found that the distinct crystalline phase peaks of PVDF depend on the conditions of crystallization: crystalline transformations when crystallized from melt or from amorphous polymer. Additionally, comparison of the heat of fusion by DSC suggested that the electrospinning method increases the crystallinity percentage. The Cole-Cole Plots' formation and associated distribution parameters $\alpha$ suggests that a high-frequency relaxation process of PVDF samples is in effect with non- Debye-type behavior. This behavior is attributed to the dipolar rotation around the long molecular axis of PVDF. The distribution parameter; $\alpha$ values that are measured for the melt cast sample decreases at elevated temperature, however these $\alpha$ values are higher than for the e-spun sample. The dipolar rotation and the dielectric behavior shows that more stable behavior against the temperature on the e-spun sample occurs due to its crystallinity's being higher.

## 3.6 REFERENCES

1. Rankin, C.; Chou, C.-H.; Conklin, D.; Bonnell, D. A. ACS Nano 2007, 1, 3.

2. Geschke, D.; Leister, N.; Steffen, M.; Glasel, H. J.; Hartmann, E. J Mater Sci Lett 1997, 16, 1943.

3. Park, S.-H.; Lee, D.-C. Journal of the Korean Physical Society 1999, 35, 5, 431-437.

4. Bergman, J. G.; McFee, J. H.; Crane, G. R. Appl Phys Lett 1971, 18, 203.

5. Ryu, J.; Park, J.; Kim, B.; Park, J.-O. Biosensors and Bioelectronics 2005, 21, 822–826.

6. Jiang, Y.; Ye, Y. ; Yu, J.; Wu, Z.; Li, W.; Xu, J.; Xie, G. Polym. Eng. Sci 2007, 47, 1344–1350.

7. Dargaville, T. R.; Celina, M. C.; Elliott, J. M.; Chaplya, P. M.; Jones, G. D.; Mowery, D. M.; Assink, R. A.; Clough, R. L.; Martin, J. W.  Sandia National Laboratories

8. Kawai, H. Jpn. Appl. Phys 1969, 8, 975.

9. Zheng, J. P. Proceedings of The 6th International Conference on Properties and Applications of Dielectric Materials 2000, 18, 143 (1), 9891.

10. Murayama N.; Hashizume, H. J. Polym Sci 1976, 14, 989.

11. Pfister, G.; Abkowitz, M.; Crystal, R.G. J. Appl. Phys 1973, 44, 2064.

12.  Blob, P.; Steffen, M.; Schafer, H.; Eberle, G.; Eisenmenger, W. IEEE Tran. Dielect. And Electr. Insul 1996, 3, 417.

13. Osaki, S. J. Polym. Sci. B 1995, 33, 685.

14. Jow, T.R.; Cygan, P.J.; J. Appl. Phys 1993, 73, 5147.

15. Murayama, N. J. Polym. Sci 1975, 13, 929.

16. Mago, G.; Kalyon, D. M.; Fisher, F. T.  Journal of Nanomaterials 2008, 8.

17. Cebet, P.; Grubb, D.T.  Macromolecules 1984, 17, 7. Cebet, P.; Grubb, D.T. Macromolecules 1984, 17, 7.

18. Ozkazanc, E.; Guney, H. Y.; Oskay, T.; Tarcan, E. Journal of Applied Polymer Science, 2008,109, 3878–3886.

19. Elashmawi, I.S.; Hakeem, N.A. Journal of Applied Polymer Science 2006, 102, 2125–2131.

20. Mhalgi, M. V.; Khakhar, D. V.; Misra, A. Polym. Eng. Sci 2007, 47, 1992–2004.

21. Pallathadka, P. K.; Tay, S.S. Polym. Eng. Sci 2006, 46, 1684–1690.

22. Andrew, J. S.; Clarke, D. R. Langmuir 2008, 24, 670-672.

23. Harrison, J. S., Ouniaes Z. Piezoelectric Polymers. NASA Langley Research Center, 2001, 43, NASA/CR-2001-211422.

24. Furukawa, T. Key Eng. Mater 1994, 15.

25. Hilczer, B.; Kueka, J.; Markiewicza, E.; Kosecb, M.; Mali, B. Journal of Non-Crystalline Solids 2002, 305, 167-173.

26. http://repositorium.sdum.uminho.pt/bitstream/1822/5170/1/872-876.pdf last accessed on January 1, 2008.

27. Seol, W.-H.; Lee, Y. M.; Park, J.-K. Journal of Power Sources 2007, 170, 191–195.

28. Chung, M.Y.; Lee, D.C. Journal of the Korean Physical Society, 2001, 38, 2, 117-122.

29. Kułek, J.; Hilczer, B. Ferroelectrics, 1996, 184, 131.

30. Yordem, O. S.; Papila, M.; Menceloglu, Y. Z. Materials & Design 2008, 26 (1), 33 – 44.

31. Dagdeviren, C.; Papila, M. Polymer Composites, accepted, April, 2009.

32. Benz, M.; Euler, W.B. Journal of Applied Polymer Science 2002, 89, 1093.

33. Zhao, Z.; Li, J.; Yuan, X.; Li, X.; Zhang, Y.; Sheng, J. Journal of Applied Polymer Science 2005, 97, 466–474.

34. Quadah, A. M.; Al-Raheil, I. A. Polym. Intern 1995, 38, 381.

35. San, S.E.; Yerli, Y.; Okutan, M.; Yılmaz, F.; Gunaydin, O.; Hames, Y.; Materials Science and Engineering B 2007, 138, 284–288.

36. Gregorio, R.; Cestari M.; Journal of Polymer Science Part B-Polymer Physics 1994, 32(5), 859-870.

37. Esterly, D.; Love, B. Journal of Polymer Science; Part B Polymer Physics 2004, 42, 91-97.

38. Kim, J.-W.; Cho, W.-J.; Ha, C.-S. Journal of Polymer Science: Part B: Polymer Physics, 2002, 40, 19–30.

39. Ma, W.; Zhang J., Wang X., J Mater Sci 2008, 43, 398–401.

40. Newman, B. A.; Yoon, C.H.; Pae, K.D.; J. Appl. Phys 1979, 50, 6095.

41. Knight, R.J.; Nur, A. Society of Exploration Geophysicists, 1986.

42. Okutan, M.; Yakuphanoglu, F.; San, S.E.; Koysal, O.; PhysicaB 2005, 368, 308–317.

43. Park, S.-H.; Lim, E.-C.; Park, K.-S.; Kang, D.-H.; Han, S.-O.; Lee, D.-C. Proceedings of the 5th Internationd Conference on Properties and Applications of Dielectric Materials May 25-30, 1997, Seoul, Korea.

44. Harrop, P. J. Dielectrics 1972 (Butterworths).

45. Nussbaum, A. Electronic and Magnetic Behaviour of Materials 1967 (Prentice-Hall) 70-77.

46. Jawad, S.A.; Jundi, J.A.; El-Ghanem, H.M.; Sagan, S. International Journal of Polymeric Materials 2004, 53:365–373.

47. Mahantappa, S. J.; Krishnamurthy, B. S.; Kothiyal, G. P.; Saraswati, V. Current Science, 2002, 83, 4.

48. Naguyen, V. Q.; Sanghera, J. S.; Lioyd, I. K.; Aggarwal, I. D.; Gershon, D. J. Non-Cryst. Solids, 2000, 276, 151–158.

49. Andrew, J.S.; Clarke, D.R. Langmuir 2008, 24, 670-672.

50. Cole K S and Cole R H 1941 J. Chem. Phys. 9 341–51.

51. http://www.doitpoms.ac.uk/tlplib/dielectrics/structure.php last accessed on February 1, 2008.

52. Ma, W.; Zhang J., Wang X., J Mater Sci 2008, 43, 398–401.

53. http://arxiv.org/ftp/arxiv/papers/0808/0808.0419.pdf last accessed on March 1, 2008.

**CHAPTER 4**


**4 PAPER-2**



**Dielectric Behavior Characterization of a Fibrous-ZnO/PVDF Nanocomposite**

Paper-2 was accepted by the Journal of Polymer Composite.

Road map of the paper-2 is given above.

EXPERIMENTAL

Electrospinning of precursor fibers

PVA + distilled water (5:20 w/w)
Stir for 4 hours

ZnAc + distilled water (6:20 w/w)
Stir for 4 hours

Stir for 5 hours at 60 $^{o}$C
Cooled to room T then electrospun

Diameter of nozzle: 300 $\mu m$
New Era NE-1000 Syringe Pump with Pumpterm Software
Voltage: 10 kV, Distance: 8 cm

Calcination & Sintering

Dwell steps:
100 $^{o}$C, 300 $^{o}$C, 400 $^{o}$C, 500 $^{o}$C, 600 $^{o}$C
~12 hours

At 1200 $^{o}$C
~9 days to obtain ZnO fiber mat

Fibrous ZnO/PVDF matrix composite formation

For solution cast PVDF: PVDF + DMF →10% w/w at room T → solution
cast on a glass substrate at 60 $^{o}$C for 4 hours.

ZnO mat was sandwiched between two PVDF solution cast film and
melt at 180 $^{o}$C. Upon cooling, the composite is formed.

CHARATERIZATION

SEM & EDXS

Crystalline Phases by XRD

Raman spectroscopy for
composite and ZnOH

Dielectric Analysis
Temperature: 30-150 $^{o}$C
Frequency: 100 Hz-1 MHz

# Dielectric Behavior Characterization of a Fibrous-ZnO/PVDF Nanocomposite

Canan Dagdeviren and Melih Papila

*Sabancı University, Faculty of Engineering and Natural Sciences, Material Science and Engineering, Tuzla, Istanbul, 34956 (Turkey)*

## 4.1 ABSTRACT

This study is focused on forming a fibrous-ZnO/PVDF nanocomposite and characterizing its dielectric behavior. The nanocomposite is prepared in two steps. First, a network of nanoscale diameter zinc oxide (ZnO) fibers is produced by sintering electrospun PVA/Zinc Acetate fibers. Second, the ZnO fibrous non-woven mat is sandwiched between two polyvinylidine fluoride (PVDF) thermoplastic polymer films by hot-press casting. Scanning electron microscope (SEM) images of the nanocomposite show that hot-press casting of the fibrous-ZnO network breaks the network up into short fibers. The in-plane distribution of the ZnO fillers (i.e., the short fibers) in the PVDF matrix appears to comply with that of the pristine ZnO fibers prior to hot-pressing, indicating that the fillers remain well-dispersed in the polymer matrix. To the authors' knowledge, the work reported herein is the first demonstration of the use of electrospinning to secure the dispersion and distribution of a network of inorganic fillers. Moreover, processing a fibrous-ZnO/PVDF flexible composite as described in this report would facilitate material handling and enable dielectric property measurement, in contrast to that on a fibrous mat of pure ZnO. Due to the high surface area of the short ZnO fibers and their polycrystalline structure, interfacial polarization is pronounced in the nanocomposite film. The dielectric response is enhanced significantly—up to a factor of ten at low frequencies compared to the dielectric response of constituent materials (both bulk ZnO and PVDF), and up to a factor of two compared to a bulk-ZnO/PVDF composite.

**Key words:** Nanocomposite, electrospinning, ZnO nanofiber, dielectric characterization.

**4.2 INTRODUCTION**

Zinc oxide (ZnO) is a technologically attractive material due to its potential for sensor applications [1, 2] enabled by catalysis [3], optical emission [4, 5], piezoelectric transduction and actuation [6-8]. The wide array of nanostructures producible broadens the appeal for their incorporation into functional composites. Individual ZnO nanobelts, for instance, were produced and measurements by piezoresponse force microscopy revealed promising results for the future of ZnO in nano-sensors and nano–actuators industry [9]. Specifically, the effective piezoelectric coefficient was reported to impart an increase, attributed to the nano-scale structure, by more than a factor of two.

For producing ZnO nanostructures, a variety of physical or chemical techniques have been used from the vapor or the liquid phase [1, 10-12]. One promising alternative is the use of electrospinning combined with heat treatment to generate a nanofiber network film [13-18]. This versatile technique has been broadly applied for solution processing of fibers from polymeric materials, as well as bioactive glass and ZnO, to name a few. For example, thermal processing electrospun polyacronitrile (PAN) produced a high-purity carbon nanofiber web that was proposed as a potential anode for high-power lithium-ion batteries [13]. The control of morphology and fiber orientation in the electrospinning of the polymer precursor fiber has been addressed in numerous studies. Methods have been proposed and proven for controlling the fiber alignment: for instance the work by Dzenis [19]. However, thermal treatment parameters, such as calcination time, on the as-spun pre-cursor fiber pattern and fiber diameter are still under investigation [18]. More recently, Kim et *al.* reported their results concerning the morphological variation due to several effects, and concluded that calcination conditions were the most significant factor [20].

The associated increase in surface area of nanoscale fillers offers advantageous electrical properties in polymeric composites, when compared to their bulk form and to traditional micron-size fillers [9, 21-23]. Polymer composites of high dielectric response, for instance, are desirable for a variety of high dielectric response electronic devices, such as transducers, piezo-sensors, hydrophones [24] and in producing

electromagnetic antennas. Malmonge et *al*. [25] produced flexible composites of poly(3- hydroxybutyrate) (PHB) and lead zirconium titanate (PZT) for ferroelectric and dielectric applications. They produced composites of different compositions and demonstrated the effect of PZT volume percentage. At a threshold ceramic content, the dielectric response can increase the dielectric response of PHB by as much as five times. It has also been noted that the composite properties depend on the size, geometry, and surface quality of the filler materials and could be tailored, if the dispersion of the fillers could be controlled [21, 26]. Hong et *al*. [21] studied the dielectric response of a ZnO/LDPE composite and the effects due to the particle size and spatial distribution of the ZnO filler. Just recently, the effects of percolation and filler distribution morphology on the dielectric properties were reported by Wang et *al.* for radial-ZnO/PVDF composites. Their results demonstrated that a significant increase in the dielectric response was achieved by the addition of R-ZnO fillers into the polymer matrix, provided that the filler volume fraction remained below the percolation threshold.

The work being presented here introduces the concept of using electrospinning to form an inorganic filler network to secure the dispersion and distribution of the fillers in the polymer matrix. Specifically, we report on the feasibility of fibrous ZnO fillers by electrospinning and their insertion into PVDF polymer matrix to form the nanocomposite. The process for producing the fibrous-ZnO/PVDF nanocomposite is described in the next section, followed by the dielectric characterization of the nanocomposite under various frequency and temperature along with the crystalline structure. Supporting evidence for the results and associated discussions are provided by the x-ray diffractometry (XRD), SEM, and Raman spectroscopy.

## 4.3 EXPERIMENTAL

The processing in the present work consists of two major stages:
1) the electrospinning of the polymer solution to form precursor fibers containing zinc;
2) thermal treatment of these fibers, i.e. calcination/sintering to form a fibrous ceramic structure.

The process parameters, including solution concentrations, calcination temperature, and exposure time were investigated independently, in order to achieve a continuous ZnO fibrous network.

## 4.3.1 Electrospinning of precursor fibers

In a homemade electrospinning set-up, as depicted in Figure 4.1, a polymer solution inserted into a syringe that has a 300 μm diameter nozzle, was subjected to a DC bias ranging between 5 to 15kV. The rate of the polymer flow from the syringe was determined by a computer controlled syringe pump (New Era NE-1000 Syringe Pump along with Pumpterm Software). Under the applied electric field, the polymer solution was extracted from the nozzle onto the collector due to high electrostatic force acting on the polymer droplet at the tip of the nozzle [27]. As the polymer jet traveled through air, a fiber was formed, and its diameter was reduced significantly by the solvent evaporation. The randomly oriented, fine fibers collected on the screen positioned above the collector plate produced a fiber mat, of a nano to micron-scale determined by the process parameters.
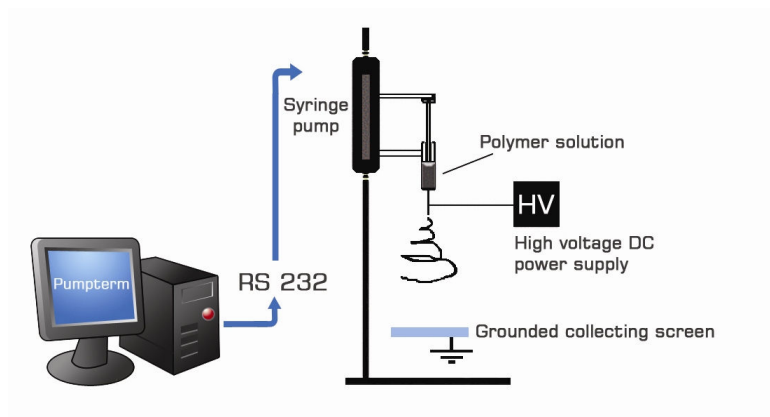


**Figure 4.1:** Schematic representation of the computer controlled electrospinning setup.

Electrospun PVA fibers with a surface decorated by zinc acetate (ZnAc) particles were produced by electrospinning a PVA-ZnAc precursor solution [28, 29]. The precursor solution was prepared with PVA-distilled water (5:20 weight/weight) and ZnAcetate-distilled water (6:20 weight/weight) solutions separately. These two

solutions were homogenized by stirring for four hours. The viscous PVA solution was then poured into the ZnAc solution, which was then heated to 60 ºC and stirred for five hours, to ensure a homogeneous distribution of the Zn and acetate ions. The solution was cooled to room temperature and then electrospun [3]. The electrospinning process was optimized for two process variables: voltage and distance between the syringe tip and the collector target. The best result for the production of a continuous and fine precursor fiber was obtained when the applied voltage and the collector distance were 10 kV and 8 cm, respectively. The resultant electrospun mat exhibited a fibrous structure of PVA (with an average fiber diameter of 700 nm) onto which ZnAc particles were distributed.

## 4.3.2 Calcination and Sintering

In order to produce ZnO fibers, the next step was the thermal treatment of the precursor fiber mat, in order to eliminate the organics for producing ZnO (i.e. calcination) and sintering of the ZnO grains. The necessary thermal treatment schedule was determined via DTA/TGA simultaneous analysis. As seen from Figure 4.2, the elimination of organic substances at 250 ºC, 360 ºC and 450 ºC [5] suggested that the organic burn-out was completed below 500 ºC.
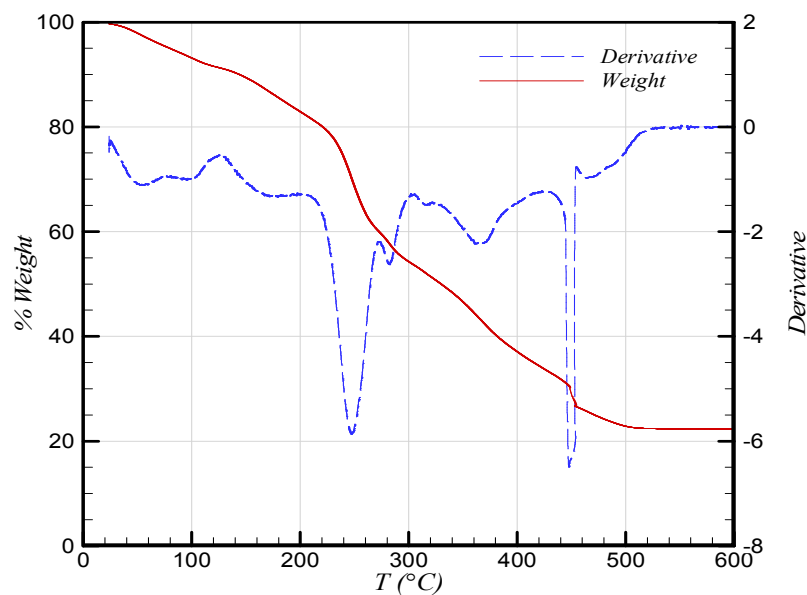


**Figure 4.2:** TGA results showed that the inorganic part is attained after 450 ºC.

Since the weight loss was about 73% after calcinations and Zn has a higher density than other atoms in the structure, the volume of the heat treated mat was significantly reduced. Therefore, the slow removal of the organics from the organic fiber mat was imperative. For this purpose, a stepwise heating schedule was applied with several ramp and dwell steps. With a heating ramp rate of 0.5 ℃/min, the dwell steps for calcination were held at 120 ℃, 300 ℃, 400 ℃, 500 ℃ and 600 ℃, each lasting ~12 hours in duration. Sintering was carried out at 1200 ℃ for an additional hundred hours. In total, ~9 days to obtain the ZnO fiber mat. This prolonged treatment allowed the successful removal of the organics and the formation of inorganic fibers formed from ZnO particles. The significant amount of shrinkage of the sample also implied that there would be friction between the surface of the platinum substrate and the sample during the heat treatment. Therefore, the organic mat was suspended over an intentionally wrinkled surface of the Pt-tray, in order to minimize the contact between the fibrous mat and the substrate.

### 4.3.3 Fibrous ZnO/PVDF matrix composite formation

In order to manipulate the extremely fragile ZnO fiber mats and perform dielectric characterization, the electrospun fibrous mat was carefully placed between two solution-cast polyvinylidine fluoride (PVDF) films and pressed at a temperature above the melting point of PVDF. The PVDF (Alfa Aesar) solution in dimethylformamide (DMF) was first prepared 10% w/w at room temperature. The solution was then cast on a glass substrate kept in an oven, at 60 °C for 4 hours. Finally, to maintain the planar network of the ZnO fibers, the ZnO mat was sandwiched between the two PVDF solution-cast films and pressed to melt at 180 °C. Upon cooling, a ZnO/PVDF flexible composite film was produced.

## 4.4 RESULTS and DISCUSSION

### 4.4.1 Content, Crystalline structure and Morphology

The first crucial assessment was to ascertain that the ZnO had remained intact in the resultant fibrous mat. The content of the mat was analyzed by energy-dispersive x-ray spectroscopy (EDXS) under a 15 kV and 6 mm working distance. EDXS results showed the signatures of Zn and O at weight fractions of 55% and 45%, respectively, and confirmed that the mat was made of fibrous ZnO. Next, the crystalline structure of the ZnO fiber mats was determined by XRD (Bruker AXS D8) measurements. The reflection angles coming from the specific crystal planes shown in Figure 4.3 were consistent with that of the wurtzite form of zinc oxide [22].
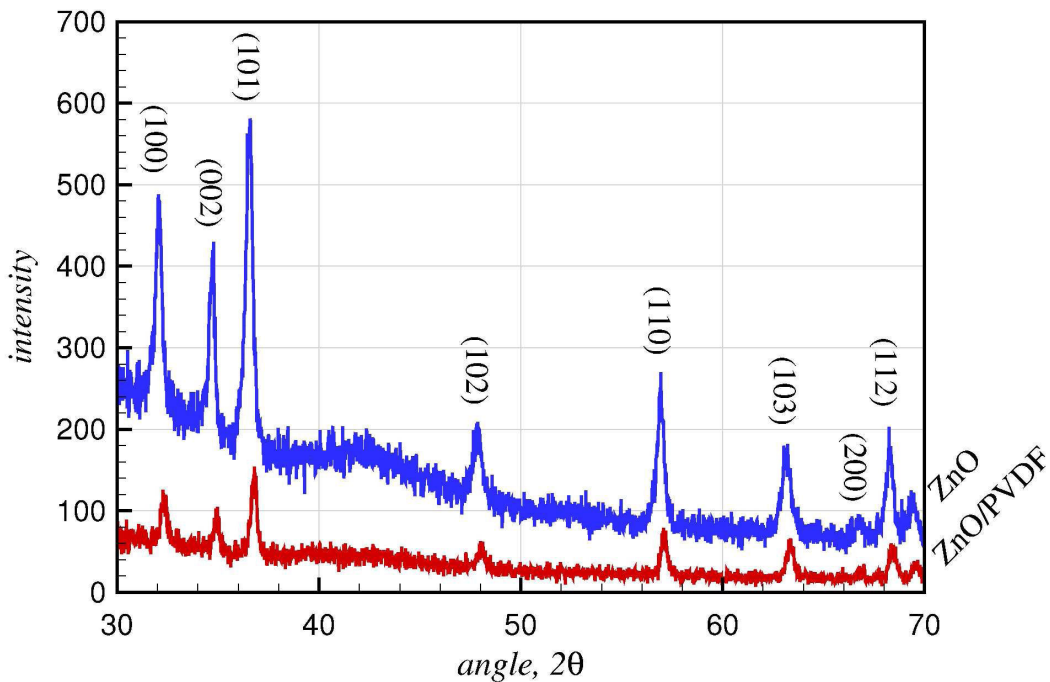


**Figure 4.3:** In XRD spectra obtained from the ZnO fiber mat and fibrous-ZnO/PVDF composite samples, the peaks matched those of the wurtzite form of ZnO [24, 32, 33].

This crystal structure is particularly important, since the electro-active characteristics of ZnO stem from the inherent symmetry [30-32]. The fibers and the mat heat-treated at 600 °C were both extremely difficult to handle; whereas fibers sintered at 1200 °C resulted in their somewhat improved handling and strength. A denser and well

sintered morphology of the polycrystalline fibers and mats (Figure 4.4) were observed at 1200 ºC.
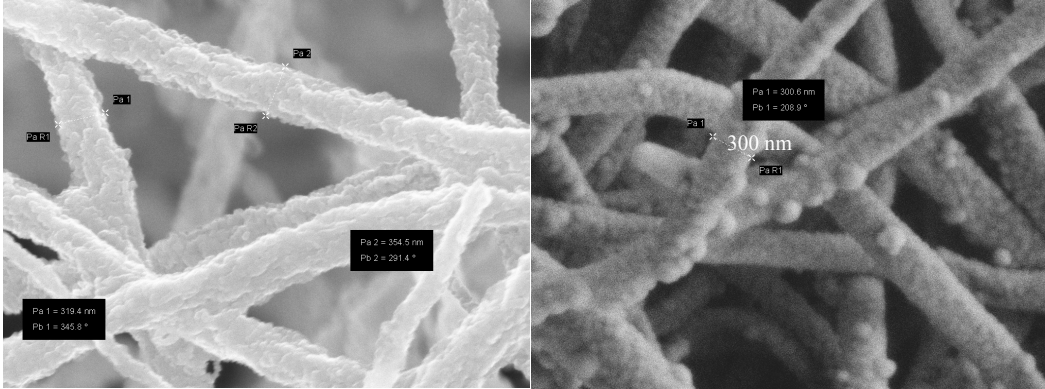


**Figure 4.4:** SEM images of the ZnO fibers treated at a) 600 ºC, and b) 1200 ºC.

The fibrous-ZnO/PVDF composite was also characterized by XRD and SEM. The XRD spectra of the fibrous-ZnO/PVDF composite (Figure 4.3) were consistent with the peaks for the ZnO fiber mat. The SEM images of the composite (Figure 4.5) suggested that the high aspect ratio ZnO fragile fibers had been broken into short fibers (~2 μm in length) during the casting procedure. Moreover, the in-plane distribution and projection of the mat appear to be maintained, and the ZnO fillers were well-dispersed in the PVDF matrix. Control of the aspect ratio and the volume fraction of the fillers (~10% in this work) was not in the scope of this paper, but these factors and their effects in the composite properties are worth investigating in future studies. Nevertheless, the idea of using an inorganic filler network by electrospinning for the benefit of securing the dispersion of the fillers in the composite is considered to be a major contribution in the present work. In addition, incorporating the fiber network into a hot press-cast composite film enabled both handling and dielectric measurement.

<table>
<tr><td>2μm</td><td>EHT = 8.00 kV</td><td>Signal A = RBSD</td><td>Date :26 May 2008</td></tr>
<tr><td>Mag = 10.00 K X</td><td>WD = 8 mm</td><td>Photo No. = 6070</td><td>Time :19:25:10</td></tr>
</table>

SE  Zn

(a)                                                    (b)
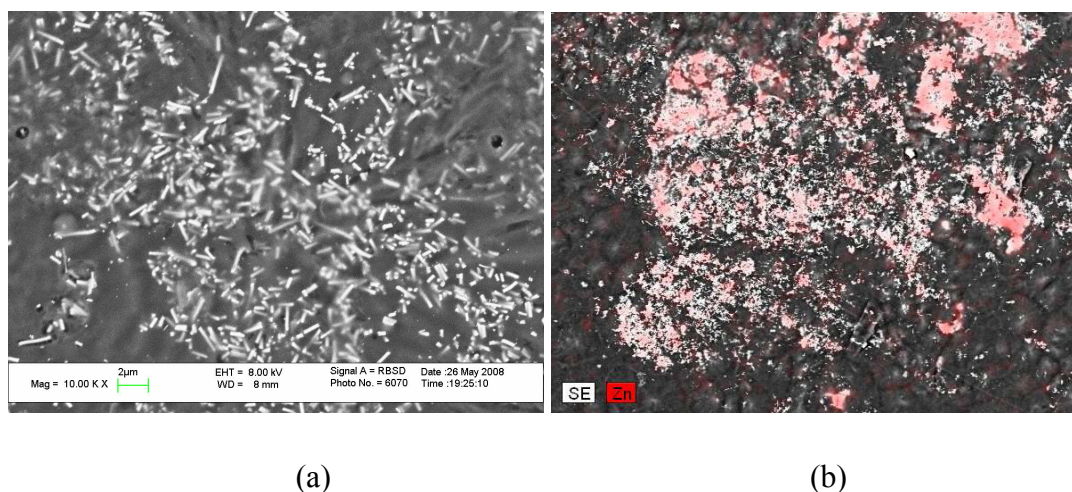
**Figure 4.5:** Fibrous-ZnO/PVDF composite film a) back-scattered SEM image, b) EDX spectra obtained using a beam of 15kV accelerating voltage.

## 4.4.2 Dielectric properties of the fibrous-ZnO/PVDF composite film

This section presents dielectric measurements to determine the dielectric response, $\varepsilon'$, as well as the dielectric loss ($\tan \delta = \varepsilon'' / \varepsilon'$) of the PVDF and fibrous-ZnO/PVDF composite films. Dielectric properties of the samples were probed by using Hewlett-Packard 4194A Impedance/Gain-Phase Analyzer. Measurements per test temperature were taken between 100 Hz and 1 MHz, while the temperature scan was made from 30 to 150 ºC at every increment of 10 ºC. The measurement system used a PT 100 resistor in direct thermal contact with the sample, providing accuracy better than 0.1 ºC, by using the NOVOTHERM Temperature Control Unit. The time for each frequency sweep was approximately one minute. Alternating Current (AC) dielectric properties were analyzed by monitoring the capacitance and conductivity. For each temperature, the real and imaginary part was recorded for the dielectric permittivity as well as time, temperature and frequency. The dielectric response or relative permittivity $\varepsilon'$ (measure of stored polarization energy) of the PVDF cast film and the fibrous-ZnO/PVDF composite film had changed as the frequency and temperature were varied. The relevant frequency-temperature scans for the two films are presented in Figure 4.6.

|      |      |
|------|------|
| (a)  | (b)  |

**Figure 4.6:** Dielectric response: frequency-temperature scan, a) PVDF film obtained by melt pressing of a single-layer, solution-cast film, and b) fibrous-ZnO/PVDF composite film.

The behavior of the dielectric response is qualitatively similar. In particular, a comparison of the low frequency versus high frequency response revealed that the relative permittivity $\varepsilon'$ decayed as the frequency was increased. Moreover, quantitative comparison of the two films, ZnO/PVDF composite vs. the PVDF specimen, showed a substantial increase by a factor of 10, over all frequency-temperature combinations for the composite (Figure 4.6 a vs. Figure 4.6 b). The polarization mechanism driving the measured dielectric behavior of the fibrous ZnO/PVDF composite was thought to be the interfacial polarization jump for two reasons. The first was due to the fact that the other three mechanisms—electronic, ionic, and molecular or dipolar—typically impart polarization relaxations or resonance as observed, but at much higher frequencies [33, 34] than were scanned. Second, by creating the large amounts of sub-micron filler/polymer interfacial area, the dielectric behavior was enhanced, as shown in Figure 4.6 b, when compared to the dielectric response measured on a bulk ZnO/PVDF composite [22, 23]. With comparable ZnO volume fractions at ~10%, the dielectric response of the fibrous-ZnO/PVDF composite (near 30 at 100 Hz) was twice that of the bulk-ZnO/PVDF composite (~14.0 maximum at room temperature and 100Hz), as reported by Wang et *al.* [22]. This enhancement in dielectric behavior could be attributed to the ceramic/polymer interfaces acting as effective blocking barriers, since they limit the charge carrier motion and give rise to interfacial polarization [35, 36],

which was further evidenced by the increase in permittivity with decreasing frequency [21]. Furthermore, the internal interfaces (e.g., grain boundaries) of the polycrystalline ZnO fibers also contributed dielectric polarization [24, 35, 37]. Different polarizabilities along different crystallographic directions occurred, depending on the orientation of crystallites forming the electrospun/sintered fiber.

Another salient property of a dielectric is the ability to support an electrostatic field, while dissipating minimal energy in the form of heat. A lower dielectric loss (the proportion of energy lost as heat) suggests a more effective dielectric material. By considering the loss tangent, which is the ratio of energy dissipated to energy stored, the overall dissipation factor could be determined, as shown in Figure 4.7 for both films. Despite the differences between the magnitude of stored energy for PVDF and ZnO/PVDF composite films, the loss tangent for both films remained in the same scale. The qualitative behavior, on the other hand, differed, manifested by a shift to higher frequencies in the polarization relaxation associated with the dielectric loss, as also observed by Park et *al.* [38]. Moreover, the dielectric loss tends to increase at elevated temperatures in Figure 7.



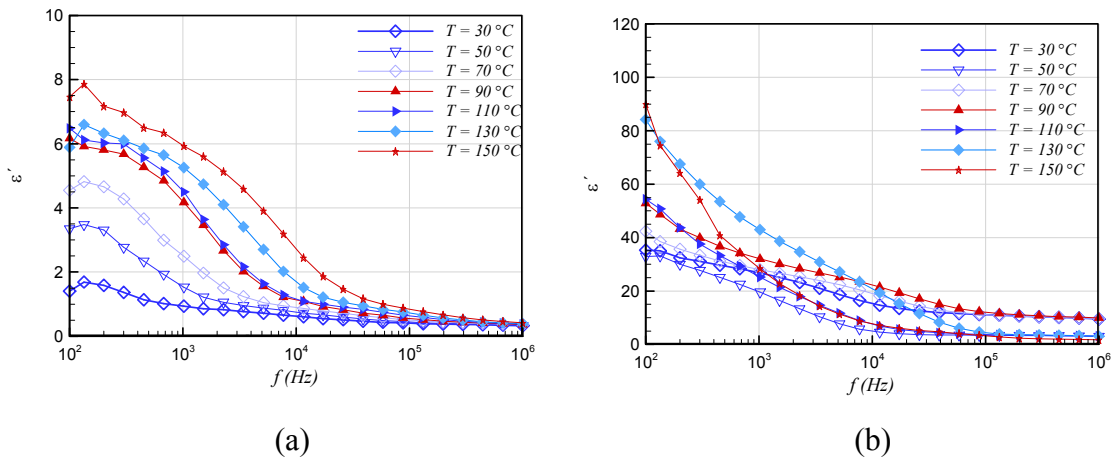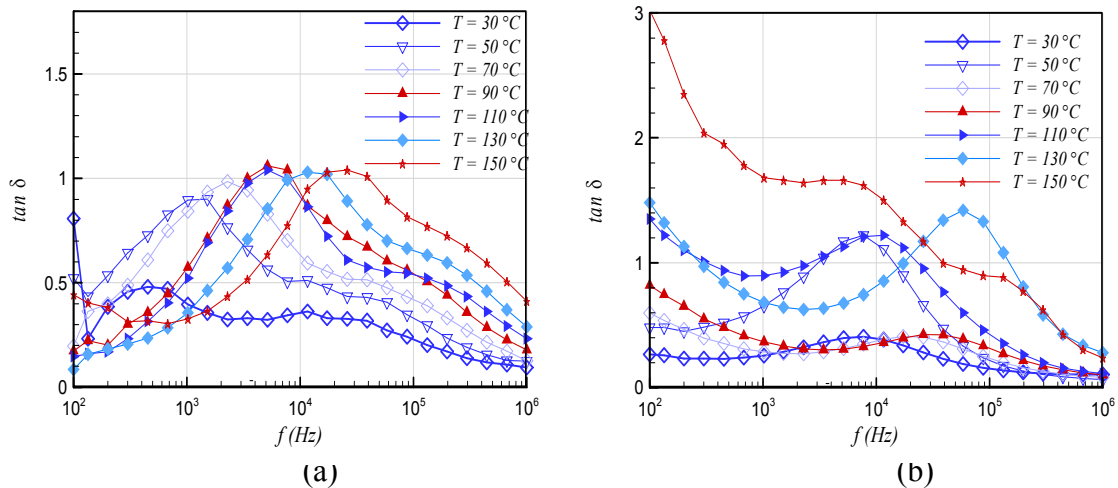**Figure 4.7:** Dielectric loss: frequency-temperature scan a) PVDF film obtained by melt pressing of a single-layer, solution-cast film, and b) fibrous-ZnO/PVDF composite film.

Closer inspection of the spectra in Figure 4.6 and Figure 4.7 reveals that the effect of temperature on the real part of the dielectric response $\varepsilon'$, of fibrous-ZnO/PVDF

composite did not impart a regular trend. The irregularity or anomaly could be seen more clearly on plots of T vs. $\varepsilon'$ and T vs. $\tan\delta$ for specific test frequencies, as reflected by the data collected at 1 kHz and 1 MHz (Figure 4.8). The stable dielectric properties appeared in the range of 60-100 ºC. The deviation or discontinuities on the otherwise regular, trend-like behavior occurred in the 40-60 ºC range, as well as at elevated temperatures above 100 ºC. Note that a similar plot was also reported by Hong et *al.* [21], for the ZnO/LDPE composite, showing a similar monotonic increase of the dielectric response from room temperature up to 100 ºC, albeit lacking measurements at 50, 60 and 90 ºC.
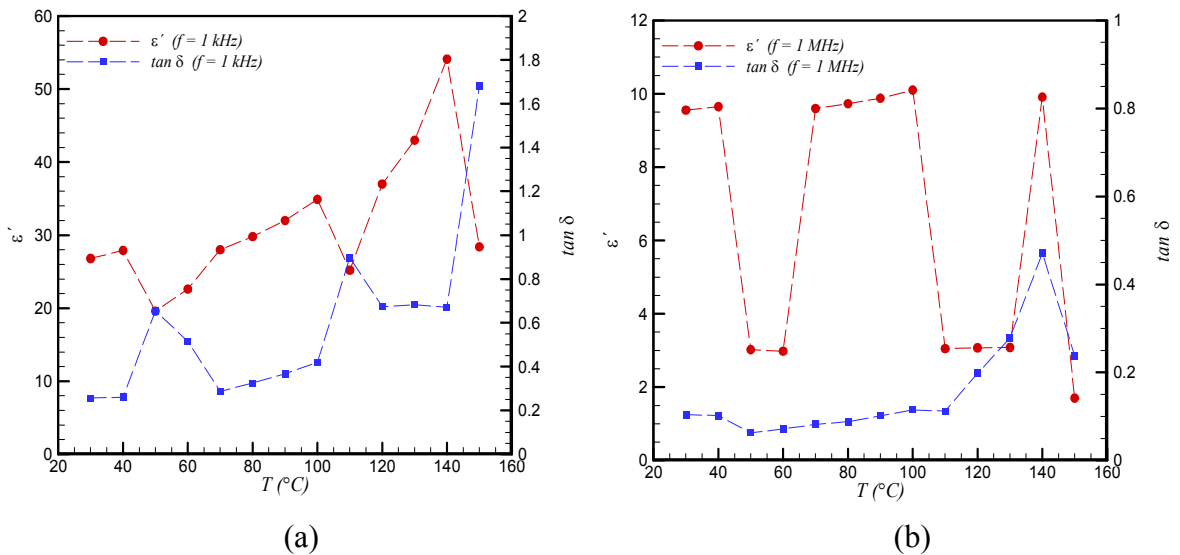


**Figure 4.8:** Temperature effect on the dielectric response and loss of the fibrous-ZnO/PVDF composite: a) at 1 kHz and b) at 1MHz.

The dielectric response of the composite is built up by the contributions of both PVDF and ZnO. Due to discontinuities at elevated temperatures, particularly above 90 ºC, one may suspect that the moisture uptake of the composite could affect the dielectric response of the material. Because of the large surface area and high surface energy of the ZnO filler, the fibers could be absorbing more target molecules, thereby producing hydroxyl radicals [31]. Another possibility would be the formation of surface defects on ZnO nanostructures and associated OH groups at the surface after thermal treatment [39]. Both possibilities, the moisture uptake of the composite and defects driven surface chemistry of the ZnO, point to the OH groups or radicals as the potential cause for the anomalies when temperature varies. Furthermore, the sudden drop in the dielectric

response was observed beyond 140 ºC. A similar drop was also observed by Wang et *al.* [22] for their ZnO/PVDF and by Deng et *al.* [40] for $BaTiO_3$/PVDF composite specimens, which was attributed to the thermal expansion and subsequent softening of the polymer matrix PVDF, which has a melting onset at ~130 ºC. In order to evaluate the anomaly or decrease of the dielectric response around 50-60 ºC and at around 100 ºC, and whether they are OH-groups related, isothermal frequency analysis was also performed on a pellet specimen of ZnOH prepared from a ZnAc and $NH_4OH$ solution. Figure 4.9 shows the ZnOH dielectric behavior as a function of temperature at 1 kHz and 1 MHz.
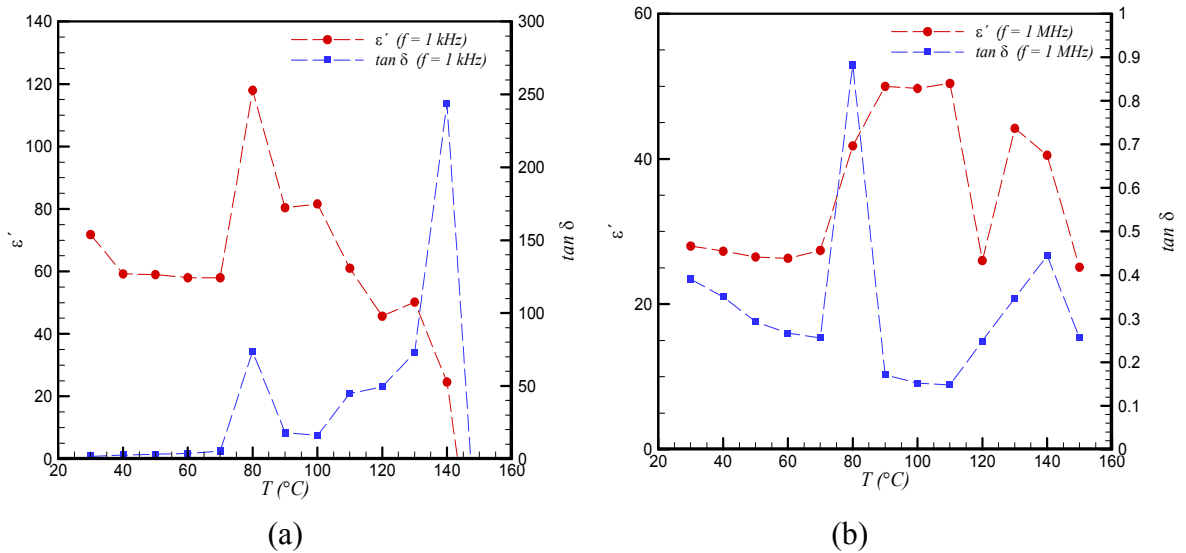


**Figure 4.9:** Temperature effect on the dielectric response and loss of ZnOH a) at 1kHz and b) at 1MHz.

The dielectric response decreased at ~50 and 60 ºC. As the temperature increased, the fluctuating values were attributed to the increased OH movements, generating more OH/OH interface in the ZnOH. After 90 ºC, the steep increase of the dielectric response appeared to stop and sharply drop at 110 ºC. Changes between 90-120 ºC were caused by moisture removal from the specimen. Fluctuations in the fibrous-ZnO/PVDF composite film could also be attributed to the OH groups, which appear to be common in the composite and the ZnOH specimens. Note that a higher dissipation was observed in the ZnOH sample than in fibrous-ZnO/PVDF composite due to higher fraction of the OH groups in ZnOH and associated movements. The existence or sign of OH groups was additionally confirmed by Raman spectroscopy (Figure 4.10), which showed peaks

for the stretching mode of the OH groups in the anticipated range of 2800 to 3600 cm$^{-1}$ [41].
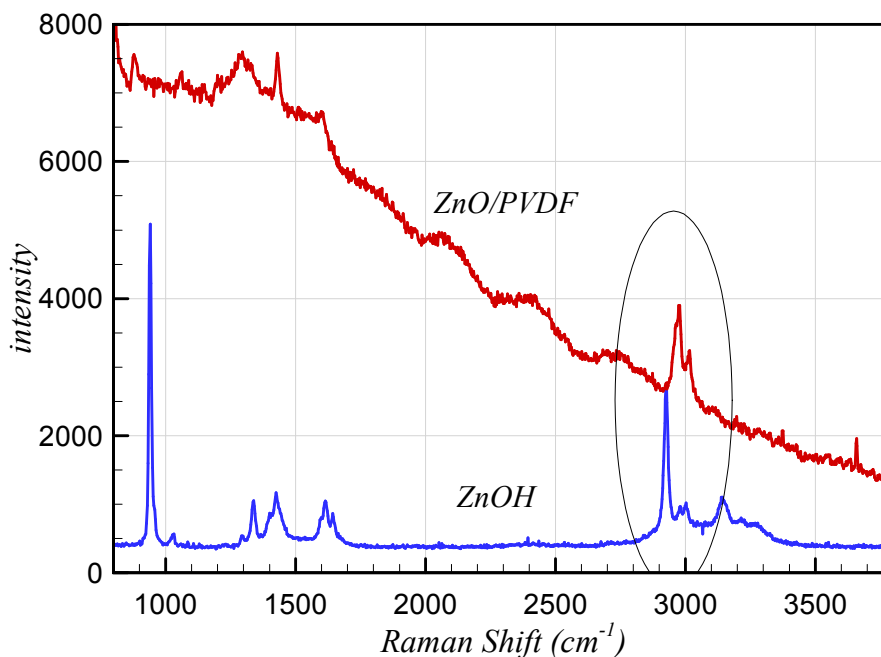


**Figure 4.10:** Raman Spectra of the fibrous-ZnO/PVDF composite and ZnOH samples in the range of 800-3800 cm$^{-1}$.

## 4.5 CONCLUSION

A poly(vinyl alcohol)-zinc acetate solution was electrospun to produce randomly oriented precursor polymeric fiber mats. The precursor mats were subjected to a controlled thermal treatment (calcinations and sintering) to form the ZnO fibrous structures. The mechanical drawback of the ZnO fibrous mat, being extremely fragile, was circumvented by first sandwiching the mat between solution cast PVDF films and then making a polymer matrix-composite via hot-press melt casting.

The use of an inorganic filler network by electrospinning for the benefit of securing the dispersion of the fillers in the composite was herein originally introduced and demonstrated. The network of high aspect ratio fibrous ZnO had been altered during the melt casting, and ZnO short fibers of nanoscale diameter in the PVDF matrix were obtained instead. The in-plane distribution of the ZnO fillers (short fibers) in the

PVDF matrix appears to comply with the projection of the pristine ZnO mat prior to hot pressing.

Moreover, the proposed process flow for the fibrous-ZnO/PVDF flexible composite facilitated handling and enabled measurements for dielectric properties, not practical on a ZnO fibrous mat. The ZnO short fibers of high surface area and their polycrystalline morphology allowed the generation of interfacial polarization, due to both the increase in dipoles formed at ZnO/PVDF interface, as well as at internal interfaces in the fibers of the composite film. The enhanced interfacial polarization had significantly increased the dielectric response over the bulk properties of both constituents, as well as over bulk-ZnO/PVDF, albeit with a slight penalty on dielectric loss was measured. Increasing temperatures and decreasing frequencies had increased the dielectric response of the ZnO/PVDF composite. The stable dielectric properties appeared in the range of 60-100 ºC. The observed temperature dependence and instabilities were attributed to OH groups in the fibrous-ZnO/PVDF composite.

## ACKNOWLEDGMENT

## 4.6 REFERENCES

1. S. Roy, and S. Basu, *Bulletin of Materials Science*, **25(6)**, 513-515 (2002).

2. Q. Zhang, T. P. Chou, B. Russo, S. A. Jenekhe, and G. Cao, *Adv. Funct. Mater.*, **18**, 1654–1660 (2008).

3. B. Pal, and M. Sharon, *Materials Chemistry and Physics*, **76**, 82-87 (2002).

4. C. X. Xu, X. W. Sun, B. J. Chen, and P. Shum, *Journal of Applied Physics*, **95(2)**, 661-666 (2004).

5. P. Viswanathamurthi, N. Bhattarai, H. Y. Kim, and D. R. Lee, *Nanotechnology*, **14**, 320-323 (2004).

6. P. M. Martin, M. S. Good, J. W. Johnston, L. J. Bond, and J. D. Lin, *Thin Solid Films*, **379**, 253-258 (2000).

7. Z. Qifeng, P. C. Tammy, R. Bryan, A. J. Samson, and C. Guozhong, *Advance Materials*, **18**, 11 (2008).

8. L. W. Zhang, Y. K. Xiang, D. Yang, G. Puxian, L. H. William, Y. Rusen, and Z. Yue, *Advance Materials*, **14**, 10 (2004).

9. M. H. Zhao, Z. L. Wang, and S. X. Mao, *Nano Letters,* **4(4),** 587-590 (2004).

10. P. X. Gao, and Z. L. Wang, *Journal of Applied Physics*., **97**, 044304 (2005).

11. Y. C. Wang, I. C. Leu, and M. H. Hon, *Electrochemical Solid State Letters*, **5(4)**, C53, (2002).

12. Y. Li, G. W. Meng, L. D. Zhang, and F. Philipp, *Applied Physics Letters*, **76**, 2011-2013 (2001).

13. C. Kim, K. Yang, M. Kojima, K. Yoshida, Y. J. Kim, Y. Kim, and M. Endo, *Advanced Functional Materials*, **16**, 2393-2397 (2006).

14. H. W. Kim, E. Kim, and J. C. Knowles, *Advanced Functional Materials*, **16**, 1529 (2006).

15. I. S. Chronakis, *Journal of Materials Processing Technology*, **167**, 283-293 (2005).

16. W. Sigmund, J. Yuh, H. Park, V. Maneeratana, G. Pyrgiotakis, A. Daga, J. Taylor, and J. C. Nino, *Journal of American Ceramic Society*, **89(2)**, 395-407 (2006).

17. Y. Wang, M. Aponte, N. Leon, I. Ramos, R. Furlan, and N. Pinto, *Journal of American Ceramic Society*, **88(8)**, 2059-2063 (2005).

18. H. Wu, and W. Pan, *Journal of American Ceramic Society*, **89**, 699 (2006).

19. Y. A. Dzenis, *Science*, **304**, 1917 (2004).

20. Y. Kim, D. Y. Lee, M. H. Lee, N. I. Cho, Y. S. Song, and S. J. Lee, *Journal of the Korean Physical Society*, **53**, 421-425 (2008).

21. J. I. Hong, P. Winberg, L. S. Schadler, and R.W. Siegel, *Materials Letters*, **59**, 473-476 (2005).

22. G. Wang, Y. Deng, Y. Xiang, and L. Guo, *Advanced Functional Materials*, **18**, 1-9 (2008).

23. T. J. Lewis, *IEEJ Transactions on Fundamentals and Materials*, **126 (11)**, 1020-1030 (2006).

24. C. K. Chiang, and R. Popielarz, *Ferroelectrics*, **275**, 1–9 (2002).

25. J.A. Malmonge, L.F. Malmonge, G.C. Fuzari Jr., S.M. Malmonge, W.K. Sakamoto, *Polym. Compos*., early view, (2008)

26. L. Flandin, M. Verdier, B. Boutherin, Y. Brechet, and J. Y. Cavaille, *J. Polym. Sci., B, Polym. Phys*., **37**, 805 (1999).

27. L. Dan, and X. Younan, *Advance Materials*, **16**, 14 (2004).

28. O. S. Yordem, MSc Thesis, Piezoelectric Ultrafine Polymer and Ceramic Fibers by Electrospinning: Process Development and Characterization, Sabancı University, Istanbul, Turkey (2006).

29. O. S. Yordem, M. Gülleroğlu, E. Öğüt, Y.Z. Menceloğlu, M. Papila, Proceedings of 21$^{st}$ Annual Technical Conference, American Society for Composites, Dearborn MI, September (2006).

30. X. Zhiyong, H. Jiann-Yang, L. Bowen, H. Xiaodi, and W. Howard, *JOM,* **60**, 29-32 (2008).

31. R. Y. Hong, L. L. Chen, J. H. Li, H. Z. Li, Y. Zheng, and H. Ding, *J. Polym. Adv. Technol.*, **18**, 901–909 (2007).

32. F. Lu, W. Cai, and Y. Zhang, *Adv. Funct. Mater*., **18**, 1047–1056 (2008).

33. H. Foll, Electronic Materials, lecture notes, U.of Kiel, http://www.tf.unikiel.de/matwis/amat/elmat_en/index.html, last accessed on September 17, (2008).

34. J. Xu, and C. P. Wong, *J. of Electronic Materials*, **35**, 5, 1087-1094 (2006).

35. J.-C. M'Peko, *Journal of Materials Science Letters*, **19-21**, 1925-1927 (2000).

36. R. V. Rao, and M. H. Shridhar, *Materials Letters*, **55**, 34-40 (2002).

37. F. Bernardini, and V. Fiorentini, *Physical Review B*, **57**, 16 (1997).

38. S. H. Park, E. C. Lim, K. S. Park, D. H. Kang, S. O. Han, and D. C. Lee, The Dielectric Properties of Functional PVDF thin films by Physical Vapor Deposition Method, *Proceedings of the 5$^{th}$ International Conference on Properties and Applications of Dielectric Materials* May 25-30 (1997), Seoul, Korea.

39. A. B. Djurisic, Y. H. Leung, K. H. Tom, Y. F. Hsu, L. Ding, W. K. Ge, Y. C. Zhong, K. S. Wong, W. K. Chan, H. L. Tom, K. W. Cheah, W. M. Kwok, and D. L. Philips, *Nanotechnology*, **18**, 095702 (2007).

40. Z. M. Dang, J. B. Wu, L. Z. Fan, and C. W. Nan, *Chemical Physics Letter*, **376**, 389–394 (2003).

41. H. Zhou, H. Alves, D. M. Hofmann, B. K. Meyer Kaczmarczyk, A. Hoffmann, and C. Thomsen, *Phys. Stat. Sol*., **229**, No. 2, 825–828 (2002).

# CHAPTER 5

## 5 PAPER-3

**Processing Conditions and Aging Effect on the Morphology of PZT Electrospun Nanofibers and on Dielectric Properties of the Resulting 3-3 PZT/Polymer Composite**

Paper-3 was accepted by the Journal of American Ceramic Society.

Road map of the paper-3 is given above.

```
                              ┌──────────────────┐
                              │   EXPERIMENTAL   │
                              └──────────────────┘
                                       │
                        ┌──────────────────────────────┐
                        │   Making PZT precursor solution │
                        └──────────────────────────────┘
```

| Pb acetate trihydrate | 2- methoxyethanol | Zr n-butoxide in Ti- isisopropoxide |

| Mixed and dissolved at 80 $^o$C | | Mixed and dissolved at 80 $^o$C |

| Dehyration at 120 $^o$C for 90 min. | | Dehyration at 120 $^o$C for 90 min. |

Mixed at 80 $^o$C

Dehyration at 120 $^o$C for 90 min. → 0.4 M , Zr/Ti molar ratio: 1:1

PVP is added in PZT precursor solution at 6wt%, 12wt%, 22wt%, 28wt%, 34wt%

Aging polymer precursor solution for investigating the optimum condition for PZT fiber formation

Electrospinning of polymer solution
Voltage: 12 kV
Distance: 10 cm

Sintering of the resultant fiber mat at 700 C for 1 hour.
Heating rate: 0.5 $^o$C/min.

Fibrous ZnO/PVDF matrix composite formation

Polymer matrix was poured on the sintered PZT fiber mat and composite was dried at room T for 10 hours.

CHARATERIZATION

SEM

Crystalline Phases by XRD

Aging period vs. fiber diameter & viscosity of precursor solution

Dielectric Analysis
Temperature: 30-150 $^o$C
Frequency: 100 Hz-1 MHz
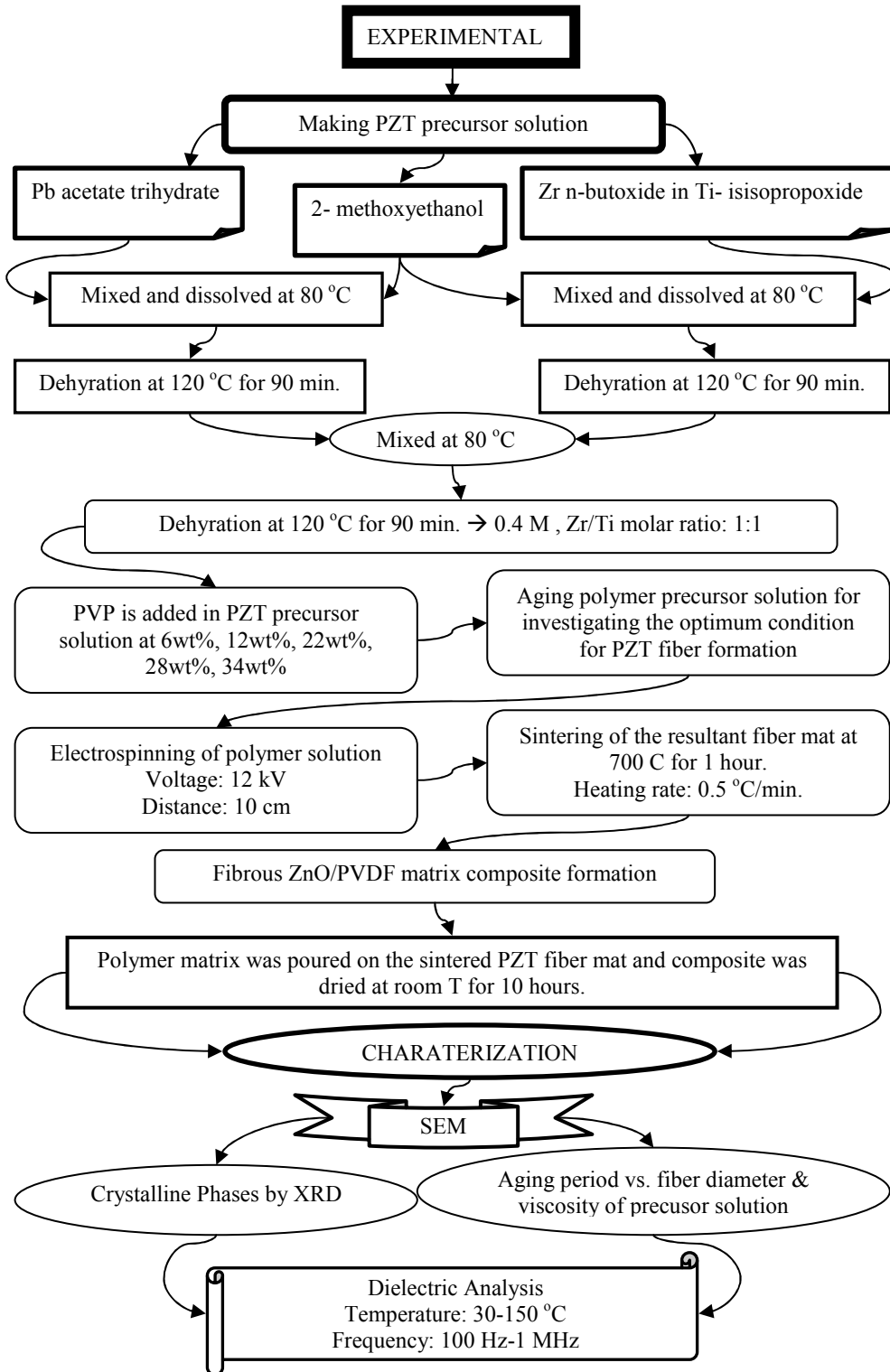
74

# Processing Conditions and Aging Effect on the Morphology of PZT Electrospun Nanofibers and on Dielectric Properties of the Resulting 3-3 PZT/Polymer Composite

Ebru Mensur Alkoy, Canan Dagdeviren, Melih Papila

*Sabancı University, Faculty of Engineering and Natural Sciences, Material Science and Engineering, Tuzla, Istanbul, 34956 (Turkey)*

## 5.1 ABSTRACT

Lead zirconate titanate (PZT) nanofibers are obtained by electrospinning a sol-gel based solution and polyvinyl pyrrolidone (PVP) polymer, and subsequent sintering of the electrospun precursor fibers. The average diameter of the precursor PZT/PVP green fibers has increased with the aging of the precursor solution along with an increase in the viscosity. Bead-free uniform green PZT/PVP fibers were collected at about ~ 230 nm average fiber diameter using 28wt% PVP ratio solution with viscosity of 290 mPa. Shrinkage of 40% was recorded on the fiber diameter after sintering. X-ray diffraction (XRD) pattern of the annealed PZT fibers exhibits no preferred orientation and a perovskite phase. Preparation of 3-3 nanocomposites by infusion of polyvinylester into the nanofiber mat facilitates successful handling of the fragile mats and enables measurements of dielectric properties. The dielectric response of the PZT/polyvinylester nanocomposite of about 10% fiber volume fraction was found to be fairly stable and vary from 72 to 62 within the measurement range.

**Key words:** PZT; nanofibers; electrospinning; ferroelectrics; aging.

## 5.2 INTRODUCTION

Lead zirconate titanate is the most widely used ferroelectric material in ultrasonic transducers, non-volatile random access memory devices, microelectromechanical devices, sensor and actuator applications due to its high dielectric response, high electromechanical coupling coefficient, and large remnant polarization [1, 2]. This material can be processed into various forms such as bulk ceramics, thin films and fibers depending on application area. PZT in fiber form is appealing because of its increased anisotropy, improved flexibility and strength over monolithic PZT ceramics. Micron-scale PZT fibers are usually incorporated into a polymer matrix to obtain smart piezocomposite structures [3]. They can also be used as individual fibers in novel actuator and sensor devices, such as energy harvesting and self-powered in-vivo medical devices, high-frequency transducers, non-volatile ferroelectric memory devices [4]. Nano-scale PZT fibers are also expected to find wide applications particularly in nano-electronics, photonics, sensors and actuators [5].

There are a few methods to obtain PZT in fiber form. Sol-gel, viscous suspension spinning process (VSSP), and extrusion, for instance, are applied to produce PZT fibers typically in the micron scale [6-8]. Electrospinning technique has recently gotten attention because the fibers at micro- and even nano-scale can be produced by this method. Nano-scale PZT fibers have been also produced by electrospinning method [4, 9-11]. Zhou et *al.* [12] have produced PZT nanofibers by electrospinning and found that these fibers exhibit significant reversible piezoelectric strains under applied electric field. The level of this strain was measured to be about 4.2% which is reportedly six times larger than that observed in thin films.

The objectives of this study are to investigate the processing conditions in electrospinning of polymeric precursor fiber mats followed by annealing for PZT nanofibers, to examine the phase and morphology of these nanofibers prior and posterior to annealing process and to characterize the dielectric properties of the resultant PZT/polyvinylester nanocomposite.

## 5.3 EXPERIMENTAL

The PZT sol-gel precursor solution was prepared from lead acetate trihydrate, titanium isopropoxide and zirconium n-butoxide in n-butanol. 2-methoxyethanol was used as the main solvent. The details of the solution preparation method is shown in Figure 5.1 a and were reported in a previous article [13]. Final concentration of the precursor sol-gel solution was 0.4 M and Zr/Ti mol ratio was 1:1. Additionally, 5mol% lead (Pb) excess was added to the precursor solutions to compensate lead loss during annealing. Different polymers can be used to provide electrospining of PZT [9-11]. Polyvinyl pyrrolidone was chosen and added to the sol-gel solution with ratios ranging from 6 wt% to 34 wt% in this study. These ratios were determined based on some preliminary experiments. Initially, various PVP ratios starting from 1wt% were studied systematically with small increments until the first fiber formation was observed.  A home-made, electrospinning set-up allowing computer controlled PZT/polymer precursor solution flow rate was used to prepare the green fiber mats. A schematic of the electrospinning set-up is shown in Figure 5.1 b. The applied voltage (12 kV) and the distance between the tip of the needle and the collector (10 cm) resulting in electrostatic field of 1.2 kV/cm were kept fixed after preliminary screening experiments. The size of needle was 300μm and the pumping speed was 0.5 ml/hour. The same processing conditions were used for all the electrospinning experiments in this study.
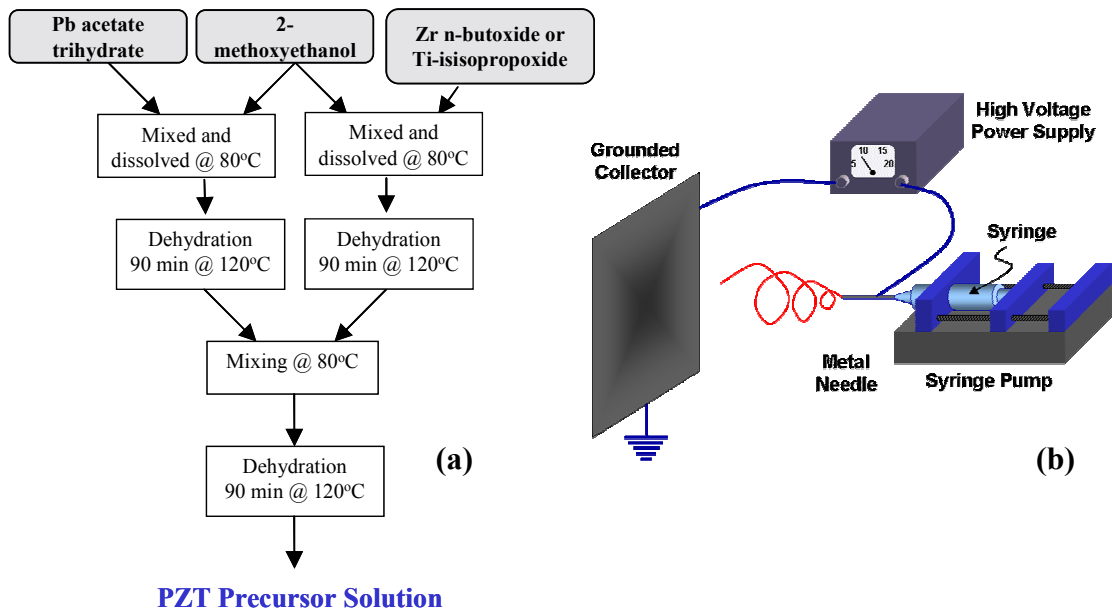


**Figure 5.1:** a) The process flow chart of precursor sol-gel PZT solution, b) A schematic of the electrospinning setup.

The viscosity of the precursor solution and PVP mixture were measured by Brookfield DVIII+ rheometer using cone/plate sample holder. The measurements were taken at various shear rates ranging from 38.4 $sn^{-1}$ to 768 $sn^{-1}$. The viscosity was found to stay stable in this measurement range and only the results taken at 76.8 $sn^{-1}$ shear rate were reported in this article. The effect of associated PVP polymer solution concentration was investigated on the morphology of the green precursor fibers. The effect of aging the precursor solution on the morphology of green fibers was also investigated by electrospinning fiber mats from solutions with 22wt% PVP content stored for various periods. The solutions were stored in closed containers to prevent evaporation during the aging process. The viscosity of the aged solutions was recorded prior to electrospinning.

Green fibers were sintered at 700 ºC with two different heating rates (0.5 or 5 ºC/min). Thermo Gravimetric Analysis (TGA) was used to identify the crucial steps in the pyrolysis and sintering processes.

After obtaining the PZT fiber mats, PZT/polyvinylester composite samples were prepared. T676NA vinyl ester, Accelerator D (styrene 10wt%, N-N dimethylaniline with >89 wt %), Accelerator G (styrene >80wt %) and Butanox LPT (methyl-ethyl ketone peroxide in diisobutyl phthalate) were mixed to obtain the polymer matrix of the composite. This solution was poured on to the sintered PZT fiber mat and this sample was kept under vacuum for five minutes to eliminate air trapped in the sample. Then the sample was dried 10 hours at room temperature.

Sintered mats were characterized by x-ray diffraction (XRD) and scanning electron microscopy (SEM). The dielectric response and loss of the PZT/polyvinylester composites were measured from 10 kHz to 1 MHz using an HP 41494A Impedance Analyzer. The samples were prepared into thin rectangular parallel plates and the dielectric measurements were taken by putting the samples between two parallel metal plates of the sample holder.

## 5.4 RESULTS and DISCUSSION

### 5.4.1 Microstructural features of green fiber mats

The microstucture and the average fiber diameter of as-prepared green and sintered nanofiber mats were examined by scanning electron microscope (SEM). Fig.2 shows the microstructure of PZT/PVP green mats at various PVP content in the solution. From Figure 5.2 a and Figure 5.2 b, small amount of PVP, such as 6wt% or 12wt%, was clearly seen to be insufficient to facilitate fiber formation. On the other hand, the concentration of the PVP polymer in the solution exceeding 22wt% appears to result in fibrous mat with reasonable amount of beads (Figure 5.2 c). In particular, bead-free uniform green PZT/PVP fibers of ~ 230 nm fiber diameter were collected using the 28wt% PVP ratio solution with viscosity of 290 mPa. These conditions were considered as optimal in this study (Figure 5.2 d). Further increase of the PVP content to 34 wt% resulted in smaller fiber diameter, but with extensive formation of large beads (Figure 5.2 e).
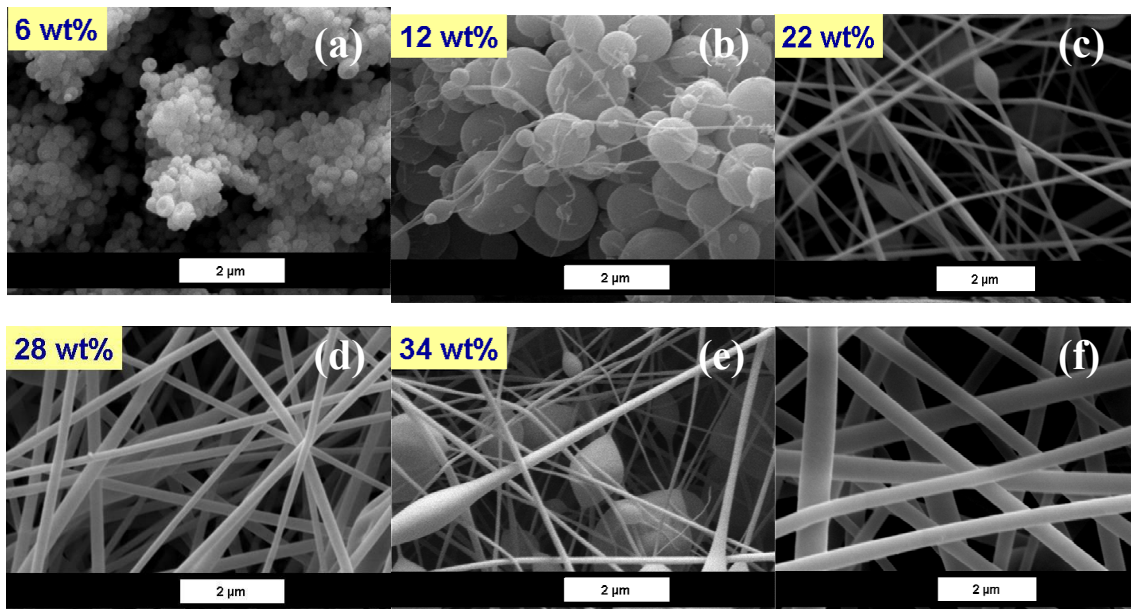


**Figure 5.2:** PZT/PVP green fibers from as-prepared solution with a) 6wt%, b) 12wt%, c) 22wt%, d) 28wt%, e) 34 wt% PVP content and f) PZT/PVP green fibers from 72 hour aged solution with 22wt% PVP content.

Additional viscosity measurements and investigation were carried out on the PZT precursor solution of 22wt% PVP, considered to be lower limit for reasonably dominant fiber formation, as a function of time in order to explore the effect of aging. Figure 5.3 shows the diameter of the PZT/PVP green fibers and viscosity of the precursor solution as a function of aging time. It is clearly seen from Figure 5.2 c and Figure 5.2 f, along with Figure 5.3, that the viscosity of the solution has a significant effect on the formation of fibers and fiber diameter. Another important and supporting correlation was also observed between the viscosity and the PVP content. The viscosity of the as-prepared (two hours mixed) solution was measured as 140 mPa (Figure 5.3). The average fiber diameter of the mats electrospun from this solution was determined to be 150 nm, however, a beaded structure was observed in these mats (Figure 5.2 c).

The viscosity of the same solution was recorded and nanofiber mats were electrospun after 24, 48 and 72 hours aging. From the SEM examinations of these mats, a bead-free mat structure was obtained from the 48 and 72 hours aged solutions. The viscosity of the 48 hours aged solution was measured as 270 mPa (Figure 5.3) and the average fiber diameter of the mats electrospun from this solution was determined to be 240 nm. When compared to the optimum conditions determined from the solution with 28wt% PVP content (viscosity = 290 mPa & fiber diameter = 230 nm), a remarkable correlation was observed. That is; the PVP content of the solution is important to obtain bead-free fiber mats, however, the real controlling factor appears to be the viscosity of the polymer solution. The PVP content is believed to be merely adjusting the viscosity of the solution. The change in the viscosity of the solutions as a result of aging is thought to be due to partial evaporation of the solvent in the polymer solution and formation of chain-like polymeric particles, which increases the viscosity of the solution. A similar effect of solution aging was observed in a previous study [14].
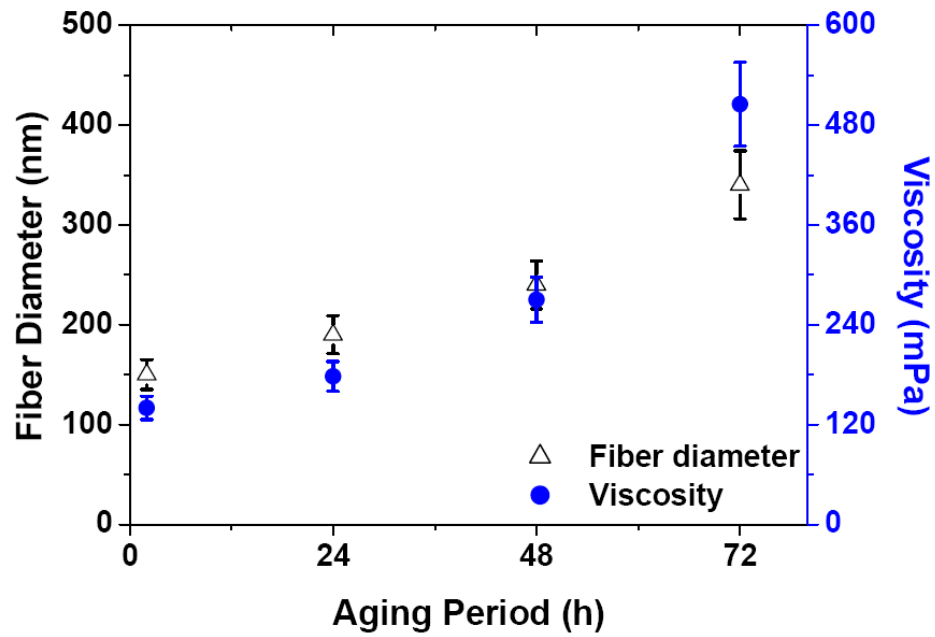
**Figure 5.3:** Variation of the fiber diameter and solution viscosity with aging.

## 5.4.2 Structure and microstructural features of the sintered PZT fibers

Thermogravimetric analysis (TGA) of the green fiber mats was done to identify thermal transitions and determine an appropriate annealing regime. From the TGA pattern in Figure 5.4, a large amount of weight loss was observed at 290 ºC and 420 ºC. These temperatures were deemed critical in the sintering of the fiber mats.
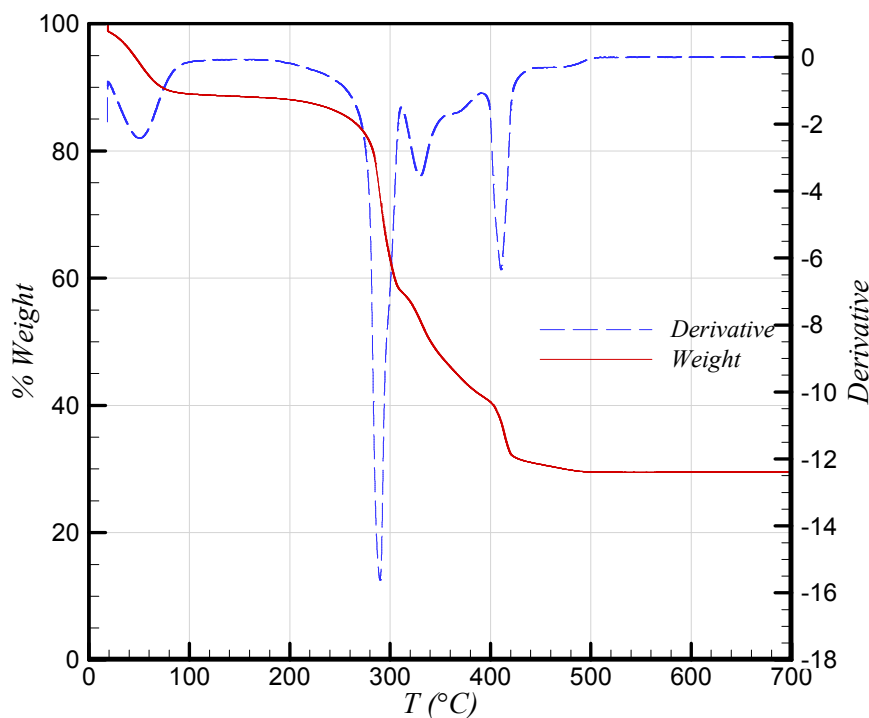
**Figure 5.4:** TGA analysis of the green fiber mats.

PZT fiber mats were annealed at 700 ºC for 1 hr, however, two different annealing regimes (heating rate = 0.5 ºC/min or 5 ºC/min) were investigated in accordance with the TGA results. The investigation of the sintering process was initially carried out on green fiber mats from the solution with 22wt% PVP content. At the slow heating regime (0.5 ºC/min) sufficient time was allowed for all organics to be systematically removed, leaving behind a relatively more uniform microstructure (Figure 5.5 a), whereas fast heating regime (5 ºC/min) yields a more complex microstructure where especially the morphology of the beads were different than the slow heating regime (Figure 5.5 b). It was observed that heating regime was influential on the microstructure. This was attributed to the rushed removal of the organic constituents. The mats produced from the solution with 28wt% PVP content also yielded similar microstructure (Figure 5.5 c). The cross-section of the fiber mats were shown in Figure 5.5 d. Shrinkage of approximately 40% was recorded on the fiber diameter after sintering.
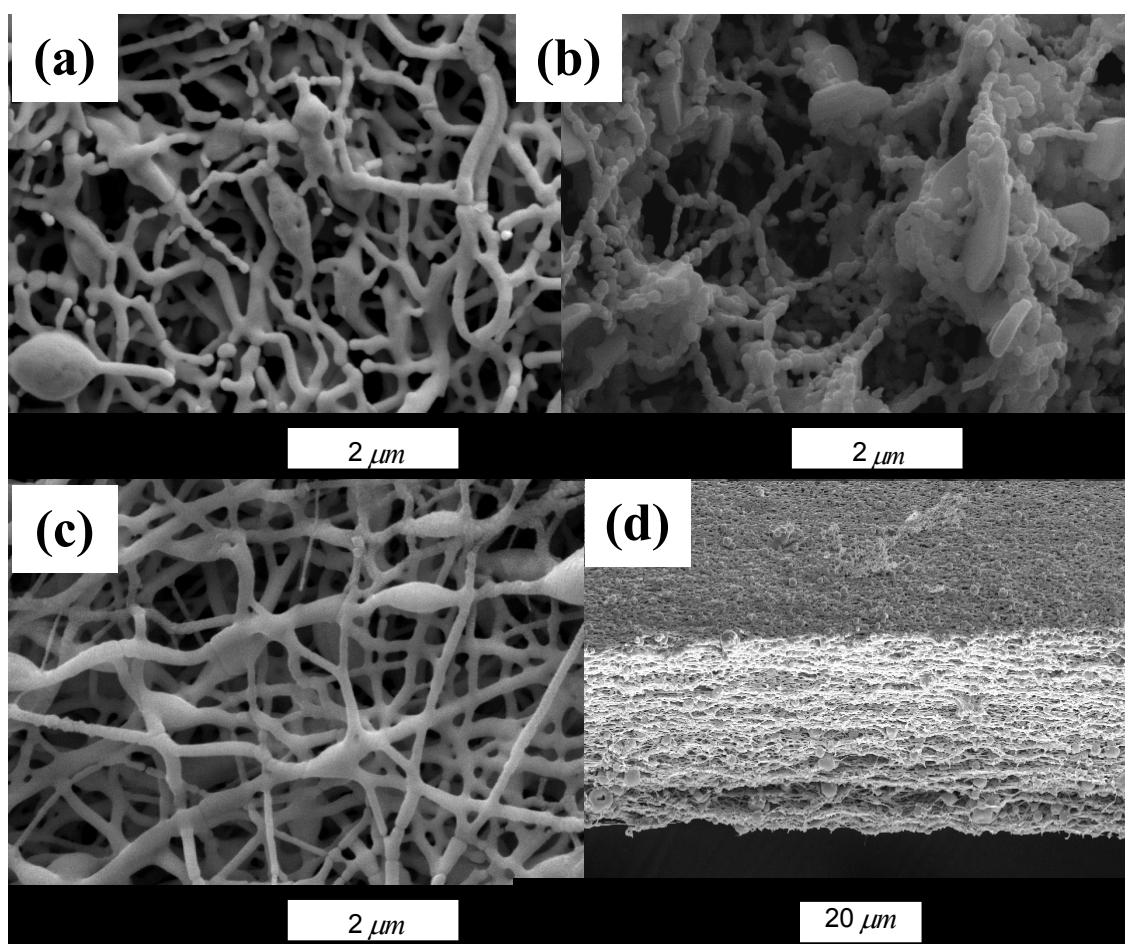
**Figure 5.5:** The micrographs of nanofiber mats prepared from the solution with various PVP content and sintered at 700°C for 1 hour with various heating regimes a) 22 wt% PVP and 0.5 °C/min, b) 22 wt% PVP and 5 °C/min and, c) 28 wt% PVP and 0.5 °C/min and, d) Cross sectional view of the sintered mat (22 wt% PVP and 0.5 °C/min).

The phase identification of the sintered PZT nanofibers was performed using XRD. The XRD pattern of the PZT fibers annealed at 700 ºC for 1 hr indicates that these nanofibers are crystallized in perovskite phase with no preferred orientation and with a small presence of lead oxide (PbO) (Figure 5.6). It is not possible to clearly identify from this pattern whether the PZT is crystallized with a tetragonal or a rhombohedral perovskite phase due to lower annealing temperature of 700 °C. However, when the PZT powders prepared from the same sol-gel solution were pressed into pellets and sintered at 1260 °C, a clear tetragonal peak splitting was observed at the (100)/(001) and (200)/(002) peaks [8].

**Figure 5.6:** XRD pattern of the PZT nano-fiber mat prepared from the solution with 28wt% PVP content and sintered at 700 °C for 1 hour.

## 5.4.3 Dielectric properties of the PZT nano-fiber/polymer nanocomposites

After fabricating the PZT fiber mats, PZT/polyvinylester composite samples were prepared. Polyvinylester was tried as the first polymer matrix material in this study. The effect of other matrix materials on the electrical properties will be investigated as a future work. The SEM micrograph of the composite structure is shown in Fig.38. When the microstructure of the mat is examined at higher magnification (the section marked with a rectangle in Figure 5.7 a), it is clearly visible from Figure 5.7 b that the polymer matrix phase has infiltrated thoroughly into the fiber network and an intimate mixture of two phases was obtained. Figure 5.7 c shows the backscattering electrons SEM image of the composite section where the PZT phase consisting of beads and fibers are visible with a bright-white contrast and the polyvinylester phase is identifiable as the darker-gray regions. Using Newnham's convention on connectivity of piezocomposites [15] the composite has 3-3 connectivity where the active PZT and the passive polymer matrix phases are both connected in three dimensions in microscale.
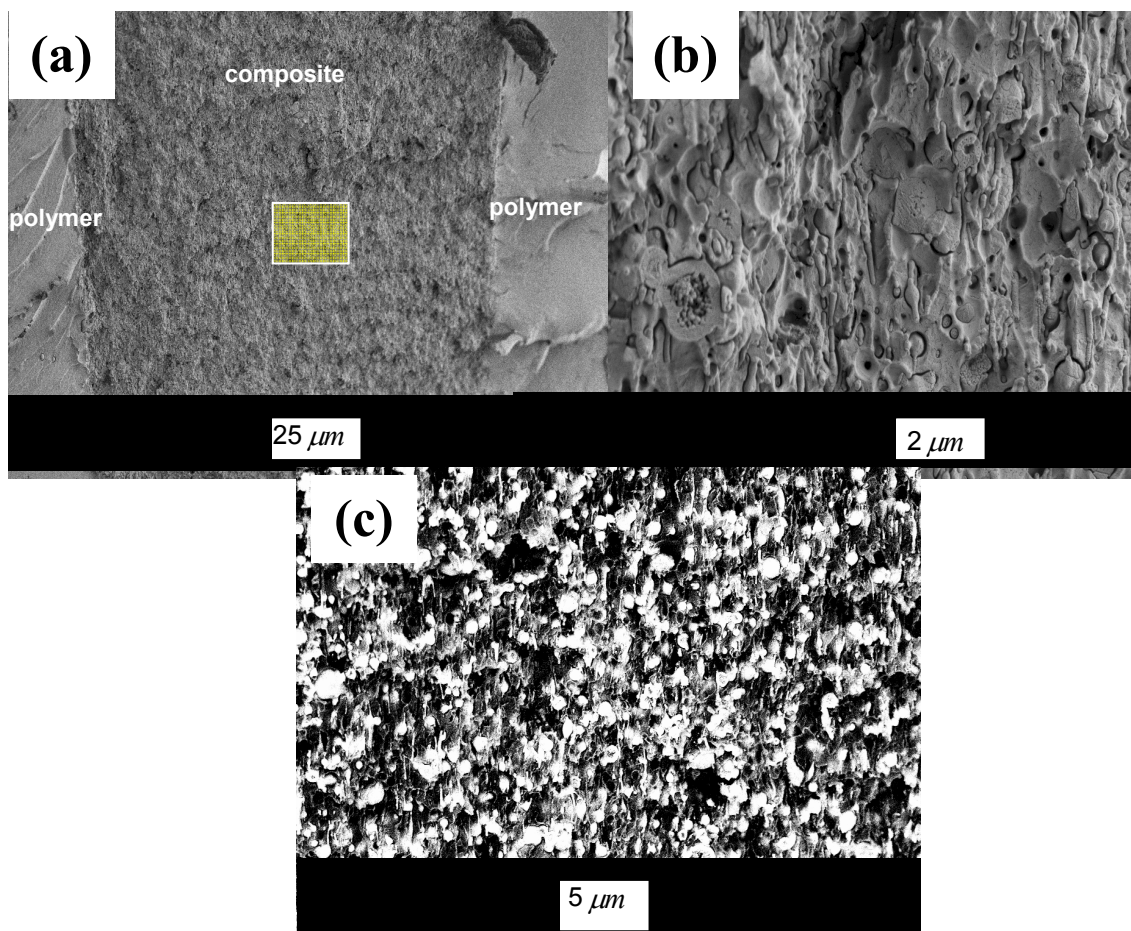
**Figure 5.7:** a) Cross sectional microstructure of PZT/polyvinylester composite, b) higher magnification of the rectangular section of a) and, c) Backscattering electrons SEM image of the composite section (PZT nano-fiber mat was prepared from the solution with 28 wt% PVP content and sintered at 700 °C for 1 hour with 0.5 °C/min heating rate).

The dielectric response, $\varepsilon'$, of the 3-3 composite was found to be fairly stable and vary from 72 to 62 within the measurement range (Figure 5.8). This value is more than an order of magnitude higher than the dielectric response of the polyvinylester which was measured as 3.2 in this study. This is due to the increasing contribution of PZT to the dielectric properties of the composites, since undoped PZT has a substantially higher dielectric constant (800 @ 1kHz) [16] than the polymer. Here, the dielectric constant of undoped PZT is taken as a reference point because doping elements affect the dielectric properties of PZT substantially. In our case a doping element has not been used in the preparation of the PZT precursor solutions.

The phase identification of the sintered PZT nanofibers was performed using XRD. The XRD pattern of the PZT fibers annealed at 700 ℃ for 1 hr indicates that these nanofibers are crystallized in perovskite phase with no preferred orientation and with a small presence of lead oxide (PbO) (Figure 5.6). It is not possible to clearly identify from this pattern whether the PZT is crystallized with a tetragonal or a rhombohedral perovskite phase due to lower annealing temperature of 700 °C. However, when the PZT powders prepared from the same sol-gel solution were pressed into pellets and sintered at 1260 °C, a clear tetragonal peak splitting was observed at the (100)/(001) and (200)/(002) peaks [8].

## 5.4.4 Dielectric properties of the PZT nano-fiber/polymer nanocomposites

After fabricating the PZT fiber mats, PZT/polyvinylester composite samples were prepared. Polyvinylester was tried as the first polymer matrix material in this study. The effect of other matrix materials on the electrical properties will be investigated as a future work. The SEM micrograph of the composite structure is shown in Fig.38. When the microstructure of the mat is examined at higher magnification (the section marked with a rectangle in Figure 5.7 a), it is clearly visible from Figure 5.7 b that the polymer matrix phase has infiltrated thoroughly into the fiber network and an intimate mixture of two phases was obtained. Figure 5.8 c shows the backscattering electrons SEM image of the composite section where the PZT phase consisting of beads and fibers are visible with a bright-white contrast and the polyvinylester phase is identifiable as the darker-gray regions. Using Newnham's convention on connectivity of piezocomposites [15] the composite has 3-3 connectivity where the active PZT and the passive polymer matrix phases are both connected in three dimensions in microscale.
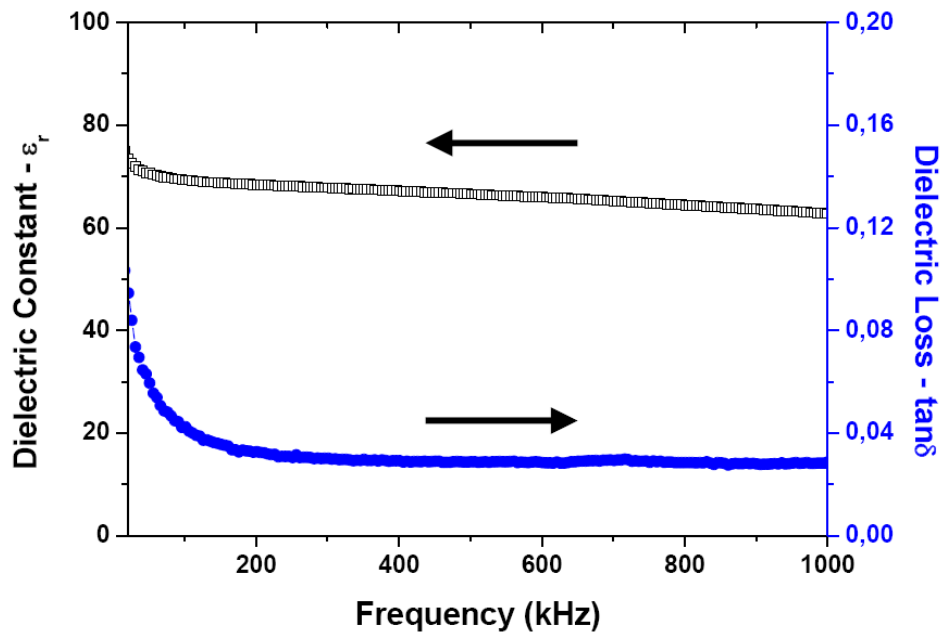
**Figure 5.8:** Dielectric response and loss of the PZT/ polyvinylester sample as a function of frequency at the room temperature.

The dielectric response, $\varepsilon^{'}$, of the 3-3 composite was found to be fairly stable and vary from 72 to 62 within the measurement range (Figure 5.8). This value is more than an order of magnitude higher than the dielectric constant of the polyvinylester which was measured as 3.2 in this study. This is due to the increasing contribution of PZT to the dielectric properties of the composites, since undoped PZT has a substantially higher dielectric constant (800 @ 1kHz) [16] than the polymer. Here, the dielectric constant of undoped PZT is taken as a reference point because doping elements affect the dielectric properties of PZT substantially. In our case a doping element has not been used in the preparation of the PZT precursor solutions.

The polymer phase in the composite was burnt out at 500 ºC and the weight of the sample was recorded before and after the treatment. From the theoretical density of PZT and polymer phases, the volume fraction of the PZT fibers in this composite structure was determined to be about 10 %. Using the rule of mixtures;

$$\varepsilon'_{composite} = \varepsilon'_{polymer} \times V_{polymer} + \varepsilon'_{PZT} \times V_{PZT} \qquad (5.1)$$

and the dielectric constants of the constituent phases, polyvinylester (3.2 @ 1 kHz) and undoped PZT (800 @ 1kHz) [16], the dielectric constant of the composite was calculated as 83.2. This calculated value is higher than the measured value. The difference is attributed to the presence of porosity and its contribution to the dielectric constant of the composite. Similar effect has been reported in the literature on 0–3 composites of PZT particles in a polyvinylidene-trifluoroethylene (PVDF-TrFE) copolymer matrix [17]. The dielectric loss of the composite is below 0.08 at low frequencies and reaches a stable value of 0.04 for the most of the measured frequencies.

**5.5 CONCLUSION**

PZT nanofibers were successfully produced by sequence of electrospinning and sintering processes. Processing conditions, especially the aging of the precursor solution was found to be critical on the morphology of the green fiber mats. Aging was observed to lead to increasing viscosity and a correlated increase in green fiber diameter. Moreover the annealing regime was found to have a significant influence on the morphology of the sintered nanofiber mats with slow heating leading to a more uniform morphology. 3-3 composites were prepared from the PZT fiber mats, at about 10% fiber volume fraction, by infiltrating a polyvinylester polymer into the mat. The dielectric constant of the composite measured at room temperature is more than an order of magnitude higher than the polymer matrix and reasonably agree with the rule of mixture prediction.

## ACKNOWLEDGMENTS

## 5.6 REFERENCES

1.    R. Maeda, J.J. Tsaur, S.H.Lee and M. Ichiki, "Effect of multi-coating process on the orientation and microstructure of lead zirconate titanate (PZT) thin films derived by chemical solution deposition," *J. Electroceram.*, **12**, 89 (2004).

2.    N. Setter and R. Waser, "Electroceramic materials," *Acta Mater.*, **48**, 151 (2000).

3.    J. Ouellette, "How smart are smart materials?," *The Industrial Physicist*, **2**, 4, 10 (1996).

4.    S. Xu, Y. Shi and S. Kim, "Fabrication and mechanical property of nano piezoelectric fibers," *Nanotechnology*, **17**, 4497-4501, (2006).

5.    X.Y. Zhang, X. Zhao, C.W. Lai, X.G. Tang, and J.Y. Dai., "Synthesis and piezoresponse of highly ordered $Pb(Zr_{0.53}Ti_{0.47})O_3$ nanowire arrays," *Appl. Phys. Lett.*, **85**, 4190 (2004).

6.    U.Selvaraj, A.V. Prasadarao, S. Komarneni, K. Brooks  and S. Kurtz, "Sol-gel processing of $PbTiO_3$ and $Pb(Zr_{0.52}Ti_{0.48})O_3$ fibres," *J. Mater. Res.*, **7**, 992–996 (1992).

7.    R.B. Cass, ''Fabrication of Continuous Ceramic Fiber by the Viscous Suspension Spinning Process,'' *Amer. Ceram. Soc. Bull.,* **70 [3]**, 424–429 (1991).

8.    J. Heiber, A. Belloli, P. Ermanni and F. Clemens, "Ferroelectric Characterization of Single PZT Fibers," *J. Intel. Mater. Sys. Struc.*, **20**, 379-385 (2009).

9.    Y.Wang, R. Furlan, I.Ramos, J.J. Santiago-Aviles, "Synthesis and characterization of micro/nanoscopic $Pb(Zr_{0.52}Ti_{0.48})O_3$ fibers by electrospinning," *Appl. Phys. A,* **78**, 1043-1047 (2004).

10.      N.  Dharmaraj,  C.H.  Kim,  H.Y.  Kim,  "Pb($Zr_{0.5}Ti_{0.5}$)$O_3$  nanofibres  by electrospinning," *Mat. Lett*. **59**, 3085-3089 (2005).

11.      W.Sigmund, J.Yuh, H.Park, V.Maneeratana, G. Pyrgiotakis, A. Daga, J. Taylor and J.C. Nino, "Processing and Structure Relationships Electrospinning of Ceramic Fiber Systems," *J. Am. Ceram. Soc*., **89 [2]**, 395-407 (2006).

12.      Z.H. Zhou, X.S. Gao, J. Wang, K.Fujihara, S. Ramakrishna and V. Nagarajan, "Giant strain in Pb($Zr_{0.2}Ti_{0.8}$)$O_3$ nanowires," *Appl. Phys. Lett*., **90**, 052902 (2007).

13.      E. Mensur Alkoy, S. Alkoy, T. Shiosaki, "Microstructure and crystallographic orientation dependence of electrical properties in lead zirconate thin films prepared by sol–gel process," *Jpn. J. Appl. Phys*., **44**, 12, 8606-8612 (2005).

14.      E. Mensur Alkoy, S. Alkoy and T. Shiosaki, "The Effect of Crystallographic Orientation and Solution Aging on the Electrical Properties of Sol–Gel Derived Pb($Zr_{0.45}Ti_{0.55}$)$O_3$ Thin Films," *Ceram. Intern.*, **33**, 1455–1462 (2007).

15.      R.E. Newnham, D.P. Skinner, and L.E. Cross,"Connectivity and piezoelectric-pyroelectric composites", Mat. Res. Bull., 13 [5] 525-536 (1978).

16.      B. Lee and E. Lee, *J.,* "Effects of complex doping on microstructural and electrical properties of PZT ceramics," *Electroceram.*, **17**, 2-4, 597-602 (2006).

17.      M. Dietze and M. Es-Souni, "Structural and functional properties of screen-printed PZT-PVDF-TrFE composites," *Sensors and Actuators A*, **143**, 329–334 (2008).

# CHAPTER 6

## 6 CONCLUDING REMARKS

The functional nanocomposites that have electro-active inorganic fibrous fillers-ZnO and PZT- were extensively investigated within this thesis. The electrospinning method used for producing ceramic and polymer fibers, the crystallinity and process effect upon dielectric behavior, and the characterization of the fibrous-ceramic/polymer nanocomposites were reported. The conclusions for the three papers forming this thesis are given in the associated chapters. Here, a brief summary of the highlights are presented particularly for the functional nanocomposite production and their dielectric characteristics.

Firstly the dielectric characteristics of the polymer PVDF used as a matrix material are elaborated by interpreting the results of the process and crystallinity effect upon the dielectricity as described in the first paper. Then, thanks to the novel method – electrospinning-, non-woven ceramic mats of extremely fragile fibers were obtained. The essential thermal treatment schedule was guided by DTA/TGA simultaneous analysis results. They suggest that the slow removal of the organics from the polymeric precursor fiber mat is imperative as the percentage weight loss was significant after the calcination. Therefore, a stepwise heating schedule was applied with several ramps and dwell steps. From SEM images, a denser and well sintered morphology of the polycrystalline fibers and mats were obtained at the end of the sintering process, confirming the need for sintering process in acquiring the fibrous inorganic formations for the two inorganic materials ZnO and PZT.

Regarding the extensive literature survey within the thesis, the ZnO/PVDF nanocomposite presented here (paper 2) is the first demonstration of the use of electrospinning to secure the dispersion and distribution of a network of inorganic fillers making these fibrous-ceramic/polymer nanocomposites.

Material handling is facilitated and dielectric property measurement is enabled by processing these nanocomposites, in contrast to that on a fibrous mat of pure ceramic. For instance, sandwiching the ZnO mat between solution cast PVDF films and making a polymer matrix-composite via hot-press melt casting provided a practical solution to the mechanical drawback of the fibrous mat. The hot-pressing resulted in the ZnO short fibers with high surface area which, along with polycrystalline morphology allowed the generation of interfacial polarization, due to both the increase in dipoles formed at ZnO/PVDF interface, as well as at internal interfaces in the fibers of the composite film. The enhanced interfacial polarization had significantly increased the dielectric response over the bulk properties of both constituents, as well as over bulk-ZnO/PVDF. Additional nanocomposite demonstration (paper 3) was with electrospun PZT nanofibers. Specifically, 3-3 composites were prepared from the PZT fiber mats, at about 10% fiber volume fraction, by infiltrating a poly(vinylester) into the mat. The dielectric constant of the composite measured at room temperature is more than an order of magnitude higher than the polymer matrix and reasonably agrees with the rule of mixture prediction.

# CHAPTER 7

## 7 SUGGESTIONS AND FUTURE WORK

Several practical problems observed/experienced while making the nanocomposites can also be noted and additional experiments can be proposed to be addressed in the extension of this work. For instance; air bubbles can be formed within the matrix of the resultant PZT based nanocomposite. As a precaution, vacuum can be incorporated into the process flow of the functional nanocomposites to discard the bubbles within the matrix. Furthermore, control of the aspect ratio and the volume fraction of the fillers (~10% in this work) were not in the scope of the thesis, but these factors and their effects in the composite properties are worth investigating in future studies. In this thesis, the characterization of the nanocomposites with single layer filler were carried out. For a future study, the multiple filler layers can be considered and thus, the effect of the filler volume fraction upon the composites can be investigated.

As an environment safe alternative to PZT/PVA precursor solutions, KN, KNN (lead-free) ceramic fibers by electrospinning can similarly be explored. The characterization of such lead-free fibrous- KN or KNN/polymer composites are also worth considering in the future studies.

Additionally, electro-active properties such as ferroelectricity behavior of the composites should be studied and they are underway. For a specific instance, the hysteresis characteristics of a fibrous-PZT/polymer nanocomposite will be measured in order to figure out the ferroelectric behavior of the resultant nanocomposite.

# CHAPTER 8

## 8 APPENDIX

### 8.1 Brief Definition of Dielectric Analysis

A dielectric material is a substance that is a poor conductor of electricity, but an efficient supporter of under the applied electrostatic field. Dielectricity is a physical model that is used to describe how an electric field behaves within a material. Mainly, dielectric behavior is characterized by how an electric field interacts with an atom. A material is formed with atoms in the classical approach of the dielectric model. The atom consists of a positive charge at the centre surrounded by a cloud of negative charge. The atoms separated by enough distance such that they do not interact with one another are represented in Figure 8.1.
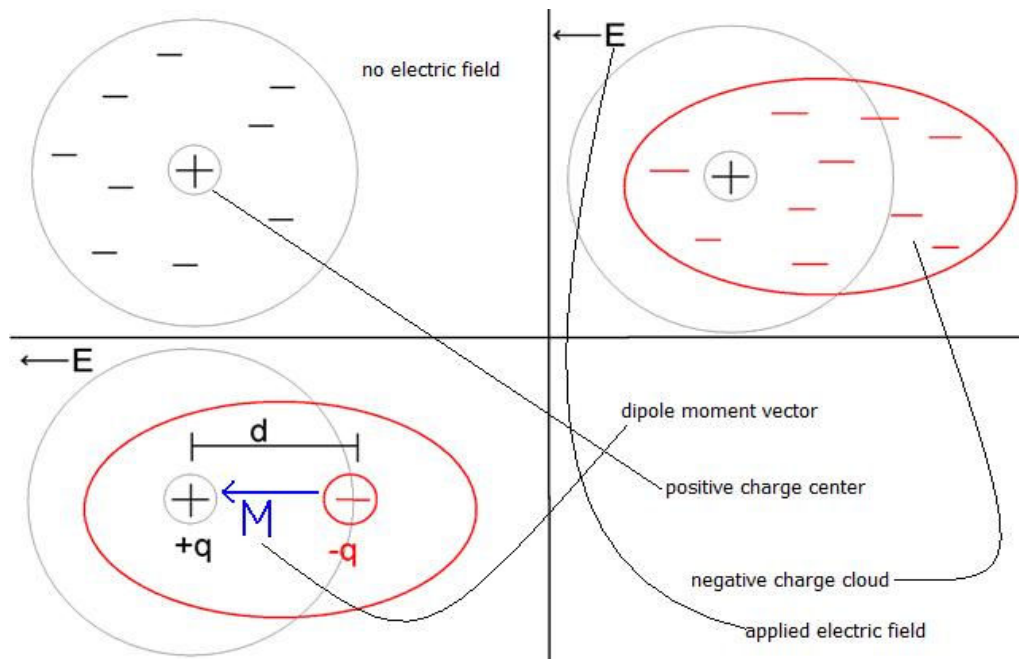
Figure 8.1: Electric field interaction with an atom under the classical dielectric model.

Dipoles within the material can be reduced to a simple dipole using the superposition principle. A dipole is characterized by its dipole moment. This is a vector quantity and is shown as the blue arrow labeled *M* in Figure 8.1. It is the relationship between the electric field and the dipole moment that gives rise to the behavior of the dielectric.

There are three main polarization mechanisms that can occur inside a dielectric material: electronic polarization, ionic polarization (sometimes referred to as atomic polarization), and orientational polarization.

An important property of a dielectric material is its ability to support an electrostatic field while dissipating minimal energy in the form of heat. The lower the dielectric loss (the proportion of energy lost as heat), the more effective a dielectric material. The overall dissipation factor is named dielectric loss in the dielectric material (the ratio of the energy dissipated to the energy stored).

Specifically, a shift in the polarization relaxation frequency associated with the peak of dielectric loss was observed as also stated by Park et *al.* [1]. It is also evident that dielectric loss tends to increase at elevated temperatures [2]. Another consideration is the dielectric response, the extent to which a substance concentrates the electrostatic lines of flux.
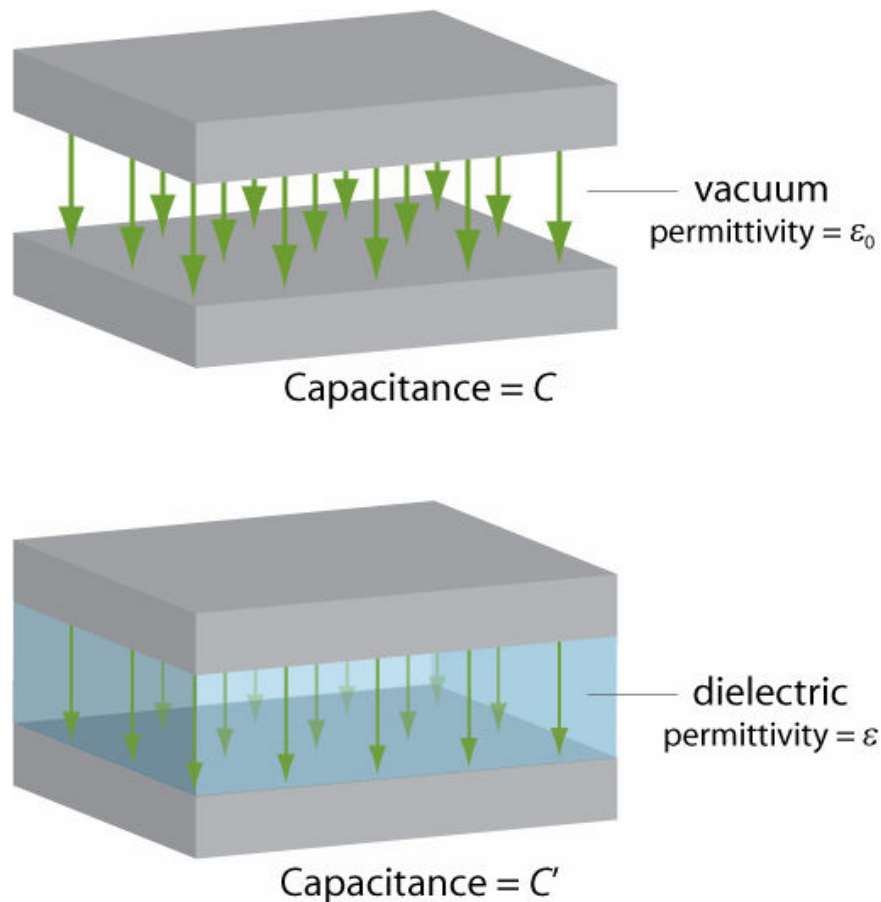


Figure 8.2: The two definitions of the dielectric response. Courtesy of [3].

In fact, there is no standard symbol for the dielectric response – it may be referred to as $\kappa$, $\varepsilon$, $\varepsilon'$ or $\varepsilon_r$. $\kappa$ can be used to avoid confusion with the absolute permittivity, which may also be given the symbol $\varepsilon$. The two definitions of the dielectric response are illustrated by Figure 8.2 (the green arrows represent the electric field).

The complex dielectric expression can be written as $\varepsilon^{*} = \varepsilon^{'} + i\varepsilon^{''}$ in terms of the $\varepsilon'$ is the real dielectric response. $\varepsilon''$ is the imaginary dielectric response (dielectric loss). The real part of dielectric response was calculated from the equation $\varepsilon' = C_{p}d/(\varepsilon_{0}A)$, where $C_{p}$ is the parallel capacitance, $d$ is the inter electrodes distance, $\varepsilon_{0}$ is the permittivity of free space, A is the electroded area. The dielectric loss $\varepsilon''$ was calculated from the equation $\varepsilon'' = \varepsilon'\tan\delta$, where $\delta = 90 - \varphi$ and $\varphi$ is the phase angle. The complex dielectric dispersion curves are described by the Cole–Cole relation that is represented by Eq. (8.1) [4, 5].

$$\varepsilon^{*}(\omega) = \varepsilon_{\infty} + \frac{\varepsilon_{0} - \varepsilon_{\infty}}{1 + (i\omega\tau)^{1-\alpha}} \tag{8.1}$$

where $\varepsilon^{*}(\omega)$ is the complex dielectric response. $\varepsilon_{0}$ is the limiting low-frequency dielectric response and $\varepsilon_{\infty}$ the limiting high-frequency dielectric response $\tau$ is the average relaxation time. $\omega$ is the average angular frequency and $\alpha$ is the distribution parameter. The relaxation curve for $\alpha = 1$ corresponds to the Debye-type relaxation and a smaller $\alpha$ value gives a broader symmetric relaxation curve [6].

The relaxation parameters that are found by the dielectric spectroscopy technique give the information regarding the microstructural characteristics of the materials such as the molecular mobility/ability to move within the material. Moreover, a semi-circular Cole-Cole plot shows that the material has resistance-capacitance (RC) type circuit characteristics. Thus, the Cole-Cole plots are significantly valuable to determine the movement mechanism of molecules under the applied electric field in materials.

## 8.2 Dielectric Response and Loss[1]

The ceramics as insulators have several advantages due to their capability for high-temperature operation without hazardous degradation in chemical, mechanical, or dielectric properties.

Linear dielectrics are described as insulator type materials in which the electric displacement $(D)$ increases in direct proportion to the electric field in the dielectric $(E)$, the constant of proportionality being defined as the relative dielectric response $(k')$. These relationships can be given as [8.2]

$$D = \varepsilon_0 E_a = \varepsilon_0 k' E \tag{8.2}$$

where $E_a$ is the applied field and $\varepsilon_0$ the permittivity (dielectric constant) of vacuum = 8.85*10 -12 F/m. The length to which the electric field has been altered by the presence of the dielectric is described as the electric displacement. Simply, the dielectric response can be defined as it is a characteristic material property and a measure of the ability of the material to store charge relative to vacuum.

In addition to the dielectric response $(k')$, three other material properties are significant in determining the insulating characteristics of the material. These are the electrical (volume) resistivity $(\rho)$, the dissipation factor (DF) $(\tan \delta)$, and the dielectric strength (DS). The measure of the resistance that a unit cube of the material offers to current flow in a given (dc) field is simply the electrical resistivity.

1. "Ceramic Materials for Electronics: Processing, Properties and Applications", Second Edition, Revised and Expanded, Chapter 1: Properties of Ceramic Insulators, p: 31-43, edited by Relva C. Buchanan, 1991 by Mercel Dekker, INC.

The electrical resistivity and the dielectric response are related by the dissipation factor, which measures the energy loss per cycle (usually in the form of heat) from the material in an ac field. This relationship is given by

$$\sigma = \frac{1}{\rho} = \omega \varepsilon_0 k' \tan \delta \qquad (8.3)$$

where $\sigma$ is the conductivity $(\Omega \cdot m)^{-1}$, $\omega = 2\pi f$ ($f = frequency$), and $k' \tan \delta$ is the loss factor $(k'')$. Eq. 8.3 also gives the frequency dependence of the resistivity $(\rho)$ for a loss resistance in parallel with the capacitance.

The maximum voltage gradient is the measure of the dielectric strength. It can be imposed across the dielectric without physical degradation of its insulating properties, leading to breakdown.

From Eq. (8.2) and the capacitive cell illustrated in Figure 8.3, expressions for the relative dielectric response $k'$, total charge $Q$ (coulombs), and capacitance $C$ (farads) for the cell can be developed as follows

$$k' = \frac{D}{\varepsilon_0 E} = \frac{Q/A}{\varepsilon_0 V / d} \qquad (8.4)$$

Therefore,

$$Q = \varepsilon_0 k' \frac{A}{d} V = CV \qquad (8.5)$$
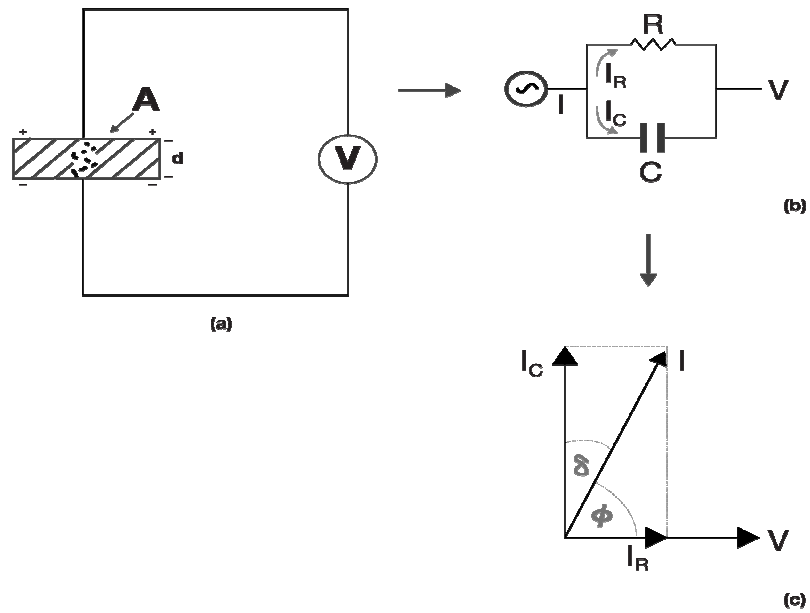
Figure 8.3: Equivalent circuit diagrams: (a) capacitive cell; (b) charging and loss current; (c) loss tangent for a typical dielectric.

where

$$C = \varepsilon_0 k' \frac{A}{d} \tag{8.6}$$

$$C_0 = \varepsilon_0 \frac{A}{d} \tag{8.7}$$

and

$$k' = \frac{C}{C_0} = \frac{\varepsilon}{\varepsilon_0} \tag{8.8}$$

A represents the area of the capacitance cell, d its thickness, C0 and C the respective air and material capacitance, V the voltage imposed across the cell, and the material permittivity (F/m). Thus represents the ratio of the permittivities or the charge stored in the capacitive cell relative to air or vacuum as dielectric. If V is sinusoidal, Eq. (8.5) may be written as

$$Q = CV_0 e^{i\omega t} \tag{8.9}$$

Therefore,

$$I = \frac{dQ}{dt} = i\omega CV = i\omega C_0 \varepsilon_0 k' V \tag{8.10}$$

where I represents the current flow on discharge of the capacitive cell in time t. However, for a real dielectric the current I has vector components IC and IR, as illustrated in Figure 8.3 for the condition of a lossy dielectric, represented by the circuit analog of a parallel resistance-capacitor. The current IC represents a (wattless) capacitive current proportional to the charge stored in the capacitor. It is frequency dependent and leads the voltage by $90^o$. The current IR is an ac conduction current in phase with the voltage V, which represents the energy loss or power dissipated in the dielectric. This situation can be represented by a complex permittivity or dielectric response, in order to deal with the loss current, as follows:

$$I = i\omega C_0 \varepsilon_0 \left(k' - ik''\right)V \tag{8.10a}$$

$$I = i\omega C_0 \varepsilon_0 k' V + \omega C_0 \varepsilon_0 k'' V \tag{8.10b}$$

$$I = I_C + I_R \tag{8.10c}$$

From the magnitude of these currents, therefore, one can define a dissipation factor, $\tan\delta$, as

$$\tan\delta = \left|\frac{I_R}{I_C}\right| = \frac{\omega C_0 \varepsilon_0 k'' V}{\omega C_0 \varepsilon_0 k' V} = \frac{k''}{k'} \tag{8.11}$$

These vector relationship, illustrated in Figure 8.3, show the phase angle $\phi$ as $\left(90 - \delta^o\right)$ and the loss tangent, $\delta$ representing the deviation from ideality or lossiness in the dielectric.

A quality factor Q, defined as:

$$Q = \frac{1}{\tan \delta} = \frac{average\ energy\ stored\ per\ cycle}{energy\ dissipated\ per\ cycle}$$

(8.12)

is frequently used as a key design parameter for dielectric usage. Table 8.1 to 8.2 define the relevant dielectric parameters and summarize the useful relationships between them for dielectric applications.

## 8.3 Polarization in Dielectric Solids[1]

The dielectric response and dissipation factor are significant true material properties so they can be understood in terms of composition and structure, which define material behavior in a dielectric field. Three vector quantities can be used to describe the macroscopic dielectric behavior: the dielectric displacement $D$, the field $E$, and polarization $P$:

$$D = \varepsilon_0 k' E = \varepsilon_0 E + P$$

(8.13)

Therefore,

$$P = \varepsilon_0 (k' - 1) E = \varepsilon_0 x E$$

(8.14)

where $x$ is defined as the electric susceptibility and is the proportionality factor that directly relates the polarizability to field in a linear dielectric. Polarization can be also described in terms of a bound charge (surface) density related to the dielectric response, which opposes the surface charge density $\sigma_s$. This density is created by the applied field, that is,

$$P = \sigma\left(1 - \frac{1}{k'}\right) \tag{8.15}$$

or in terms of a volume charge density related to the concentration of dipoles per unit volume, $N$, and the local field $E'$ in the dielectric:

$$P = \alpha N E' \tag{8.16}$$

and

$$E' = \frac{k' + 2}{3} E \tag{8.17}$$

where $\alpha$ is defined as the polarizability and is a true material parameter with components reflecting polarization mechanism in the solid.

From Eqs. (8.14) and (8.15) expressions can be developed by (Clausius-Mosotti) relating the dielectric response to the various polarizability mechanisms:

$$\frac{k' - 1}{k' + 2} = \frac{N\alpha}{3\varepsilon_0} = \frac{1}{3\varepsilon_0} \cdot \frac{N_0 \rho_d}{M} \alpha = \frac{1}{3\varepsilon_0} \sum N_i \alpha_i \tag{8.18}$$

where $N_0$ is Avogadro's number with $\rho_d$ and $M$ the density and molecular weight of the solid, respectively. The components of the polarizability are

$$\alpha = \alpha_e + \alpha_i + \alpha_o + \alpha_s \tag{8.19}$$

representing susceptibilities associated with electronic, ionic, orientation, and space charge polarization, respectively.

Electronic polarization $(P_e)$ occurs in all solids up to optical frequencies $\sim10^{16}$ Hz and is due to shifts or displacement of electron clouds in the dielectric field away from their equilibrium positions, resulting in a net dipolar response. Apart from electronic polarization, ionic polarization $(P_i)$ results from similar ionic displacement in the field and occurs up to the infrared region of $10^{10}$-$10^{13}$ Hz. The polarization $(P_e + P_i) = P_\infty$ is mostly composition dependent, instantaneous, or nearly frequency independent for most dielectrics and only marginally affected by temperature. Conversely, orientation polarization is both frequency (time) and temperature dependent, since it represents dipole orientation and ion jump polarization. The parameter $P_s = P_o + P_\infty$ thus represents the total polarization from all mechanism, including the static or low-frequency polarization. According to Debye, $P_o$ is time dependent, approaching its final value in an exponential manner described by

$$P_o(t) = P_o \left(1 - e^{-t/\tau}\right)$$

(8.20)

where $\tau$ is the relaxation time [ period needed to diminish the polarization charge to $\sim37\%$ (1/e) of its original value ]. Solution of Eq. (8.20) in terms of complex quantities gives the Debye equations:

$$k' = k'_\infty + \frac{k'_s - k'_\infty}{1 + \omega^2 \tau^2}$$

(8.21a)

$$k'' = \frac{\left(k'_s - k'_\infty\right)\omega t}{1 + \omega^2 \tau^2}$$

(8.21b)

$$\tan\delta = \frac{k''}{k'} = \frac{\left(k'_s - k'_\infty\right)\omega\tau}{k'_s + k'_\infty \omega^2 \tau^2}$$

(8.21c)

where and represent the dielectric response for the equivalent polarizations. The relaxation behavior representing these parameters for the ideal Debye solid (single relaxation mode) are illustrated in Figure 8.4. For $k'$ and $k''$, maximum relaxation and loss occur at $\omega\tau = 1$ and slightly higher for the $\tan\delta$ peak.
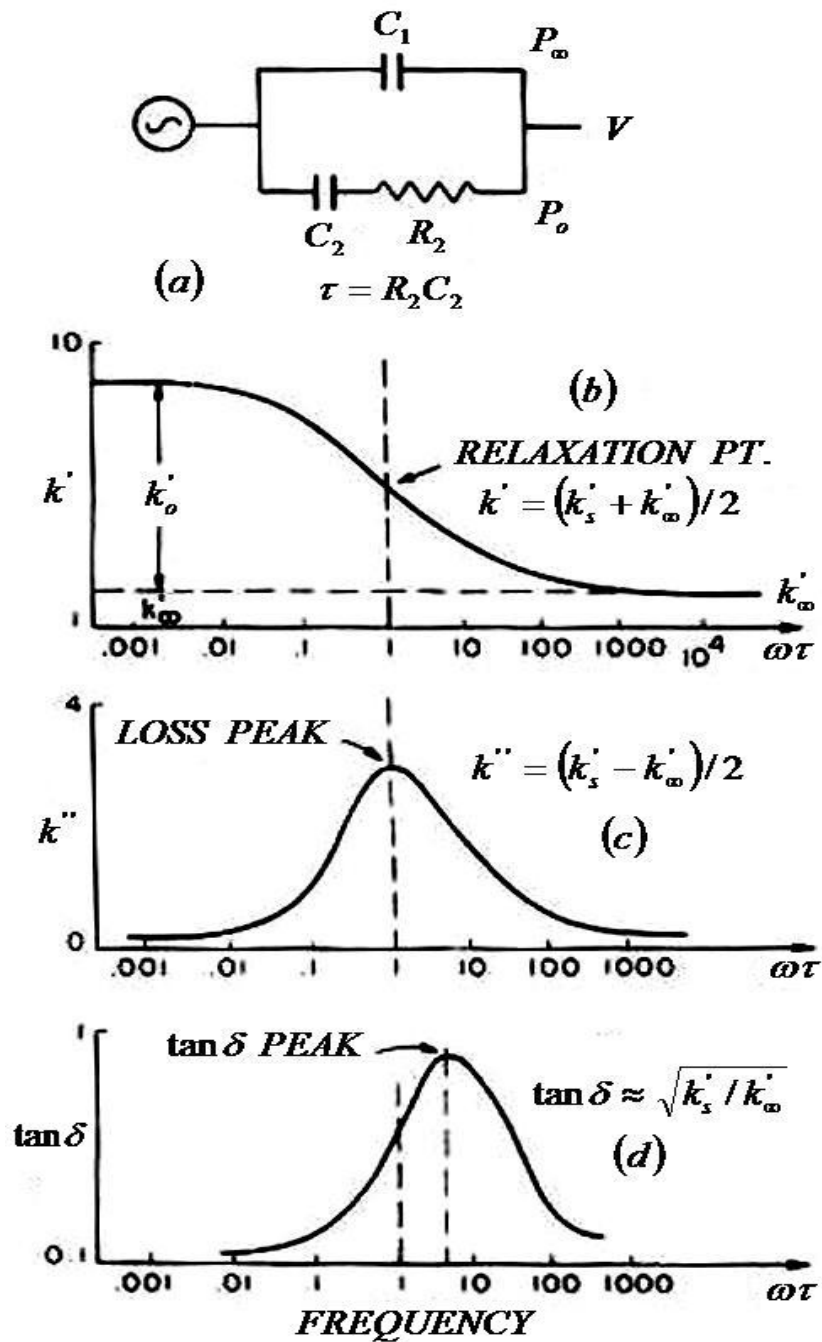
"Figure 8.4: Representations of (a) dielectric circuit for a Debye solid, (b) dielectric response (polarization), (c) dielectric loss factor, and (d) dissipation factor, as a function of frequency for a solid with single relaxation mode." Courtesy of Relva C. Buchanan.[1]
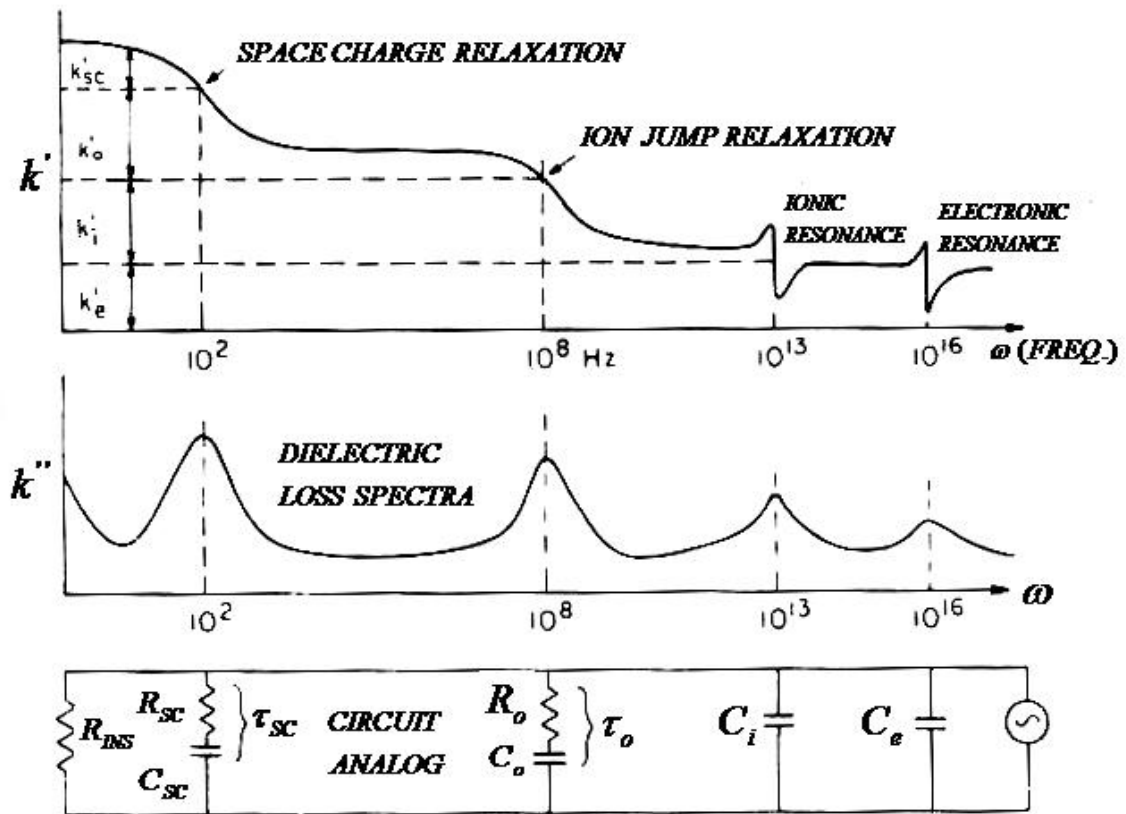
"Figure 8.5: Frequency dispersion behavior for a general solid with multiple relaxation and resonance modes, with analogy of equivalent circuits representing loss mechanism." Courtesy of Relva C. Buchanan.[1]

Figure 8.5 shows the frequency and the corresponding circuit analogs for a general solid with several relaxation modes.

The resonance losses forming for ionic and electronic oscillations at infrared and ultraviolet frequencies are associated with absorption interactions with the incident radiation at or near the natural vibration frequencies of the ions or electrons. In contrast, relaxation losses are associated with dipolar orientation, ion jump, or electron hopping. Space charge polarization are associated with ion migration and electrode contact losses or with the presence of grain boundary inhomogeneous phases in the dielectric material and losses typically occur at low frequency (<1 kHz). Space charge losses in the following case can occur up to much higher (~$10^5$ Hz) frequencies.

106

The composition, frequency, and temperature of the dielectric are significantly important variables for the contributions to the overall dielectric response from different polarization mechanism. For predominantly electronic solids such as diamond and molecular solids such as polyethylene, the dielectric response is closely related to the refractive index (i.e., $k^{'} \approx n^2$). Otherwise, the electronic polarizability is given by

$$\alpha_e = 4\pi\varepsilon_0 r_0^3 = \frac{\varepsilon_0}{N_0}R_\infty \qquad (8.22)$$

where

$$R_\infty = \frac{n^2 - 1}{n^2 + 1}\frac{M}{\rho_d} \qquad (8.23)$$

and $r_0$ represents the radius of the atom or ion, $n$ the reflective index, and $R_\infty$ the molar refractivity, values for which are available for different ions. In general, $\alpha_e$ increases with ion concentration, ion size, and ion polarizability, hence the use of such ions as $Ba^{2+,}$ $Pb^{2+}$, $La^{3+}$ and $K^+$ in optical glasses in order to achieve a higher dielectric response and refractive index. For predominantly ionic solids such as MgO, $Al_2O_3$, and NaCl, the ionic polarizability $\alpha_i$ can be expressed analytically as

$$\alpha_i = \frac{(ez)^2}{2\omega_0^2 a^3}\left(\frac{1}{m_1} - \frac{1}{m_2}\right) \qquad (8.24)$$

where $\omega_0$ is the ionic resonance frequency ($\sim 10^{13}$ Hz), $a$ the interionic separation, $ez$ the charge on the ion, and $m_1$ and $m_2$ the mass of the cation and anion. Ion size and separation are seen to have a significant effect on the polarization, which in these solids generally exceeds the electronic polarization, and thus contribute most to the dielectric response.

For ceramic insulators that have mobile ions, the orientation polarization can be considered equivalent to an ion jump polarization, $\alpha_j$, where

$$\alpha_o = \frac{p^2}{3kT} \quad and \quad \alpha_j = \frac{(ezd)^2}{3kT} \tag{8.25}$$

and $p = ezd$ is dipole moment associated with the jump of an ion of charge $ez$ through a distance $d$. As a function of frequency, the real and imaginary (loss) parts of a complex $\alpha_j$ may be given as

$$\alpha_j' = \frac{(ezd)^2}{3kT} \frac{1}{1+\omega^2\tau^2} \tag{8.26}$$

$$\alpha_j'' = \frac{(ezd)^2}{3kT} \frac{\omega\tau}{1+\omega^2\tau^2} \tag{8.27}$$

$$\tau = \frac{1}{2v} = \tau_0 e^{\mu/kT} \tag{8.28}$$

and

$$n = n_0 v = n_0 e^{-\mu/kT} \tag{8.29}$$

where $\tau$ is the relaxation time, $v$ the jump frequency, $n$ the number of successful ion jumps per second, and $\mu$ the activation energy for ion jump (~ 0.4 - 0.9 eV for ceramics). For ceramics, $\tau$ decreases with elevated temperature, the relaxations move to higher temperature with elevated frequency. However, since $n$ (the number of successful ion jumps per unit time) also increases constantly with temperature. Instead, the dielectric response and loss increase continuously with temperature but decrease with frequency.

Table 8.1: Definitions of Dielectric Parameters[1]

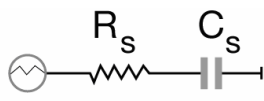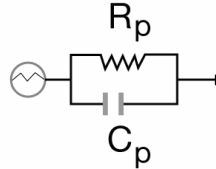| Units | Parameter | Definition |
|---|---|---|
| Farads | $C_0$ | Capacitance of cell with air/vacuum dielectric |
| Farads | $C$ | Capacitance of cell with solid dielectric |
| Coulombs | $Q$ | Total charge on capacitor |
| C/sec (A) | $I$ | $dQ/dt$ =current due to charge flow |
| F/m | $\varepsilon_0$ | Dielectric constant of vacuum (permittivity) |
| F/m | $\varepsilon'$ | Dielectric response of solid |
| | $k'$ | $\varepsilon' / \varepsilon_0$ = relative dielectric response |
| | $\varepsilon''$ | Loss permittivity of solid |
| | $k''$ | $\varepsilon'' / \varepsilon_0$ = relative loss factor |
| $(\Omega \cdot m)^{-1}$ | $\sigma$ | Dielectric conductivity |
| | $\tan \delta$ | $D = dissipation\ factor = \dfrac{energy\ dissipated\ /\ cycle}{energy\ stored\ in\ solid}$ |
| | Q | Quality factor = $1/\tan \delta$ |
| $(\Omega)$ | Z | Circuit impedance $Z^*(\omega) = \dfrac{V^*(\omega t)}{I^*(\omega t)}$ |
| Sec | $\tau$ | time constant |
| | $\varepsilon_0$ | $8.85*10^{-12}$ F/m; $8.85*10^{-12}$ F/cm |
| | $C'$ | Real capacitance |
| | $C''$ | Imaginary part (loss part) of capacitance |

Courtesy of Relva C. Buchanan.[1]

Table 8.2: Relationships Between Dielectric Parameters[1]

**Capacitance**

$$C_0 = \varepsilon_0 \frac{A}{d}$$

*also*

$$C = \varepsilon' \frac{A}{d}$$

$$\frac{C}{C_0} = \frac{\varepsilon'}{\varepsilon_0} = k'$$

$$\varepsilon = \varepsilon_0 k'$$

**Complex quantities**

$$\varepsilon^* = \varepsilon' - i\varepsilon''$$

$$\varepsilon^* = \varepsilon_0 k^*$$

$$k^* = k' - ik''$$

*and*

$$C' = \frac{C_s}{1 + \omega^2 \tau^2} \quad ; C'' = \frac{C_s \omega \tau}{1 + \omega^2 \tau^2}$$

$$\varepsilon'' = \varepsilon_0 k''$$

**Time constant/dissipation factor**

$$\tan \delta = \omega R_s C_s = \frac{1}{\omega R_p C_p}$$

$$\tau = RC \quad (series)$$

$$\tan \delta = \omega \tau$$

$$\tan \delta = \frac{\varepsilon''}{\varepsilon'} = \frac{k''}{k'} = \frac{C''}{C'}$$

$$\tan \delta = \frac{\sigma}{\omega \varepsilon'} = \frac{\sigma}{\omega \varepsilon_0 k'}$$

$$\tan \delta = \frac{1}{Q}$$

**Charge current**

$$Q = CV; V = V_0 e^{i\omega t}$$

$$I = \frac{dQ}{dt} = i\omega CV$$

$$Z = \frac{V}{I} = \frac{V}{i\omega CV} = \frac{1}{i\omega C}$$

**Dielectric power loss**

$$W = \omega \varepsilon_0 k' V^2 \tan \delta \quad (W / cycle)$$

**Dielectric conductivity**

$$\sigma = \omega \varepsilon'' = \varepsilon_0 \omega k'' = \varepsilon_0 \omega k' \tan \delta$$

Courtesy of Relva C. Buchanan.[3]

Table 8.3: Series and Parallel Dielectric Circuit Equations [a1]

| | $Z$ | $\lvert Z \rvert$ | $\tan \delta$ | $\tau$ |
|---|---|---|---|---|
| (a) | $R_s + \dfrac{1}{i\omega C_s}$ | $\dfrac{1}{\omega C_s}\left(1+\omega^2 C_s^2 R_s^2\right)^{1/2}$ $= \dfrac{1}{\omega C_s}\left(1+\tan^2\delta\right)^{1/2}$ $= \dfrac{1}{\omega C_s}\left(1+\omega^2\tau^2\right)^{1/2}$ | $\omega R_s C_s$ | $R_s C_s$ |
| (b) | $\dfrac{R_p}{1+i\omega R_p C_p}$ | $\dfrac{R_p}{\left(1+\omega^2 R_p^2 C_p^2\right)^{1/2}}$ $= \dfrac{R_p}{\left(1+1/\tan^2\delta\right)^{1/2}}$ | $\dfrac{1}{\omega R_p C_p}$ | $\dfrac{1}{\omega^2 R_p C_p}$ |

(a) $R_s$ $C_s$

(b) $R_p$ $C_p$

(c) $R_p = R_s + \dfrac{1}{\tan^2\delta}$

$C_p = \dfrac{C_s}{1+\tan^2\delta}$

$\varepsilon'_p = \dfrac{\varepsilon'_s}{1+\tan^2\delta}$ ; $k'_p = \dfrac{k'_s}{\left(1+\tan^2\delta\right)}$

Courtesy of Relva C. Buchanan.[1]

"[a] Series circuits are used mainly for low-loss materials ( $\tan\delta$ <0.032), which consritute most dielectrics. For ( $\tan\delta$ >0.032), however, the series equivalent circuit goes too high a value for $k'$ and $k''$ and the parallel equivalent circuit should be used [i.e., a correction should be made (using the equations above) if very accurate results are desired]."[3]

## 8.4 References

[1] Park, S.-H.; Lim, E.-C.; Park, K.-S.; Kang, D.-H.; Han, S.-O.; Lee, D.-C. Proceedings of the 5th Internationd Conference on Properties and Applications of Dielectric Materials May 25-30, 1997, Seoul, Korea.

[2] Dagdeviren, C.; Papila, M. Dielectric Behavior Characterization of Fibrous-ZnO/PVDF Nanocomposites, *Journal of Polymer Composites*, accepted April, 2009.

[3] http://www.doitpoms.ac.uk/tlplib/dielectrics/dielectric_constant.php last accessed on February 1, (2008).

[4] Raju, G. G. Dielectrics in Electric Fields -Marcel Dekker- 2003.

[5] Cole, K. S.; Cole, R. H. Dispersion and absorption in dielectrics. I. Alternating current, *J. Chem. Phys.* 9, 1941, 341–51.

[6] Ma, W.; Zhang J., Wang X. Formation of poly(vinylidene fluoride) crystalline phases from tetrahydrofuran/N, N-dimethylformamide mixed solvent, *J. Mater. Sci.*, 43, 2008, 398–401.

**BIOGRAPHICAL SKETCH**

Canan Dağdeviren has been fascinated by science ever since she was a child. At age 3, she began to draw her figment of a spacecraft with her best friend and sweet brother Caner to find their stars in the sky. When she was 6, she tried to find the atom of a stone by cutting it into small pieces in defiance of people's saying that it was impossible to see the atom with the naked eye. Funny girl!

Because of her fluent speech and telling imaginative stories, her teachers always thought that she would be a writer or literature teacher. Actually, she was not good at mathematics and solving problems until 12, because she thought that most mathematics problems were not logical and solving problems wasted time. So, her teacher did not think that she would succeed in science. Apart from this, she graduated from all her schools with the highest honors. She always did what she wanted and thank God reached her goals successfully. As the great leader Mustafa Kemal Atatürk had once requested; she will try to do her best in her limited life time for humanity and peace.

After she completed her high school education from Seyhan ÇEAŞ Anatolian High School and Oruç Reis Anatolian High School, she decided to attend the Department of Physics Engineering in Hacettepe University because of Prof. Erdal İnönü's suggestions. She thinks that Erdal Hoca changed her life with his magic stick and valuable thoughts.

Now, Canan is 24 and has completed her M.S. degree studying in Materials Science and Engineering at the Sabancı University (SU). She has been awarded a full scholarship from SU and a The Scientific and Technological Research Council of Turkey (TÜBİTAK) project research scholarship. Moreover on August, 2009 as a Fulbright Scholar, she will go the University of Illinois at Urbana, Champaign (UIUC) for a Ph.D. degree in Material Science and Engineering.

In addition to science, music and collecting packet salt have been her other major interests. During her life, she sings the songs that evacuate bad ideas and stress from her brain. She believes that collecting salt is an incredible way to show that crystals are salt - the flavor of life. She will exhibit her salt collection in the future for the benefit of orphaned children.

Canan's life philosophy is based on this sentence: "In the world, there are two most important things that increase when they are shared with other people: One of them is love and the other one is knowledge." She likes to share her love and knowledge with anyone who is willing to have them. She also thinks that people have limited time to live; therefore, now is the time to love, learn and teach!

She is extremely fortunate to have had such incredible opportunities presented to her and is incredibly grateful for all those who have helped her become who she is today and will be in the future.

*Note for the readers: This thesis is dedicated to the stars in the sky. Do you know that everybody has a star in the sky? Try to find it!*

*C.D.*